UNIVERSITY OF TRIESTE

Development of quantum well structures for multi band photon detection

Author:

Tamiraa Ganbold

Supervisor:

Giorgio Biasiol

Tutor:

Ralf Hendrik Menk

A thesis submitted in fulfillment of the requirements

for degree of Doctor of Philosophy

February 2015

Abstract

La ricerca qui presentata è incentrata sullo sviluppo di tecnologie innovative per la produzione di rivelatori di posizione di fasci fotonici veloci (pBPM) per applicazioni in luce di sincrotrone (SR) e laser a elettroni liberi (FEL). Nel nostro lavoro abbiamo proposto un rilevatore *in-situ* che ha dimostrato velocità di risposta ed omogeneità sia per scopi di diagnostica che di calibrazione. I dispositivi sono basati su pozzi quantici (QW) dimateriali semiconduttori InGaAs/InAlAs,che offrono diversi vantaggi grazie alla loro gap di banda diretta e a bassa energia, e all'alta mobilità elettronica a temperatura ambiente. I QW metamorfici di $In_{0.75}Ga_{0.25}As/In_{0.75}Al_{0.25}As$ contenenti un gas di elettroni bidimensionali (2DEG) sono staticresciuti tramite epitassia a faci molecolari (MBE). Tali materiali presentano alcune differenze notevoli rispetto al diamante, che è il materiale utilizzato per i rivelatori commerciali allo stato dell'arte. Innanzitutto, i costi di produzione e di fabbricazione sono molto più bassi. Poi, il coefficiente di assorbimento è molto superiore al diamante su una vasta gamma di energie di raggi X, il che li rende ampiamente complementari in possibili applicazioni. Inoltre, utilizzando semiconduttori composti si possono fabbricare dispositivi con diverse combinazioni di materiali per la barriera ed il QW; ciòha permesso di ridurre la gap di energia fino a 0.6 eV. La disponibilità e la ripetibilità di fabbricazione dei dispositivi è migliore rispetto a quelle del diamante. Quattro configurazioni di dispositivi a QW pixelati sono stati testati con diverse fonti di luce, come radiazione di sincrotrone, tubo a raggi X convenzionali e laser ultra veloce nel vicino UV. In questa tesi, dopo aver introdotto i dispositivi a QW per utilizzo comepBPM, saranno riportati e discussii risultati più importanti ottenuti. Tali risultati indicano che questi rivelatori rispondono con tempi di 100-ps a impulsi laser ultraveloci, cioè un fattore 6 più velocirispetto a rivelatori a semiconduttori commerciali allo stato dell'arte. La precisione raggiunta nella stima della posizione del fascio fotonico è di 800 nm, da confrontare con i 150 nm di rivelatori a diamante commerciali. Inoltre, i nostri rivelatori di fotoni a QW lavorano a tensioni molto inferiori rispetto aipBPMs esistenti. Infine, test con raggi X da radiazione di sincrotrone mostrano come questi dispositivi presentano elevate efficienze di raccolta di carica, che possono essere imputabili all'effetto di moltiplicazione di carica del gas di elettroni 2D all'interno del pozzo. Tutti questi vantaggi rispetto ai rivelatori esistenti basati sul diamante, rendono i nostri dispositivi potenzialmente molto attrattivi come alternativa a quelli commerciali.

Acknowledgements

I would like to express my special appreciation and thanks to my advisor Dr. Giorgio Biasiol, you have been a tremendous mentor for me. I would like to thank you for encouraging my research and for allowing me to grow as a research scientist. Your advice on both research as well as on my career have been priceless. I would also like to thank my tutor, Dr. R.H. Menk. I also want to thank you for letting my defence be an enjoyable moment, and for your brilliant comments and suggestions, thanks to you. I would especially like to thank Dr. Matias Antonelli and Dr. Giuseppe Cautero form the Electromagnetism group of Elettra Sincrotrone Trieste. All of you have been there to support me when I recruited patients and collected data for my Ph.D. thesis. I would like to thank to all the people in TASC Laboratory, CNR-IOM.

A special thanks to my family. Words cannot express how grateful I am to my family for all of the sacrifices that you've made on my behalf. I would also like to thank all of my friends who supported me in writing, and incented me to strive towards my goal. At the end I would like express appreciation to my beloved husband Shinekhuu Sukhbaatar who spent sleepless nights with and was always my support in the moments when there was no one to answer my queries. We acknowledges support from the Training and Research in Italian Laboratories (TRIL) Programme of the International Centre for Theoretical Physics, Trieste. The research leading to these results has received funding from the European Community's Seventh Framework Programme (FP7/2007-2013) under grant agreement n^{o} 312284.

Contents

Chapter 1

Introduction

Much of modern physical science is based on the understanding of matter at the atomic or molecular level of detail. Many forms of light have been developed as probes for acquiring the atomic and electronic structural information. Synchrotron radiation (SR) and Free Electron Laser (FEL) are among the most outstanding examples of such structural tools. SR is produced by accelerating charged particles (e.g. electrons or protons) in storage rings; SR facilities are capable of generating radiation from the far infrared, through the visible and into the X-ray portions of the spectrum. Compared to conventional light sources, SR is characterized by extremely high intensity and a high level of collimation at the sample target (i.e. high brilliance) which enable many experimental applications of light-matter interactions that would otherwise not be feasible. Once generated the light is conditioned by a beamline particular optics to the desired characteristics necessary for experiments involving the interaction of radiation with matter. However, prior to any experimental procedure it is imperative to know the features of the incoming beam, among which its position, direction and intensity. Without the accurate knowledge of where the beam is positioned it becomes difficult to provide a consistent set of operating conditions for any experimental endeavour. Therefore facilities throughout the world employ a variety of beam position monitors, for either the electron or synchrotron radiation beams, to dynamically measure the beam position and direction.

The stability of the photon beam position is one of the main issues for SR and FEL. Therefore, monitoring of X–ray beam position downstream from beamline optics is desirable for diagnostic and calibration purposes [1]. Beamlines are rarely is equipped with a system of feedback with fast bandwidth of the order of kilohertz or higher. It should be noted that the gap

between the diagnostic on beamline and the much more systematic measures in the control of the machine is not attributable only to the technologies used in the lines; it is rather the context of extremely heterogeneous and detailed beamline to hinder the systematic use of strategies and technologies standard.

The evolution of instrumentation and detectors have occurred in recent years leads to reconsider the applications mentioned above in the light of the latest technologies available for the production of photon Beam Position Monitors (pBPM). It is possible and desirable to increase the dissemination of such devices on the beamlines, both for diagnostics and stabilization purposes. Several experimental techniques using SR would take advantage of new solutions for the production of fast and efficient photon detectors. In addition, different applications of the FEL require new methods and devices to control the light beams produced from these fourth generation sources, characterized by a high thermal load and the radiation concentrated in extremely short times (in the scale of femtoseconds) [2].

The doctoral activities presented in this thesis are supported by prolific scientific collaboration between the TASC-IOM-CNR [3], Elettra-Sincrotrone Trieste [4] and the University of Trieste [5]. The work has focused mainly on research, development and testing of innovative technologies for novel *in-situ*, on-axis pBPMs based on solid-state QW devices targeted especially for applications in X-ray sources. During this activity, several prototypes of the QW detectors were made and their performances improved, as demonstrated by a wide range of experiments with different light sources, such as conventional X-ray tubes, near UV laser and SR. Metamorphic InGaAs/InAlAs QWs structures renders it possible to reduce the direct semiconductor band gap down to 0.6 eV in the well layer. This property confers to these QW devices the ability to detect photons over a broad energy range, spanning from visible to X-ray regions. Furthermore, the high density and mobility of carriers in the 2D Electron Gas (2DEG) forming inside the QW allow the development of fast and efficient photon detectors with sub-nanosecond response times.

In the remainder of this work the matters set out above will be discussed in greater detail; after a few chapters that introduce the operating environment and the state of the art regarding pBPM, particular attention will be given to the work of development and testing of new detectors, concluding with a discussion of the experimental results.

Chapter 2

Photon Beam Position Detectors: State of the Art

Several solutions have been proposed in recent decades to manufacture Photon Bam Position Detectors (pBPM), different which differ for both the techniques and the materials used. In this chapter, some existing pBPMs Section (2.1) and particularly solid state Section (2.2) beam monitoring detectors will be introduced.

2.1 Photon beam position monitoring detectors

Beam position changes may be caused by many sources, including refilling of the storage ring, thermal cycles of the monochromators, mirrors and other temperature-, pressure- and mechanical-related factors which may lead to loss of focus on the sample or result in the beam missing the sample altogether. Various devices based on different methods have been studied including, but not limited to, photoconductive, photoemissive, fluorescence and elastic scattering-based devices. In what follows, different types of pBPMs such as ionization chambers, blades and screens will be briefly described. In the last section (2.2) solid state pBPM will be treated more in detail.

2.1.1 Ionization chamber

The position monitor described here is basically non-destructive and can be mounted directly upstream of experiments. The principle for this position monitor is that of a split ionization chamber. These detectors are composed of a sealed chamber containing gas at low absorption of radiation (typically nitrogen), and base their operation on the ionization of gas molecules by incident photons. Polarizing two electrodes placed on opposite walls floors, ions and electrons generated by this process are collected and generates a measurable current proportional to the intensity of the radiation that passes through the chamber. This position-sensitive detector may be sectioned by diagonal electrodes for reading (Fig. 2.1a), thereby creating a linear dependence of the current with respect to the centroid of the light beam [6].

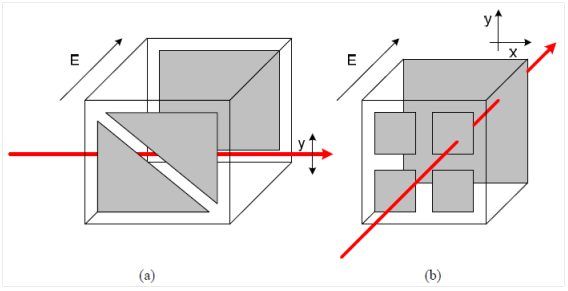

FIGURE 2.1: Representations of ionization chambers: (a) electrode sectioned; (b) a longitudinal field.

In fact, due to the reduction of the longitudinal intensity due to the absorption of the gas, this method does not have a symmetrical response in the two directions; a partial improvement can be obtained with the so-called configuration of backgammon electrodes [7]. With these techniques, position was estimated with accuracies of about 5 to 10 μm. The benefits are limited primarily by the slow speed of the positive ions of the gas, forming ion clouds and creating a counter-internal field, thus reducing the sensitivity and slowing the charge collection. This problem can be significantly reduced by using a longitudinal field configuration, at the price of intercepting the beam with the transverse electrodes (Fig. 2.1b) [8] and can achieve sub-micrometric precision for the position, and 0.3% for the intensity with an adequate flow ($\sim 10^8$ ph/s) .

2.1.2 Blades

The operation of these pBPM is based on the photoemission of electrons by special metal plates as a result of the absorption of photons. These plates are mounted with electrically insulating media within a vacuum chamber, typically according to a cross geometry (Fig. 2.2a); the walls around the supports are polarized positively (with voltages of hundreds of volts) with respect to the edges that are grounded, in order to collect the photo-emitted electrons. The current that is generated on each sheet can be measured and thus provide information about the intensity and position of the incident beam [9].

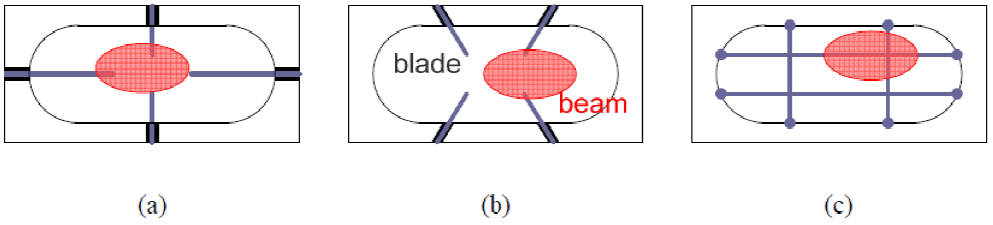

FIGURE 2.2: Schematic representations of pBPM photoelectric effect:a) cross laminae; b) in inclined laminae; c) flush.

One major disadvantage of this technique is the interaction with the destructive and non-uniform beam of photons; in fact, in the case the distance between the plates is too wide, it is possible to intercept only the most marginal parts of the light spot, while if it is too low can produce unwanted shadowing within the beam. In case of intense irradiation, due to the strong absorption of the laminate, these detectors tend to overheat and require cooling systems, with consequent increase in size and noise. Among the most important solutions for the improvement of these pBPM one can quote the inclined electrode configuration (Fig. 2.2b) [10], the use of foils with metallic deposit diamond [11], the introduction of an energy analyser to discriminate the contribution of the insertion devices from that of the radiation from bending [1].

The monitor wires (Fig. 2.2c) operate substantially according to the same principle as those of laminae, with the difference that in such devices the detectors consist of pairs of photo-emitting wires. A peculiarity of these pBPM is the possibility to move them deliberately to scan the beam, and then using them as a beam profiler [12].

2.1.3 Screens

Inserting in the radiation path of the thin layers of appropriate materials, it is possible to estimate the intensity and position of the beam using the indirect emission from such screens. Several phenomena can be at the basis of these emissions; for example it is possible to use the fluorescence of metal screens of thickness of the order of one micron [13], although they are suitable only in certain ranges of energy for the presence of the edges of absorption. To measure the emission of the screen one can use different systems for geometry and detectors. The most common solution consists in using screens orthogonal to the beam surrounded by PIN diodes (Fig. 2.3a) or oblique patterns that emit toward a photo-diode array or CCD sensors placed on a transverse axis (Fig. 2.3b).

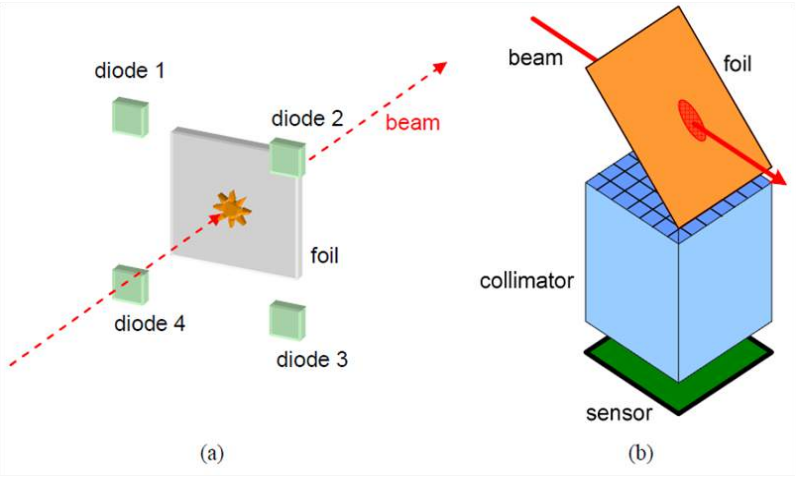

FIGURE 2.3: Representations of pBPM screens: a) orthogonal with PIN diodes; b) with oblique collimator and matrix sensor.

The latter configuration, although much more complex and cumbersome, has some advantages compared to the axial; it is more immune to spurious contributions of any windows in the line and, given the presence of a matrix sensor, can be used as a beam profiler [14]. With these technologies, one can estimate the position of the beam with accuracies between 1 and 10 μm; the absolute intensity measurement requires delicate calibrations due to the indirect method of reading.

2.2 Solid State Detectors

The pBPMs of this type are constituted of a thin layer of active material inserted transversely in the beamline and crossed by the entire light beam, as shown in Fig. 2.4. The absorption of photons of energy above a certain threshold produces free charge in the irradiated volume; therefore, if the device is suitably biased, a current is generated proportional to the incident flow.

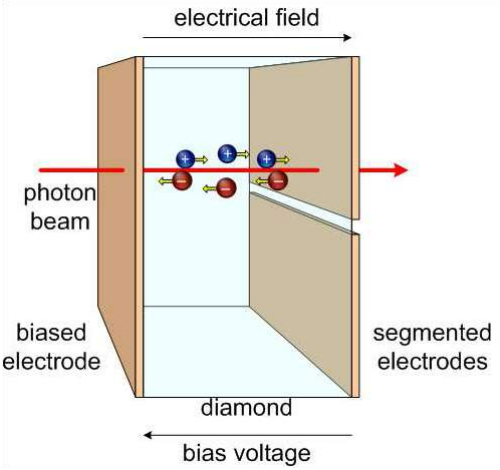

FIGURE 2.4: Block diagram of the operation of a pBPM window with segmented electrodes

The electrical contacts with the material are generally made by metallizations of their surface; on one or both sides, such electrodes can be segmented to render the device sensitive to the position of the light beam. Normally a voltage is applied between the two faces and the resulting electric field has a longitudinal direction, ie parallel to the optical axis. This mechanism is very similar to that used in the above-mentioned ionization chamber [8], which, in fact, mutates its geometry from this type of detectors. However, these solid state devices several advantages compared to ionization chambers. First, the far higher density of the solid phase is reflected in a large number of interactions between photons and atoms in very limited volumes, thus allowing to drastically reduce the thickness of the monitor ($\sim 100\ \mu$m). Thanks to this, and the mobility of free charges, much higher than that of the gas ions, speed limits and sensitivity due to the space charge phenomena occur at frequencies much higher than those reached by the ionization chambers [15]. There are other advantages linked to the small dimensions, such as the possibility of using smaller bias voltages($\sim 10 \div 100$ V, to be compared with $\sim 100 \div 1000$ V of the chambers), and the compatibility with narrow spaces, that allows to insert these devices without changing the structure of the experimental line [16].

In general, the pBPM based on solid state technology are in many respects superior to the other blades and screens as well. A difference of solid-state monitors to foil curtains is that they normally do not require high bias voltages. Furthermore, since they intercept the entire beam, they are little sensitive to variations of the shape of the spot and produce an attenuation uniform over the entire section. Compared to a screen, provide a more direct measurement process,a much smaller footprint, comparable complexity and invasiveness. The two most widely used materials in the manufacture of these detectors are silicon and synthetic diamond obtained by chemical vapor deposition (CVD). The first has technologies nowadays extremely widespread and entrenched, making silicon photo-diodes advantageous in terms of availability, flexibility and reliability of manufacturing processes [17]. For pBPM based on lateral effect diodes precisions are reported down to about 30 nm in the estimation of the position with moderate flow ($\sim 10^8$ ph/s) and 10 Hz bandwidth [16]. The main limitation of the silicon detectors is the limited resistance to ionizing radiation; the latter, in particular interacting with oxide layers, generates charges that are trapped on the surface and interfaces, causing a rapid degradation of the operation of the device [18].

Although the availability of synthetic diamond is much lower than that of silicon, currently it is possible to buy thin sheets of this material at relatively sustainable costs. Diamond, in particular in the monocrystalline form presents unsurpassed physical properties that make it particularly attractive for the production of radiation detectors. It is in fact superior than most other materials in terms of resistance to radiation, thermal conductivity, mobility of sedge, immunity to thermal noise, etc. This material, therefore, can be used in rather hostile conditions characterized by high thermal loads. Due to the low atomic number of the component (Z_C = 6), the diamond has a low absorption for high-energy photons. A layer of 500 μm diamond is semi-transparent for the radiation in excess of 8 keV, while 50 μm diamond can have same transparency at 4 keV [19]. The energy large gap (5.47 eV at 300 K) makes pure diamond an excellent insulator. This gap value makes this material very immune to thermal noise; at RT the resistivity is typically between 10^{13} and 10^{16} Ω cm [8]. The performance that can be achieved with pBPM based on diamond exceeds those achievable by most other technologies. It can detect the passage of individual packets with a photonic band of the order of gigahertz [15], while in a band of 10 Hz you get to estimate the position of the beam with accuracies of 50 nm [20]. Time response of the single crystal diamond detector was reported as 600 ps with ultra fast UV laser source [21].

Chapter 3

Design of photon detectors based on InGaAs/InAlAs quantum wells

This chapter describes the realization of a high mobility two-dimensional electron gas (2DEG) forming inside an InGaAs/InAlAs QW (3.1). In the literature, low temperature electron mobilities (μ) higher than $2.15\times10^5 cm^2V^{-1}s^{-1}$ for 2DEGs confined in an InGaAs channel with an In concentration x = 0.75, are reported for structures grown with molecular beam epitaxy (MBE) on GaAs substrates [22] while typical room temperature electron mobilities are the order of $10^4 cm^2V^{-1}s^{-1}$. The high density and mobility of carriers in the 2DEG forming inside such QW make them promising structures to develop fast and efficient photon detectors. To get a better insight into the potential features of there materials, we have simulated the band structure, the charge distribution and the quantum states of the 2DEG inside the QW. Moreover, electrical properties of the proposed detector were simulated under a bias voltage. In order to describe the working principles of a QW photon detector, the interaction of semiconductor with photons (3.2) will shortly be analyzed end of the the chapter.

3.1 InGaAs/InAlAs quantum wells and 2D Electron Gas

In bulk semiconductors, the electrons have three degrees of freedom. Therefore, there is no quantum confinement (Fig.3.1a). Quantum wells are thin layered semiconductor structures in which we can observe and control many quantum mechanical effects (Fig.3.1b). They derive

most of their special properties from the quantum confinement of charge carriers (electrons and holes) in thin layers of one semiconductor "well" material sandwiched between other semiconductor "barrier" layer, which possesses a higher energy gap. Such quantum confined structures can be realized to a high degree of precision in terms of thickness and composition by modern epitaxial crystal growth techniques. Many of the physical effects in quantum well structures can be seen at room temperature and can be exploited in real devices.

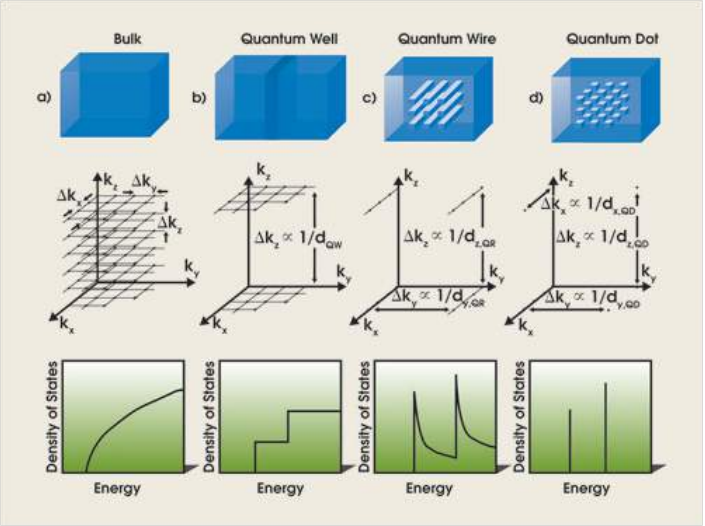

FIGURE 3.1: Electronic states in bulk, quantum well, quantum wire, and quantum dot.

One of the most important features of semiconductors is the possibility to control the concentration of carriers in the conduction or valence band by adding dopants in the crystal matrix. However in bulk materials the incorporation of doping impurities is the limiting factor for obtaining high mobilities at low temperature. In fact they act as charge scattering centers causing a deterioration of the transport properties. In bulk semiconductors, the scattering mechanisms are quite well understood and measured [23]. Five main mechanisms have been identified as limiting factors for the electron mobility:

- Optical-phonon scattering;
- Acoustic-phonon scattering due to deformation potential;
- Acoustic-phonon scattering due to piezoelectric field;
- Scattering by ionized impurities;
- Scattering by neutral impurities.

The various mechanisms is shown in Fig. 3.2 where the experimental temperature dependence of the Hall mobility in n-type bulk GaAs [24] is compared with theory [25]. It is shown that at high temperatures the mobility is limited by phonon scattering whereas ionized impurity scattering dominates at lower temperatures.

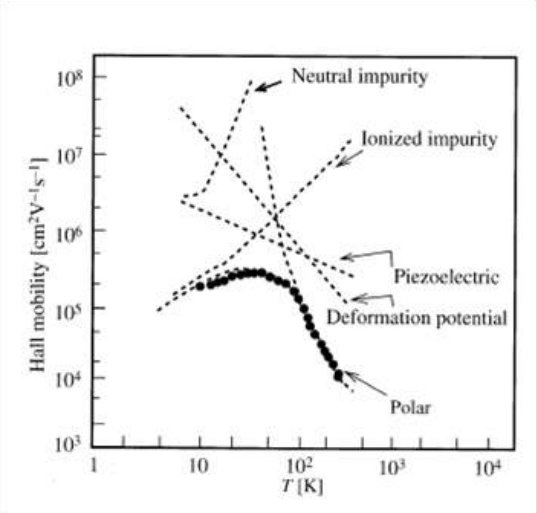

FIGURE 3.2: Temperature dependence of the Hall mobility in n-type GaAs [24]. The dashed curves are the corresponding calculated contributions from various mechanisms [25]

However, at low temperatures the limitation in the mobility can be circumvented by using the so called method of modulation doping proposed by [26]. The idea of this method is to spatially separate the ionized impurities from the conductive layer. In order to realize these structures two materials with different band-gaps are grown one on top of the other. When two semiconductors with different band-gaps are joined together, the discontinuities in the conduction and valence bands create an electrostatic potential, that can attract free charges from the wide to the narrow gap material. If the material with larger band-gap is n-doped (usually by Si atoms in III-V semiconductors), in order to maintain a constant chemical potential throughout the two materials, electrons will flow from the wide gap to the narrow gap one. Single n-type heterojunctions confine electrons in the triangular potential well formed between the conduction band discontinuity on one side and the potential due to the Coulomb attraction of ionized donors on the other side (see Fig. 3.3a). Due to the confining potential, the motion of conductive electrons is restricted in a plane on the narrow band-gap side of the interface, where a 2DEG is formed.

In order to further separate the ionized dopants from the conductive electrons in such systems, an undoped “spacer” region can be inserted between the doping layer and the 2DEG

(see Fig. 3.3a)). Alternatively, a 2DEG can be confined in a potential well, by growing a thin layer, of the order of 10 – 30 nm, of narrow band-gap material in a wide band gap host (see Fig. 3.3b), that can be doped either on one or on both sides of the well.

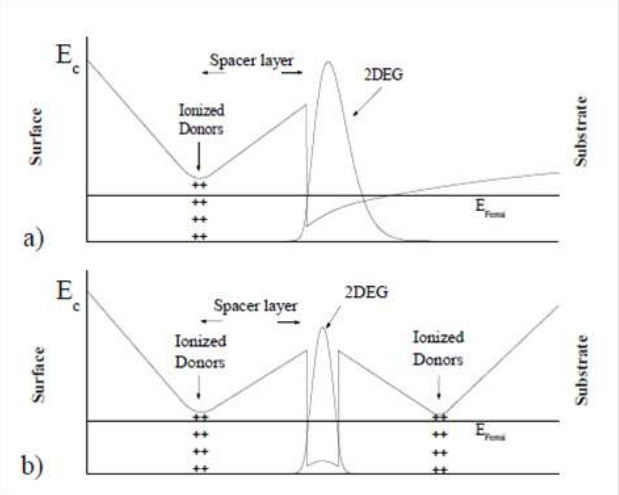

FIGURE 3.3: Conduction band profile for a) a single side doped and b)a symmetrically doped quantum well

Therefore the possibility to control, through the technique of modulation-doping, the effects of ionized dopant impurities on transport properties, makes tit possible to tune in a relatively easy way the carrier concentration in the instrinsically 2D conducting channel, and to obtain high-mobility (and therefore high speed) devices even at room temperature, such as the high electron mobility transistor (HEMT) [27]. In our work, modulation-doped $In_{0.75}Ga_{0.25}As/In_{0.75}Al_{0.25}As$ QW samples were grown by MBE on commercially available 500 μm GaAs semi-insulating wafers. An $Al_{0.33}Ga_{0.67}As/GaAs$ superlattice (SL) was grown to block impurities from the substrate while an $In_xAl_{1-x}As$ buffer layer (BL) with composition x ranging stepwise from 0.15 to 0.75 was introduced to accommodate the $In_{0.75}Ga_{0.25}As$ lattice parameter to that of the substrate. The growth details will be given in Section 5.1. Properties of the 2DEG forming inside the QW were simulated with different Si doping concentrations. In order to provide such simulator with the requested parameters for the different materials, a number of literature models have been taken into account [28–30]. The basic material parameters used in our calculations parameters are shown in Table 3.1:

As the chemical composition of the grown semiconductors develops into a rather complex layered structure, the energy band gap presents many variations, bends and discontinuities along the growth direction. Therefore, the properties of the energy bands at 300K has

TABLE 3.1: Basic parameters for utilized materials

	Lattice constant [A]	Band gap [eV]	Electron effective mass
GaAs	5.6533	1.424	0.063 m_0
$Al_xGa_{1-x}As$	5.6533+0.0078x	1.424+1.247x (x<0.45) 1.09+0.125x (x≥0.45)	(0.063+0.083x)m_0 (x<0.45) (0.85-0.07x)m_0 (x≥0.45)
$In_xAl_{1-x}As$	5.6611+0.3972x	2.163-0.63x	(0.637+0.261x)m_0 x<0.38 (0.146-0.125x)m_0 x≥0.38
$In_xGa_{1-x}As$	6.0583-0.405x	1.424-1.539x	(0.063-0.054x)m_0

been estimated through a software [31] which allows to calculate the profiles of conduction and valence bands, as well as Fermi level, carrier concentrations, electric field etc., by solving self-consistent Poisson-Schrodinger equations. Although the semiconductors constituting these QW should be intrinsic, they actually tend to be n-type due to residual impurities and defects due to the epitaxial growth process [32]. Due to these lattice imperfections, actual donor concentrations are not easy to estimate in real devices. To use reliable values for the presented QWs, impurity concentrations and energies reported in [33] have been considered, since they had previously been measured on epitaxial layers grown with the same process. The energy band diagram calculated through the described procedure is reported in Figure 3.4a.

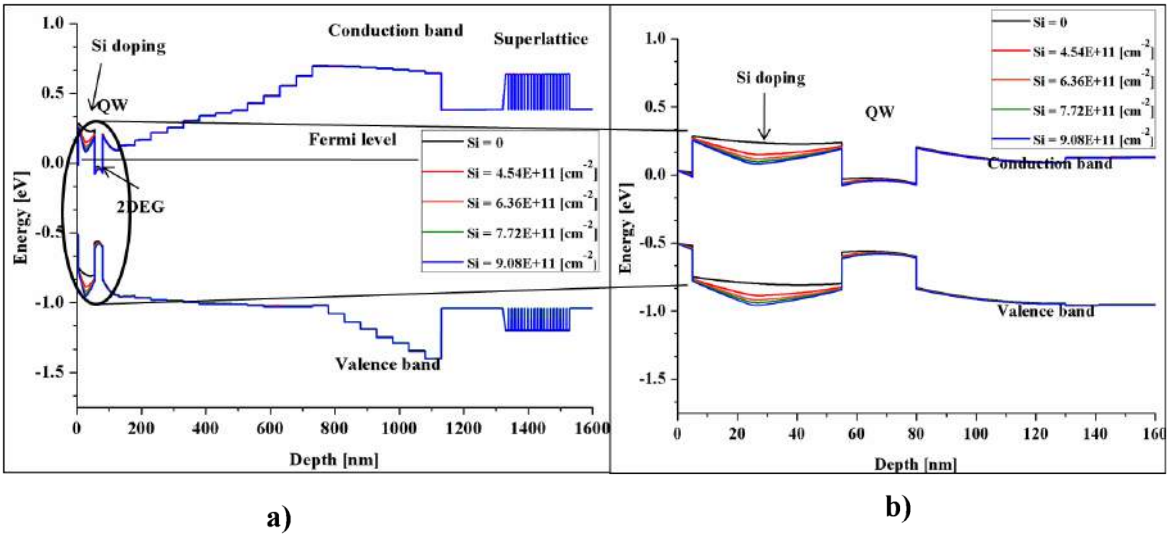

FIGURE 3.4: Simulated band structure of the QW with different Si doping concentration: a) the bands of epitaxial layers; b) zoom of the QW region

As the chemical composition of the BLs changes, a "staircase" band structure is

shown by the simulation, followed by the QW region. A zoomed band profile with different Si doping concentration shows a bending of the band due to the positive ions (Fig. 3.4b). A dependence of the electron concentration inside of the 2DEG on the Si doping concentration is shown in Figure 3.5a. The change of the charge profile inside the QW depending on the Si concentrations is shown in Figure 3.5b. Note that the QW is populated even in the absence of Si donors, due to the intrinsic n-type nature of the materials [33]. It can be seen that, as our samples were doped in the upper barrier only, the charge profile on the doping side becomes higher as the Si amount increases.

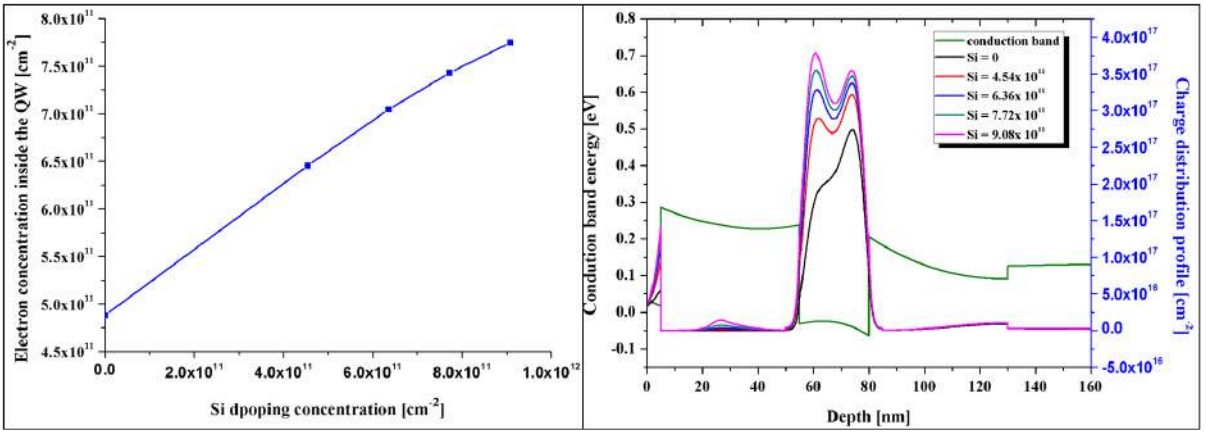

FIGURE 3.5: Charge distribution function of the 2DEG in different Si doping concentrations: a) the charge concentrations; b) the charge distribution profile inside the QW depending on the dopant concentration

3.2 Quantum-well photon detector

In order to motivate the use of the QW heterostructures as a photon detectors, this section will give a short description about the interaction between photons and a semiconductor material. Furthermore, electronic properties of the QW devices are calculated under bias condition.

The InGaAs/InAlAs QW devices are grown on 500 μm GaAs substrate. GaAs is a compound semiconductor with favorable physical characteristics for fabricating photon detectors: the high-atomic number of its constituents (Ga = 31, As = 33) and its wide band gap (1.42 eV) permit to have a high photon absorption (similar to germanium [34] and ten times higher with respect to silicon [35]) and the potentiality to operate at room temperature, not possible

for germanium detectors. Moreover, the well-established microelectronic technology is another advantage of GaAs with respect to other high-Z, wide band gap semiconductors. Two processes are fundamental to the operation of almost all semiconductor optoelectronic devices [36]:

- The absorption of a photon can create an electron-hole pair. The mobile charge carriers resulting from absorption can alter the electrical properties of the material. One such effect, photo-conductivity, is responsible for example for the operation of semiconductor photo-detectors.
- The recombination of an electron and a hole can result in the emission of a photon. This process is responsible for the operation of semiconductor light sources. Spontaneous radiative electron-hole recombination is the underlying process of light generation in the light-emitting diode. Stimulated electron-hole recombination is the source of photons in the semiconductor laser.

The photo-generated charge can be collected at readout electrodes by applying a bias voltage to the device, resulting in measurable currents, which are proportional to a photon flux. The generated charge by the full absorption of the energy of a single detected photon is given by [37]:

$$Q_{gen} = q\frac{E}{\epsilon} \tag{3.1}$$

where q is the elementary charge, E the energy of the photon, and ϵ the mean energy necessary to generate an electron-hole pair in the semiconductor. Moreover, a charge collection efficiency ($CCE = Q_{ind}/Q_{gen}$), can be defined as the ratio between the electric charge induced (Q_{ind}) at the detector output electrode and the charge generated (Q_{gen}) by the full absorption of the energy of a single detected photon. CCE is an important parameter to study and develop radiation detectors. CCE of our devices will be considered in Section 6.3. Photons are absorbed in the device and generate an electron-hole pair; either electrons or holes will be collected as photo-current depending on the bias voltage applied. The electrons will contribute to the current when the device is biased negatively whereas the holes will be collected under positive bias. In an ideal device, all of the charge can be collected as the current, resulting in CCE = 100%. In reality, photo-generated carriers are trapped by deep levels due to material defects

and dislocations, etc. The high density and mobility of carriers in the 2DEG forming inside the QW should allow the development of efficient photon detectors.

Figure 3.6 shows absorption spectra of the active layers as a function of the photon energy in the range from 30 eV to 30 keV. The absorption spectrum is calculated for each material and combined by the corresponding epitaxial growth. The number of photo-generated carriers depends on the photon flux and energy. As shown in the absorption spectrum all of the incident photon are absorbed in the device even at high energy (30 keV), which means 500 μm the QW detector is not transparent, differing to crystal diamond photon detectors. If a back tinning for the QW device is introduced, then the device can be transparent at high energies (from 20 keV to 30 keV) when the total thickness is less than 20 μm.

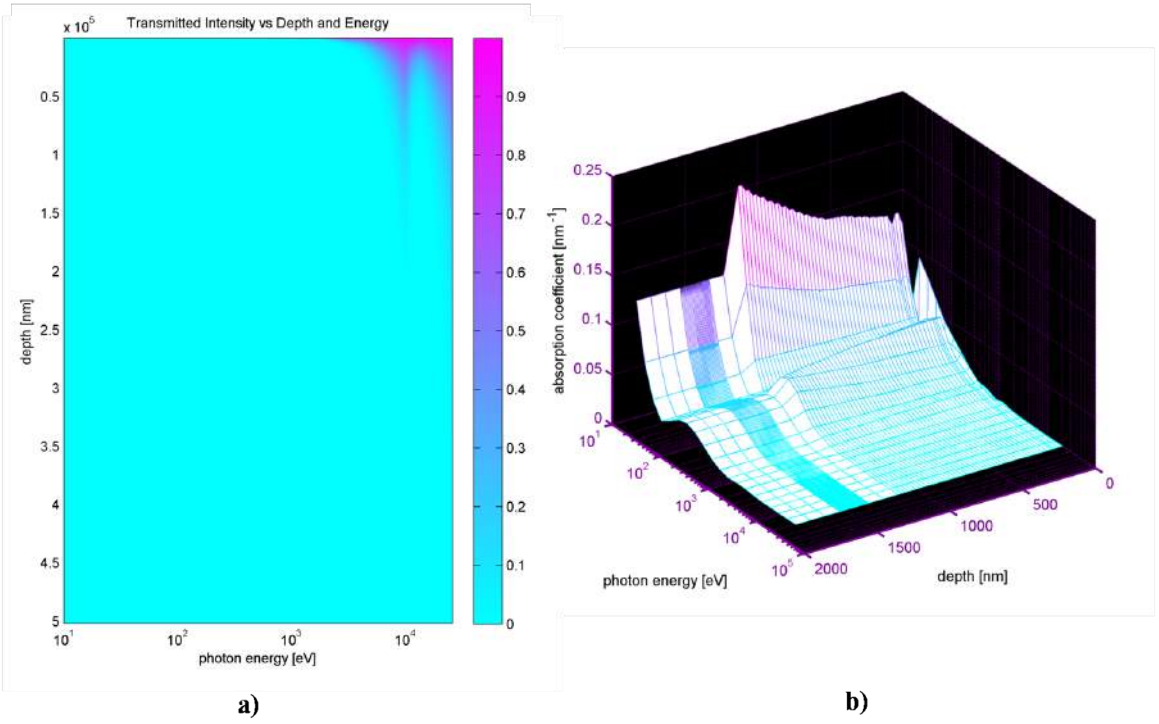

FIGURE 3.6: Photon absorption spectrum of the QW device a) 2D transmission spectra in a photon range from 30 eV to 30 keV b) 3D presentation of the absorption spectrum zoomed in epitaxial grown layers (2 μm from the top surface).

The possibility to use QW photon detectors was reported in the literature in the infrared region [38]. Thanks to their direct, low-energy band gap and high electron mobility, the QW devices based on InGaAs/InAlAs semiconductors have been proposed as multi-wavelength sensors from visible light to hard X-rays in this thesis. These QW devices can generate free charges as a consequence of photon absorption; since the energy gap falls down to about 0.6 eV

in the well layer (Fig. 3.4), a wide band of incident radiation ranging from visible light up to X-rays can be converted. Furthermore, the photons absorbed inside the QW create more than twice as many carriers as those they produce outside the well thanks to the small band gap in such region.

The band structure was simulated under negative bias voltages and a typical Si doping concentration of 9.08×10^{11} (Fig. 3.7).

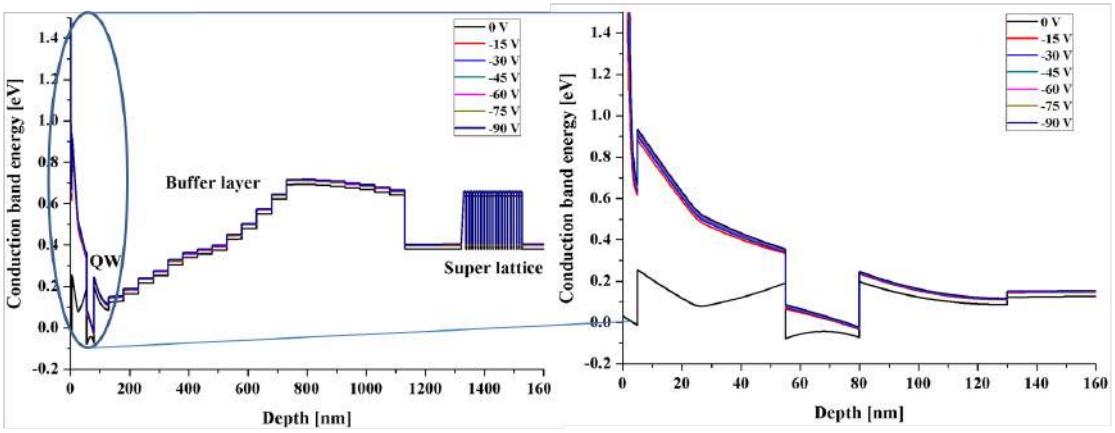

FIGURE 3.7: Conduction band is simulated by the package [31] with different bias voltages; a) the epitaxial layers band profile and b) active region of QW change under negative bias voltage

As a negative voltage is applied to the top surface, the potential across the active layer increases. Therefore , the charge concentration decreases when higher bias voltages are applied (Fig. 3.8).

Furthermore, we have calculated the kinetic energy of an electron in the upper barrier (50 nm InAlAs) + the cap (5nm InGaAs) (Fig. 3.9), which is accelerated by the electric field E under the bias voltages applied to the top surface:

$$E_{kinetic} = \frac{m_e \cdot (v_d)^2}{2 \cdot q} \qquad [eV] \tag{3.2}$$

where $v_d = \mu \cdot E$ is the drift velocity, μ is the electron mobility, q is the electron charge and m_e is the electron effective mass (see Table 3.1).

We take the simulated values of E at the upper interface of the QW with corresponding bias voltages. We do not have any direct measurement of the mobility in the InAlAs layers,

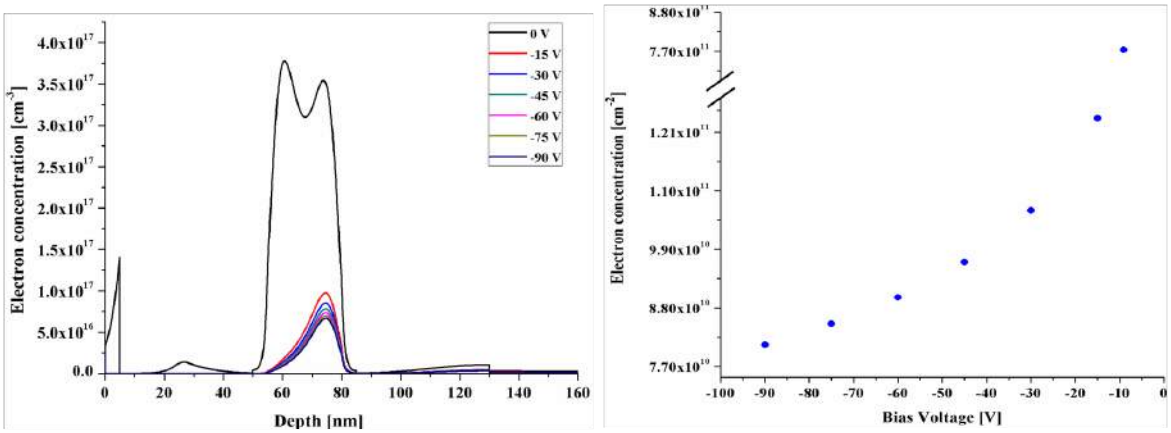

FIGURE 3.8: Simulated carrier density values inside the QW under negative bias voltage; a) charge distribution profile of the 2DEG b) a dependence of the charge concentration on the bias voltage

however we can estimate an upper value for it. The background impurities of our materials have been evaluated of the order of 10^{17}cm^{-3} [33]. Room temperature mobilities for $In_{0.75}Ga_{0.25}As$ with a similar background impurity level have been measured to be 4.5103 cm^{2}V^{-1}s^{-1} [39]. As the InAlAS electron mass is higher than InGaAs (see Table 3.1) and our mobilities are probably limited by epitaxial defects (layer roughness, composition fluctuations, possible residual dislocations [40]), we consider the value of 4.0 as the maximum mobility in our materials. If the kinetic energy of the electron drifting through the layer is higher that the potential barrier of the QW (i.e., the conduction band discontinuity of 0.4 eV), the electron could give the energy to the carriers inside 2DEG by finding lower energy states in the QW and allow them to escape from the well. Figure 3.9 shows schematically this mechanism.

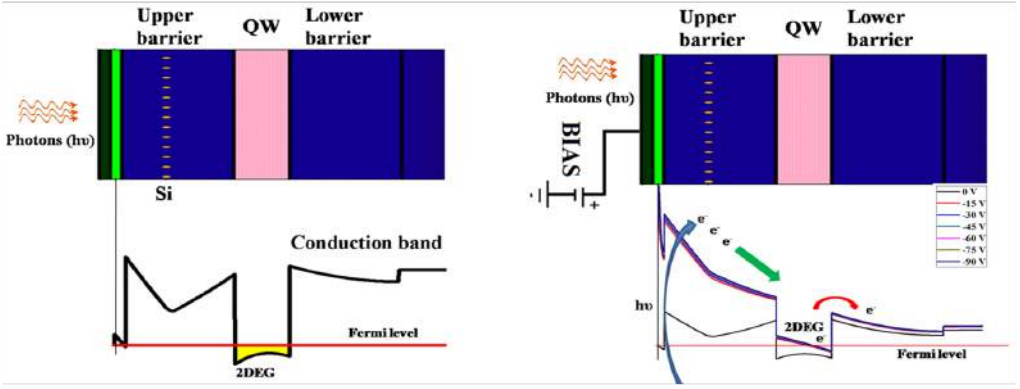

FIGURE 3.9: Charge multiplication mechanism

This contribution to the current could be addressed as *internal charge multiplication*, which will be one of the advantages of the QW detector in terms of efficiency, as it will be shown in Section 6.3. The kinetic energy depends dramatically on the electron mobility μ.

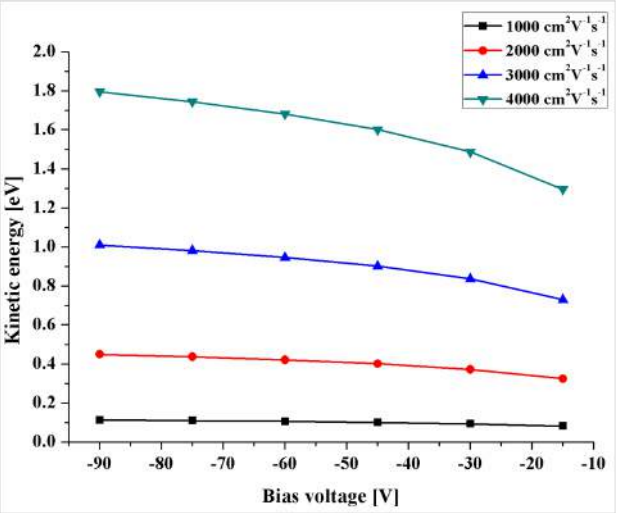

FIGURE 3.10: Calculated kinetic energy of an electron accelerated by the simulated kinetic energy under different bias voltages and the electron mobilities were considered as 1-4$\times 10^3$ $cm^2V^{-1}s^{-1}$ in the InAlAs layer.

Figure 3.10 shows the calculated kinetic energies of the drifting electrons under different bias voltages and mobilities down to 1×10^3 $cm^2V^{-1}s^{-1}$. Such energy is higher than the QW energy barier with all the bias voltages even with the mobility underestimated to the lowest value, which is more than a factor of 4 lower than the maxiumum estimated value. Therefore, we expect that internal charge multiplication is effective in our heterostructure under all the applied voltages in the range considered above.

To conclude, we can assess that technology of InGaAs/InAlAs QW is a novelty in the field of pBPM and was developed and proposed within this thesis. These devices are characterized by a very high electron mobility, superior even to that of diamond [41]; furthermore, are able to detect photons of different energies motion, from the visible to the hard X-rays.

Chapter 4

Experimental and Fabrication Techniques

The aim of this chapter is to briefly describe the instruments and techniques employed in this thesis. The first section considers the basic principles of the molecular beam epitaxy (MBE). This section describes the growth apparatus, growth process, the growth calibrations method for GaAs, AlAs, InAs and, in particular, focuses the attention on the MBE machine installed at IOM-CNR. In section 4.2 the fabrication techniques, (UV lithography, chemical etching and metal deposition) are discussed. The next section (4.3) describes transport measurements for electrical characterization. Stylus profile-meters is used to measure a topographical map of the etched surface. Finally, section (4.4) is dedicated to the description of the experimental setups to perform time response of the QW device, position estimation of X-ray and SR and charge collection efficiency for photo-generated carriers measurements.

4.1 Molecular Beam Epitaxy

Molecular beam epitaxy (MBE) is an Ultra-High-Vacuum (UHV)-based technique for producing high quality epitaxial structures with monolayer (ML) control. Since its introduction in the 1970s as a tool for growing high purity semiconductor films, MBE has evolved into one of the most widely used techniques for producing epitaxial layers of metals, insulators, semiconductors, and superconductors, both at the research and the industrial production level. The principle underlying MBE growth is relatively simple: it consists essentially in the production

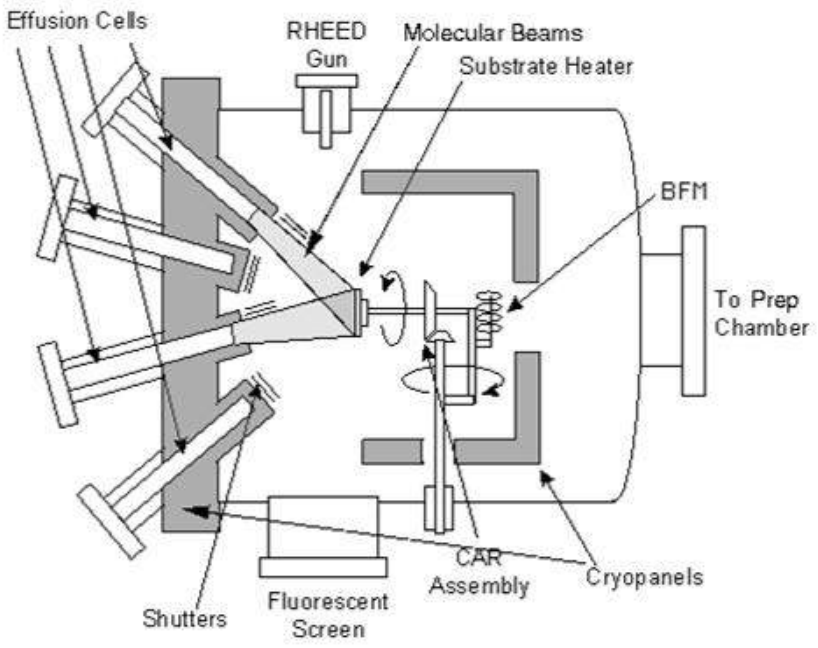

FIGURE 4.1: Schematic drawing of a generic MBE system (top view)

of atoms or clusters of atoms by heating of a solid source. They then migrate in an UHV environment and impinge on a hot substrate surface, where they can diffuse and eventually are incorporated into the growing film. Despite the conceptual simplicity, a great technological effort is required to produce systems that yield the de sired quality in terms of material purity, uniformity, and interface control. An exhaustive discussion on the principles and applications of the MBE technique can be found in Ref. [42].

The choice of MBE with respect to other growth techniques depends on the desired structures and needs. In particular, MBE is the proper technique when abruptness and control of interfaces and doping profiles are needed, thanks to the low growth temperature and rate. Besides, the control on the vacuum environment and on the quality of the source materials allows a much higher material purity, as compared to non UHV based techniques, especially in Al containing semiconductors for applications in high mobility and high speed devices.

4.1.1 MBE Growth Apparatus

A schematic drawing of a standard MBE system is shown in Fig. 4.1. Some basic components are:

- The *vacuum system* consists in a stainless-steel growth chamber, UHV connected to a preparation chamber, where substrates are degassed prior to growth. All the components of the growth chamber must be able to resist bake-out temperatures of up to 200^{o}C for extended periods of time, which are necessary to minimize outgassing from the internal walls .

- The pumping system must be able to efficiently reduce residual impurities to a minimum. The pumping system usually consists of ion pumps, with auxiliary Ti-sublimation and cryogenic pumps, for the pumping of specific gas species. Typically the base pressure of an MBE chamber is from 10^{-11} to 10^{-12} mbar, which determines an impurity concentration below 10^{15} cm^{-3} in grown structures.

- *Liquid N_2 cryopanels* surround internally both the main chamber walls and the source flanges. Cryopanels prevent re-evaporation from parts other than the hot cells and provide thermal isolation among the different cells, as well as additional pumping of the residual gas.

- *Effusion cells* are the key components of an MBE system, because they must provide excellent flux stability and uniformity, and material purity. The cells (usually from six to ten) are placed on a source flange, and are co-focused on the substrate to optimize flux uniformity. The flux stability must be better than 1% during a work day, with day-today variations of less than 5% [43]. This means that the temperature control must be of the order of $\pm 1^o$C at 1000^{o}C [42]. The material to be evaporated is placed in the effusion cells. A mechanical or pneumatic shutter, usually made of tantalum or molybdenum, is placed in front of the cell, and it is used to trigger the flux coming from the cell (see Fig. 4.1).

- The *substrate manipulator* holds the wafer on which the growth takes place. It is capable of a continuous azimuthal rotation around its axis to improve the uniformity across the wafer. The heater behind the sample is designed to maximize the temperature uniformity and minimize power consumption and impurity outgassing. Opposite to the substrate holder, an ionization gauge is placed which can be moved into the molecular beam and is used as a beam flux monitor (BFM).

- The *Reflection High Energy Electron Diffraction* (RHEED) gun and detection screen are used to calibrate precisely the material fluxes evaporated by the effusion cells; with

RHEED it is possible to monitor the epitaxial growth ML by ML. A thorough description of this tool is given in Section (4.1.3)

4.1.2 MBE Growth processes

In general, three different phases can be identified in the MBE process [42]. The first is the crystalline phase constituted by the growing substrate, where short- and long-range order exists. On the other extreme, there is the disordered gas phase of the molecular beams. Between these two phases, there is the near-surface region where the impinging molecular beams interact with the hot substrate. This is the phase where the phenomena most relevant to the MBE process take place. Atomic or molecular species get physisorbed or chemisorbed on the surface where they can undergo different processes Fig. 4.2.

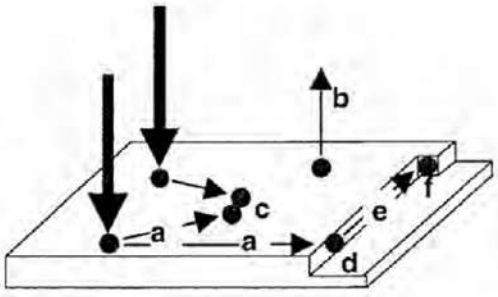

FIGURE 4.2: Different surface elemental processes in MBE

Atoms can diffuse on a flat surface (a), where they can re-evaporate (b), meet other atoms to form two-dimensional clusters (c), reach a step where they can be incorporated (d), or further migrate along the step edge (e) to be incorporated at a kink (f).

The MBE growth of III-V semiconductors uses the so called three temperatures method [42], in which the substrate is kept at an intermediate temperature between the evaporation temperature of the group III and group V source materials. Group V species have a much higher vapor pressure than group III atoms, therefore typical cell working temperatures are lower for group V evaporation (around 300^0C for As) than for group III species (around 1100^0C, 800^0C and 1000^0C, for Al, In, and Ga, respectively).

At the substrate temperature, the vapor pressure of group III species is nearly zero; this means that every atom of the III species that impinges on the substrate is chemisorbed on

its surface; in other words group III atoms have a unit sticking coefficient. The high vapor pressure of the group V species favors, on the contrary, the re-evaporation of these species from the sample surface. Due to the higher group V species volatility with respect to group III, growth is usually performed with an V/III beam flux ratio much higher than one. This flux imbalance does not affect the one-to-one crystal stoichiometry between III-V species. In fact, as shown by [43, 44], in the case of homoepitaxial growth of GaAs, As atoms do not stick if Ga atoms are not available on the surface for bonding. So, in the case of GaAs, the growth rate is driven by the rate of impinging Ga atoms on the substrate. The flux J of atoms evaporated from an effusion cell can be described as

$$J = 1.11 \times 10^{22} \times \left[\frac{aP}{d^2\sqrt{MT}}\right] \cos\theta \quad \text{molecules cm}^{-2}\text{s}^{-1} \tag{4.1}$$

where a is the aperture area of the effusion cell, d is the distance of the aperture to the sample, θ is the angle between the beam and the normal to substrate, M is the molecular weight of the beam species, T the temperature of the source cell, and P is the vapor pressure of the beam; the vapor pressure is itself a function of the source cell temperature as

$$\log P = \frac{A}{T} + B\log T + C \tag{4.2}$$

where A, B and C are material-dependent constants. For a growth rate of about 1 μm/h the typical fluxes are $\sim 10^{16}$ atoms cm^{-2} s^{-1} for group V elements and $\sim 10^{15}$ atoms cm^{-2} s^{-1} for group III.

In the case of alloys with mixed group III elements, such as InGaAs and InAlAs, the reactions with the group V elements are identical to those observed in the growth of binary compounds, such as GaAs [43, 44]. The only difference is that the optimum growth temperature range is driven by the less stable of the two group III atoms, i.e. by indium in the case of InGaAs and InAlAs alloys. In fact, [45] observed that the incorporation of In in InAlAs alloys grown on GaAs substrates decreases for samples grown at temperatures higher than 500^{o}C, while significant Ga or Al re-evaporation takes place only at higher temperatures (about 650^{o}C for Ga, and about 750^{o}C for Al).

In the case of substrate temperatures below 500^{o}C a unit sticking coefficient can be assumed for the growth of In-based alloys; the resulting growth rate and composition are simply

derived from the two binary growth rates that form the alloy. For example if R_{InAs}, and R_{GaAs} are the growth rates for InAs and GaAs respectively, then the total growth rate of the alloy is $R_{InGaAs} = R_{InAs} + R_{GaAs}$ while the indium concentration x is the same as in the gas phase and is given by

$$x = \frac{R_{InAs}}{R_{InAs} + R_{GaAs}} \tag{4.3}$$

4.1.3 Growth calibration

To grow ternary alloys as $In_xGa_{1-x}As$ and $In_xAl_{1-x}As$ with known indium concentration x, it is necessary to measure accurately, prior to growth, the three growth rates R_{GaAs}, R_{AlAs}, and R_{InAs}.

GaAs and AlAs

The growth rates of GaAs and AlAs are determined by the intensity oscillations of the specular spot of the RHEED signal during the growth of a GaAs or AlAs film on a GaAs substrate [42]. This technique employs a high energy (up to 20 keV) electron beam, directed on the sample surface at grazing incidence (a few degrees); the diffraction pattern of the electrons is displayed on a fluorescent screen and acquired by a CCD. Thanks to the grazing incidence and the limited mean free path of electrons in solids, the electron beam is scattered only by the very first atomic layers, giving rise to a surface-sensitive diffraction pattern. Besides, the grazing geometry limits the interference of the RHEED electrons with the molecular beams, making the technique suitable for real-time analysis during growth. During crystal growth the intensity of the zero order diffraction spot (the specular spot) is recorded as a function of time. An example of such measurements is shown in the left panel of Fig. 4.3, where it can be noticed that the intensity of the spot has an oscillatory behavior. This happens because a flat surface, present when a ML is complete, reflects optimally the electrons while in a condition in which a half-ML has been deposited the electron beam gets partially scattered by the stepped surface.

As schematically shown in the right panel of Fig. 4.3, starting with a flat surface and proceeding with growth, the incident electron beam gets partially scattered by the islands steps of the growing ML, thus reducing the reflected intensity. Scattering becomes maximum at half

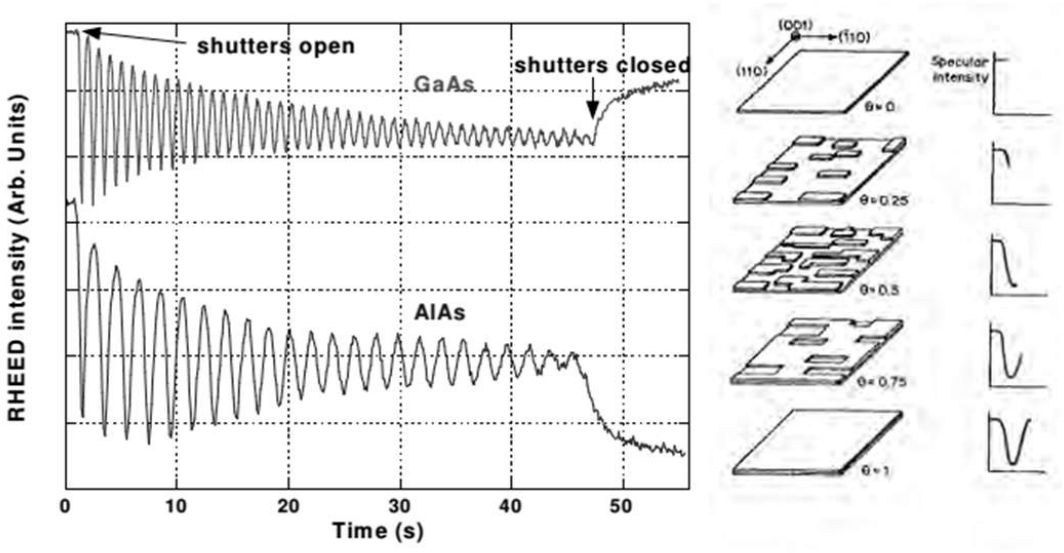

FIGURE 4.3: RHEED oscillations. In the left panel an actual measurement for GaAs and AlAs grown on GaAs (001). In the right panel a schematic view of the relationship between RHEED intensity and monolayer coverage θ.

ML coverage, while as the new ML completes (one Ga or Al plus one As layer) the surface flattens again by coalescence of the islands, and the reflected intensity recovers its value. A progressive dumping of the oscillation intensity is due to an increasing disorder of the growth front as the growth proceeds.

Thus, a period of RHEED oscillation corresponds to the growth of a single ML. By measuring the time necessary to complete a certain number of oscillations one can calculate the growth rate in ML/s for a fixed effusion cell temperature, and easily convert it to units of A/s knowing the lattice parameter of GaAs or AlAs.

This calibration is performed almost daily, prior to sample growth, on a *ad hoc* substrate. The day-to-day variation of R_{GaAs} and R_{AlAs}, with constant cell temperatures is $\sim 1\%$; the long term behavior of these rates, on the other hand is fairly predictable, and is constant (within 1 - 2%) until the cell is almost empty, unless major changes to the cell environment happen (like refilling, etc).

InAs

Unfortunately, InAs growth rates cannot be measured taking advantage of RHEED oscillations. This is because it is very difficult to obtain good quality, ML-flat InAs surfaces on any substrate, and it is virtually impossible on GaAs ones. In fact the large lattice mismatch between InAs and GaAs ($\sim$7.2%) favors the formations of 3D islands even after the first one or two MLs. However the relation (4.3) provides an alternative method to evaluate the InAs growth rate, by in-situ measuring the GaAs growth rate by RHEED oscillations, and the In concentration in a thick InGaAs layer by ex-situ X-ray diffraction measurements.

The indium flux calibration is a time-consuming operation that involves the growth of several samples of $In_xGa_{1-x}As$, and multiple X-ray diffraction measurements on each sample. For this reason, and knowing the relative stability of the fluxes until the cells are almost empty, the In flux calibration is performed only once every few months, after major maintenance operations to the MBE chamber.

4.1.4 The HMMBE system at IOM-CNR

The MBE chamber installed at Laboratorio TASC IOM-CNR in Trieste is mainly dedicated to the growth of GaAs based heterostructures characterized by a very high carrier mobility. Such a system requires some peculiar modifications. Two 3000 l/s cryopumps replace the ion pumps, providing a cleaner, higher-capacity pumping system. All-metal gate valves are mounted to eliminate outgassing from Viton seals. No group-II materials, such as Be, are used for p-doping, since they are known to drastically reduce carrier mobility; a carbon source is used instead for C doping. High-capacity and duplicate cells are used to avoid cell refilling or repairing for extended periods. Extensive degassing and bake out duration (three months at 200^{o}C) were carried out after the installation of the MBE system to increase the purity of the materials.

4.2 Fabrication techniques

In this chapter we are presenting the fabrication techniques exploited in the QW samples production. The main fabrication technique we used is UV Lithography (UVL) followed by wet

FIGURE 4.4: Photo of the high-mobility MBE system at TASC-IOM-CNR, Trieste

etching. Metal deposition technique was introduced to create readout electrodes.

4.2.1 Photo-lithography

Photolithography is one of the most common lithography techniques. It uses light (UV) to transfer a pattern from a photomask to a photoresist.

Resist

A photoresist is a solution composed mainly by a polymer, a sensitizer and a casting solvent. The polymer changes structure when exposed to radiation, the sensitizer controls the photo chemical reactions, the solvent allows the deposition of the resist on the substrate and the formation of thin layers on the surface to be covered. The tone of the photoresist describes its behavior to exposure. When the photoresist is of the *positive* type, the photochemical reaction during exposure weakens the polymer causing scission of the main and side polymer chains, resulting in a higher solubility of the exposed resist. The development rate of the exposed resist is, then, faster than the development rate of the unexposed resist. When the photoresist is of the type called negative, the exposure causes the strengthening of the polymer by random cross-linkage of main or pendant side chains, becoming less soluble. Fig. 4.5 shows exposure effects on both positive and negative resist.

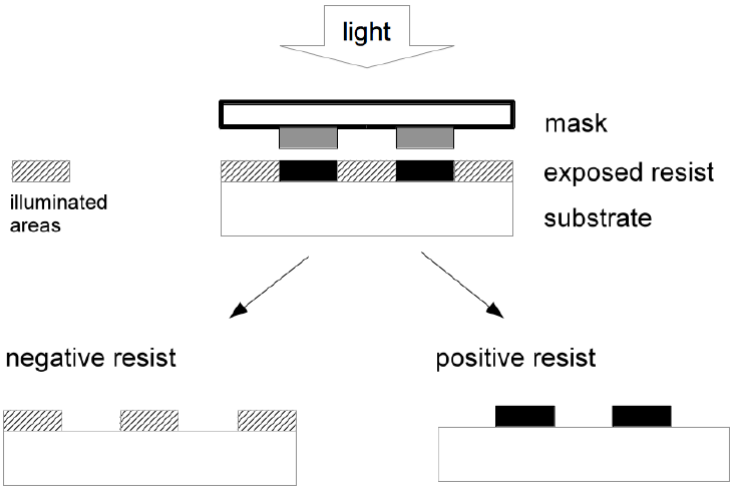

FIGURE 4.5: Negative and positive resist behavior to exposure. Positive exposed resist is removed during development, negative exposed resist remains.

Spin coating

One of the techniques used to cover a surface with a thin, homogeneous layer of photoresist is the spin coating. The photoresist is dispensed from a viscous solution onto the sample, which is then spun at high speed. The spinner vacuum chuck holds the sample in place. The speed at which the sample is spun varies from 500 to 8000 revolutions per minute (rpm) and depends on the viscosity of the resist and the required film thickness. At these speeds, centrifugal forces causes the solution to flow to the edges, where it builds up until the surface tension is exceeded. The rotation at high speed causes the resist to deposit homogeneously. The resist thickness is a function of spin speed, solution concentration and molecular weight and can be valued using the empiric expression [46]:

$$T = \frac{KC^{\beta}\eta^{\gamma}}{\omega^{\alpha}} \tag{4.4}$$

where K is a calibration constant, C the polymer concentration in $g/100ml$ solution, η the intrinsic viscosity, ω the speed (rpm) and α, β, γ parameters to be determined. The quality of resist coating determines the density of defects transferred to the final structure. After spin coating the resist still contains up to 15% solvent and may contain stresses: the resist covered sample is then soft baked (this operation is also known as *pre exposure bake*), to promote residual solvent evaporation, surface adhesion and to reduce the stresses. Temperature and time

of the soft bake are specific to every resist. The negative resist often requires a post exposure bake after exposure to enhance cross-linkage.

UV Lithography

One of the advantages of UV lithography is the high throughput with resists of moderate to fast sensitivity. The primary limitations are resolution due to diffraction and substrate reflectivity. Diffraction affects resolution, since the image projected on the resist becomes increasingly blurred as the dimensions decrease, while substrate reflectivity affects line-width control, because of the standing waves in the resist and the effect of interference at the air-resist interface on coupling of the incident exposure dose into the resist.

The photomask is composed by flat glass or quartz substrate, transparent respectively to near and deep ultraviolet, and an absorber pattern metal layer, usually chromium, opaque to UV. The mask is placed in direct contact with the resist covered substrate and light, passing through the photomask, exposes the area of the resist not protected by the mask absorber pattern. In this way, a 1:1 image of the mask is transferred from the mask to the photoresist. Optical lithography is generally the most cost effective lithography technique.

The optical lithography (Karl Süss MJB3) at TASC-IOM-CNR clean room works with 300 W Hg light source at 405 nm wavelength. A spatial resolution and an accuracy of a mask aligner are 500nm.

4.2.2 Chemical Etching

The procedure by which material is removed in a controlled way from a substrate is defined as etching and it can be performed as wet or dry etching. In the former the detachment of material is happening in a liquid, while in the latter the material is transferred into the gaseous phase. The use of wet etching techniques has a long history in treating surfaces and materials.

Nowadays the etching techniques have become a key process for the fabrication of semiconductor microdevices and microcomponents since they allow a much more refined removal from a solid surface compared to mechanical methods. This is very important since in modern microelectronics, structures in the sub-micrometer range are needed. The etching

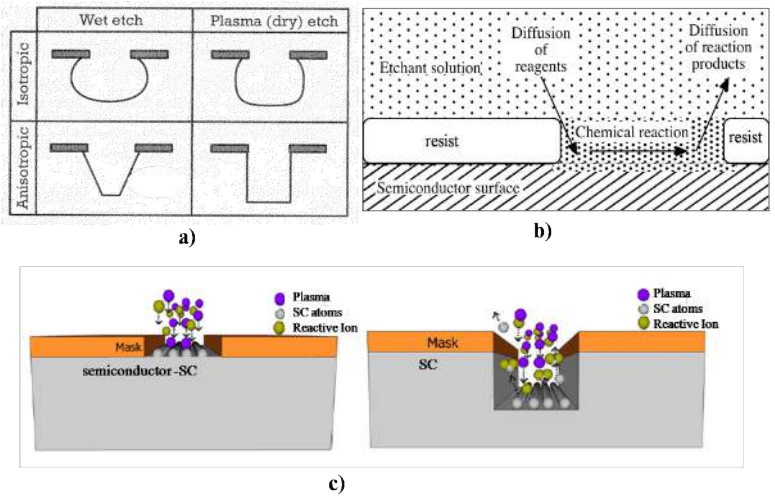

FIGURE 4.6: Wet chemical etching

of semiconductors in liquid reactants is in fact widely used at all stages of the microsystem technology, such as for removing contaminants from the wafers, for creating three-dimensional structures, for revealing buried layers to define electrical contacts, etc.

When a material is attacked by a liquid or vapor etchant, it is removed isotropically (uniformly in all directions) or anisotropically. The difference between isotropic etching and anisotropic etching is shown in Figure 4.6a. Material removal rate for wet etching is usually faster than the rates for many dry etching processes and can easily be changed by varying temperature or the concentration of active species. Wet etching is a material removal process that uses liquid chemicals or etchants to remove materials from a wafer (Fig. 4.6b). The specific patters are defined by masks on the wafer. Materials that are not protected by the masks are etched away by liquid chemicals. These masks are deposited and patterned on the wafers in a prior fabrication step using lithography.

In dry etching, plasmas or etchant gases remove the substrate material. The reaction that takes place can be done utilizing high kinetic energy of particle beams, chemical reaction or a combination of both. Physical dry etching requires high kinetic energy (ion, electron, or photon) beams to etch off the substrate atoms. When the high energy particles knock out the atoms from the substrate surface, the material evaporates after leaving the substrate. There is no chemical reaction taking place and therefore only the material that is unmasked will be removed. Chemical dry etching (also called vapor phase etching) does not use liquid chemicals or etchants. This process involves a chemical reaction between etchant gases to attack the surface. Reactive ion etching (RIE) uses both physical and chemical mechanisms to achieve

high levels of resolution (Fig. 4.6c). The process is one of the most diverse and most widely used processes in industry and research [47].

4.2.3 Metal evaporation

Metal evaporation is a thin film deposition method. A metal evaporator consist of a vacuum chamber where the source material (a metal) is heated until it evaporates and the vapor particles condense on the sample. The material to be deposited is loaded into a heated container, the crucible. It can be heated simply by an embedded resistance heater (thermal method) or by an electron beam (electron-beam method). Due to the very low pressure in chamber (10^{-5}-10^{-7}mbar), the atoms of the vapor travel across the chamber in a straight line until they impact on a surface where they accumulate as a film. Some evaporation systems may contain many crucibles in order to perform multiple material deposition without breaking vacuum. They may contain a large number of wafers suspended above the crucibles.

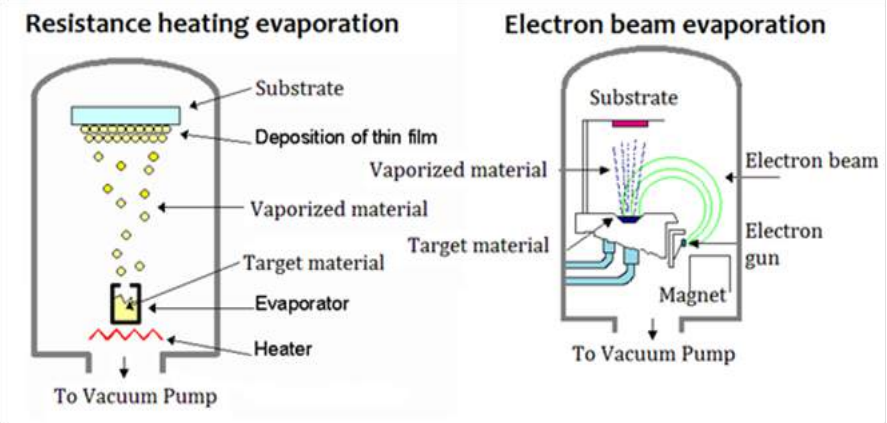

FIGURE 4.7: Metal deposition

Deposition rate is commonly measured using a quartz crystal rate monitor. A feedback may be used to control the crucible heating in order to maintain a constant deposition rate. The main disadvantage of metal evaporation, the discontinuity to cover surface topology, in particular the vertical walls, may be exploited for lift-off processes or tilted deposition.

4.3 Characterization techniques

4.3.1 Transport measurement

The van der Pauw method [48] is one of the most utilized measurement methods for the evaluation of electrical properties in semiconductor materials, such as resistivity, carrier density, and mobility. The van der Pauw method can be used to measure samples of arbitrary shape, although several basic sample conditions must be satisfied to obtain accurate measurements, for instance, the thickness of the sample must be constant, point contacts placed at the edges of the samples must be used for the measurements, and the sample quality has to be homogeneous. Most semiconductor samples satisfy these conditions, so that this convenient measurement method has been widely utilized. The most indicated shape of the samples for a correct VdP measurement is square with point ohmic electrodes contacted at the four corners. The arrangement of the electrodes with schematics of the van der Pauw method are shown in Figure 4.8 a) and b).

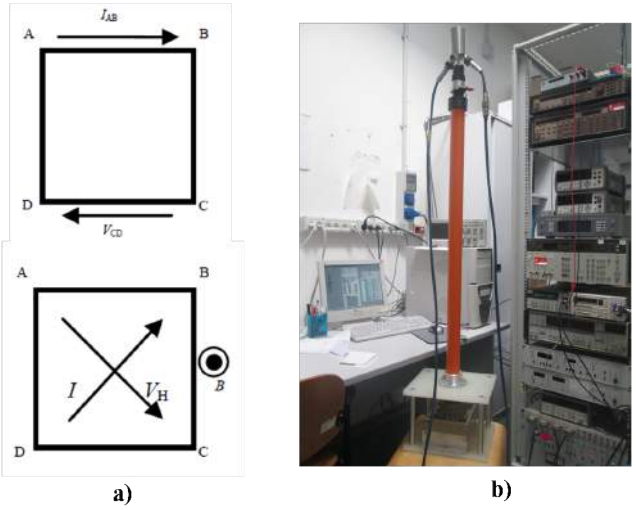

FIGURE 4.8: Schematic illustrations of a) resistivity and Hall effect measurements by the van der Pauw method; b) The measurement setup in the laboratory

For resistivity measurements, a voltage is applied to flow current I_{AB} along one side of the square sample and the voltage along the opposite side, V_{CD}, is measured. For Hall effect measurements, a voltage is applied between the contacts placed at diagonally opposite corners and the current I flowing between them is measured. In addition, a magnetic field B is applied perpendicular to of the sample surface, and the change in voltage V_H, between the

point contacts placed at diagonally opposite corners is measured. Resistivity ρ, carrier density n, and mobility μ, are calculated from the measured values, applied magnetic fields and the film thickness d, of the measured sample. Equations 4.5 to 4.10 are used to calculate the electrical properties:

$$\rho = \frac{\pi d}{ln2} \cdot \frac{(R_{AB,CD} + R_{BC,DA})}{2} \cdot f \tag{4.5}$$

where f is correction function that can be numerically calculated through the relation [49]:

$$\frac{R_{AB,CD} - R_{BC,DA}}{R_{AB,CD} + R_{BC,DA}} = \frac{f}{\ln 2} \arccos\left(\frac{\exp(\ln 2/f)}{2}\right) \tag{4.6}$$

$$R_{AB,CD} = \frac{V_{CD}}{I_{AB}}, \quad R_{BC,DA} = \frac{V_{DA}}{I_{BC}} \tag{4.7}$$

$$R_H = \frac{V_H d}{IB}, \tag{4.8}$$

$$n = \frac{1}{R_H e} \tag{4.9}$$

$$\mu = \frac{R_H}{\rho} \tag{4.10}$$

Our measurements are performed at room temperature. In a typical Hall effect measurement of our samples an 100 nA alternating current at a frequency of 20 Hz is driven inside the device and the voltage drops V_{CD} and V_H are recorded by a lock-in amplifier. V_H was recorded usually with an applied magnetic field of 0.2 Tesla.

4.4 Experimental setups for detector performance

In this section, experimental setups of the light sources on which we have tested QW devices are detailed. Near UV laser light was chosen to test time response of the device (4.4.1). A

conventional X-ray tube (4.4.2) was mainly used to obtain a first estimation of the position of the beam with however a larger spot size then SR beamlines. Both beamlines (4.4.3.1) and (4.4.3.2) used to estimate the beam position in the QW devices have the possibility to set either a very focused beam (" needle beam ") with size down to 70-90 μm or wider beams (200-500 μm). At the end of this section (4.4.4), some details will be given about the setups used to test the detector performance, such as the UHV chamber and the X-Y movable stage.

4.4.1 Near UV laser

Titanium-doped sapphire (Ti^{3+}:sapphire) is a widely used transition-metal-doped gain medium for tunable lasers and femtosecond (fs) solid-state lasers [50]. Optical parametric oscillators and amplifiers can extend wavelength tunability to access the deep-UV ($<$ 200 nm) and mid-IR regions ($>$20 μm) with pulse widths approximately 100 femtoseconds in length.

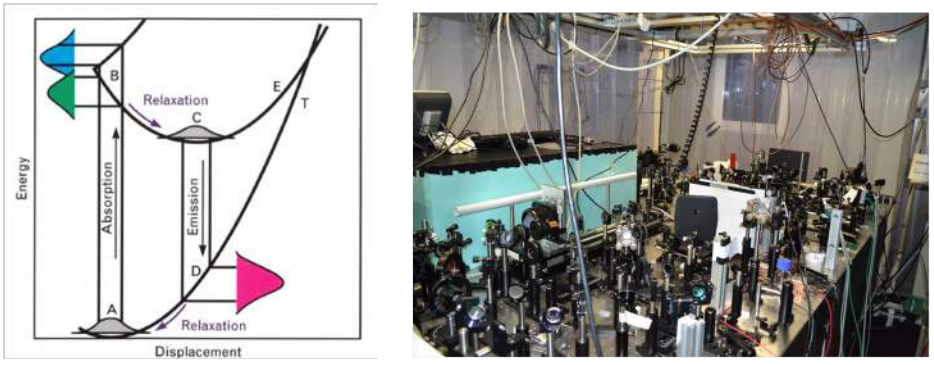

a) **b)**

FIGURE 4.9: a) Ti:AI_20_3 configurational diagram. The energy of the electronic states are plotted with respect to the displacement of the Ti^{3+} ion. Absorption is indicated by the vertical transition from A to B and occurs in the blue and green region of the spectrum as indicated to the left. The emission of light is indicated by the transition from C to D and occurs in the red to infrared region of the spectrum as indicated at the right; b) Near UV laser laboratory

Ultra-fast near UV pulsed laser sources are an efficient tool to characterize the presented QW detectors in terms of time response and position sensitivity. The reported experiments were carried out at the IUVS Support Laboratory of Elettra through a 400 nm titanium-sapphire laser emitting 100 fs wide pulses at a 1 kHz repetition rate (Fig. 4.9). The laser beam was focused in order to obtain a 100 μm spot on the surface of the QW sensor. The power of the impinging photon pulse was varied during the tests to check the dependence of photo-generated charges. The signals from the readout pads were acquired through a 40 GS/s oscilloscope.

4.4.2 Conventional X-ray tube

Conventional x-ray tubes are vacuum tube diodes, with their filaments biased. Electrons are emitted thermionically from the filament, and accelerate into the anode, which is maintained at ground potential. The operating voltage and current of an x-ray tube are typically selected to optimize the emission of characteristic radiation. For a particular accelerating voltage, the intensity of all radiations increases with the electron current in the tube. The effect of accelerating voltage on characteristic x-ray emission is more complicated, however, since the spectrum of x-rays is affected. Characteristic x-rays are excited more efficiently with higher accelerating voltage, V . In practice the intensity of characteristic radiation depends on V as:

$$I_{characteristic} \propto (V - V_c)^{1.5} \tag{4.11}$$

where V_c is the energy of the characteristic x-ray. On the other hand, continuum radiation (somewhat improperly called bremsstrahlung, meaning "braking radiation") can be emitted when an electron undergoes a strong deflection causing an acceleration. This acceleration can create an x-ray with an energy as high as the full kinetic energy of the incident electron, E_0(equal to its charge, e, times its accelerating voltage, V). "Duane–Hunt rule" shows the shortest x-ray wavelength from the anode, λ_{min} [51]

$$E = h\nu = h\frac{c}{\lambda}, \quad E_0 = eV, \quad \Rightarrow \frac{h\nu}{eV} = \lambda_{min}[A] \tag{4.12}$$

Moreover, the intensity of the bremsstrahlung increases approximately as:

$$I_{bremsstrahlung} \propto V^2 Z^2 \tag{4.13}$$

To maximize the characteristic x-ray intensity with respect to the continuum:

$$\frac{d}{dV}\frac{I_{characteristic}}{I_{bremsstrahlung}} = \frac{d}{dV}\frac{(V - V_c)^{1.5}}{V^2} \tag{4.14}$$

Combining the bremsstrahlung and characteristic x-ray intensities gives wave length distributions as shown in Fig. 4.10a. For this example of an x-ray tube with a silver anode, the

characteristic K_α lines (22.1 k eV, 0.56 $\AA$) are not excited at tube voltages below 25.6 k eV, which corresponds to the energy required to remove a K-shell electron from a silver atom [52].

In our measurement, the conventional crystallographic X-ray tube with silver target used to estimate a beam position only. Such a source provides a white beam with photon energies ranging from 6 keV to 50 keV with an intensity peak at 22 keV. The spot size has been reduced by a pinhole and a double-slit collimator from 200 to 500 μm (FWHM) at the interaction point.

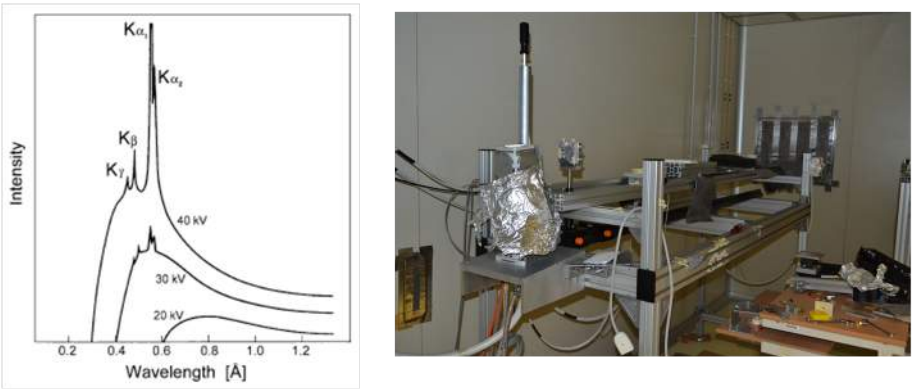

FIGURE 4.10: a) Intensity spectrum (in wavelength) of an x-ray tube with a silver anode; b) Conventional X-ray tube laboratory

4.4.3 Synchrotron Radiation

Synchrotron radiation is a light source for a variety of applications. High flux and collimation, energy tunability, and timing capabilities are some special features of synchrotron radiation sources. These facilities are centered around an a storage ring with where electrons travel close to the speed of light. Their energy losses are primarily in the electron mass, not velocity (which stays close to the speed of light), so the bunches remain intact. The electrical power needed to replenish the energy of the electrons is provided by a radio frequency electric field. This cyclic electric field accelerates the electron bunches by alternately attracting and repelling them as they move through a dedicated section of the storage ring [51].

Synchrotron radiation is generated by the dipole bending magnets used for controlling the electron orbit in the ring, but all modern " third generation " synchrotron radiation facilities derive their x-ray photons from " insertion devices," which are magnet structures such as "

wigglers ” or “ undulators”. Undulators comprise rows of magnets along the path of the electron beam. Synchrotron radiation is produced when the electrons accelerate under the Lorentz forces of the row of magnets. The mechanism of x-ray emission by electron acceleration is essentially the same as that of bremsstrahlung radiation (4.4.2).

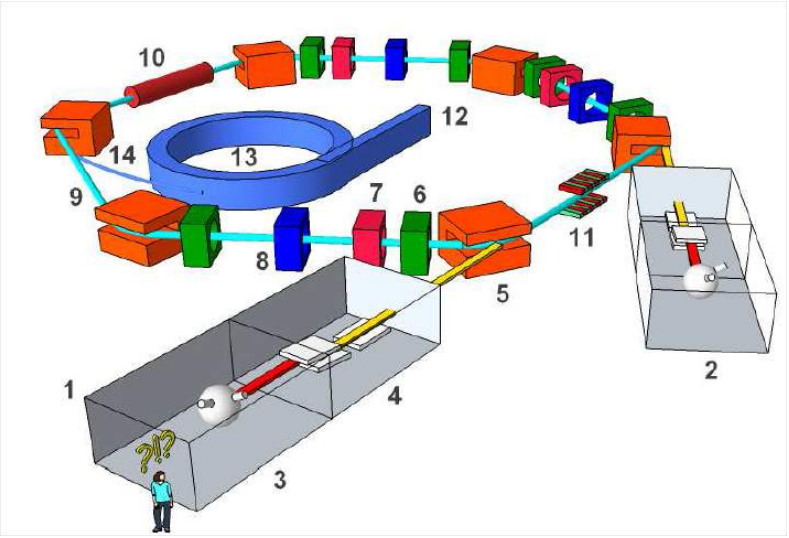

FIGURE 4.11: Simplified representation of the structure of a third-generation synchrotron; forms, scales and composition are indicative; 1) beamline from undulator ; 2) beamline from bending; 3) experimental hutch; 4) optical hutch; 5) bending magnet; 6) quadrupole magnet; 7)sixfold magnet; 8) magnet steering; 9) vacuum chamber of the storage ring; 10) RF cavity; 11) device insertion; 12) linear accelerator (linac); 13) booster; 14) transfer line.

Various figures of merit describe how x-ray sources provide useful photons. The figure of merit for operating a monochromator is proportional to the intensity (photons/s) per area of emitter, but another factor also must be included. For a highly collimated x-ray beam, the monochromator crystal is small compared to the distance from the source. It is important that the x-ray beam be concentrated into a small solid angle so it can be utilized effectively. The full figure of merit for monochromator operation is “brightness” (often called “brilliance”), which is normalized by the solid angle of the beam. The brightness of an undulator beam can be 10^9 times that of a conventional x-ray tube. Brightness is also a figure of merit for specialized beamlines that focus an x-ray beam into a narrow probe of micron dimensions.

4.4.3.1 X-ray Fluorescence beamline

The X-ray Fluorescence (XRF) beamline is a highly versatile beamline at Elettra – Sincrotrone Trieste S.C.p.A. The beamline is optically designed to present the beam parameters needed for

high-level measurements in spectroscopy as well as in microscopy. In particular, experimental chambers can be placed temporarily at the beamline to make use of either a monochromatic beam (δE/E = 1.5 $\times$ 10^{-4}) or a white beam [53]. Our experiments were performed with monochromatic beams at photon energies of 2.14 keV, 5 keV and 10 keV, respectively. A photon flux of 10^8 ph/s was roughly estimated by an ion chamber for the two higher energies with a spot size of 200 μm. Since photon absorption of air increases below 4 keV, the spot size of the beam at 2.14 keV was set to 500 μm, in order to reach a comparable value of the impinging flux (3×10^8 ph/s). The position of the beam was estimated and charge collection efficiency (CCE) for photo-generated carrier was calculated at those energies. Additionally, the beam size was set as $\sim$70 μm with energy of 7 keV for the measurements only of the position estimation.

FIGURE 4.12: X-ray Fluorescence beamline at Elettra – Sincrotrone Trieste S.C.p.A

4.4.3.2 SYRMEP beamline

The optics of the SYRMEP beamline, Elettra – Sincrotrone Trieste S.C.p.A is based on a double-crystal Si (111) monochromator which was set in a range from 10 keV to 22 keV [54]. The beamline provides, at a distance of about 20 m from the source, a monochromatic, laminar-section X-ray beam which was shaped to a spot of either 90$\times$90 or 500$\times$500 μm^2 in our measurement by means of motorized slits. The total fluxes were estimated as order of 10^7-10^8 for utilized energies by the ion chamber currently used for beam diagnostic at SYRMEP. We had position estimation measurements at 10 keV, 11 keV, 14 keV and 20keV with spot size of 90$\times$90 μm^2. A beam with energies of 15 keV, 17 keV, 20keV and 22 keV with bigger spot of 500$\times$500 μm^2 was used to evaluate CCE for the device.

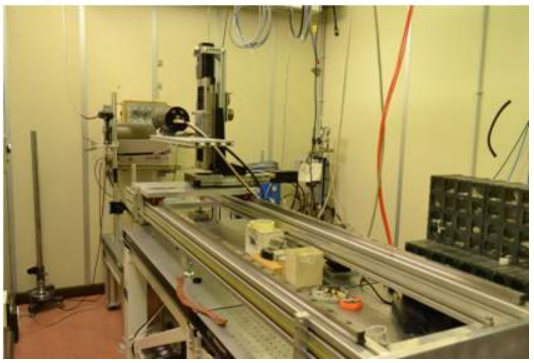

FIGURE 4.13: SYRMEP beamline, Elettra – Sincrotrone Trieste S.C.p.A

4.4.3.3 MCX beamline

MCX beamline at Elettra (Fig. 4.14) allows to perform a wide range of non-single crystal diffraction experiments: grazing angle diffraction and reflectivity, residual stress and texture analysis, phase identification and structural studies and kinetic studies [55]. Systems that can be investigated vary from organic and inorganic thin films, to thermally and/or mechanically modified surfaces of mechanic components, to polymers, catalysts and highly disordered materials in the form of films, powders, fibers. In addition to the scientific heritage, a valuable activity will be the support to technology and industrial production, both for specific tasks of non-destructive control and for the development of new products. The beam was set at 10 keV with blade beam ($100\times600\mu$m) for line scans on our devices. Estimated photon flux is of the order of 10^9 ph/s.

FIGURE 4.14: a) the board; b) Chamber for UHV with coaxial receptacles

4.4.4 Detector performance setups

The QW device was placed on a carrier board (Fig. 4.15a) and the top electrical contacts were wire-bonded into the readout pins. The board was mounted in a measurement chamber (Fig. 4.15b) resting on a translator in order to perform X–Y movements with sub-micrometric precision. The actuators were computer driven using a software developed in Labview, allowing to correlate the readout signal with the position, thus reconstructing a 2D mapping of the point-to-point device photo-response. The readout of the signal was carried out using a four-channel AH501 picoammeter [56], fabricated by Elettra — Sincrotrone Trieste S.C.p.A. The generated photocurrents have been read by means of four different multi-channel acquisition systems, which work at low and high sampling frequencies.

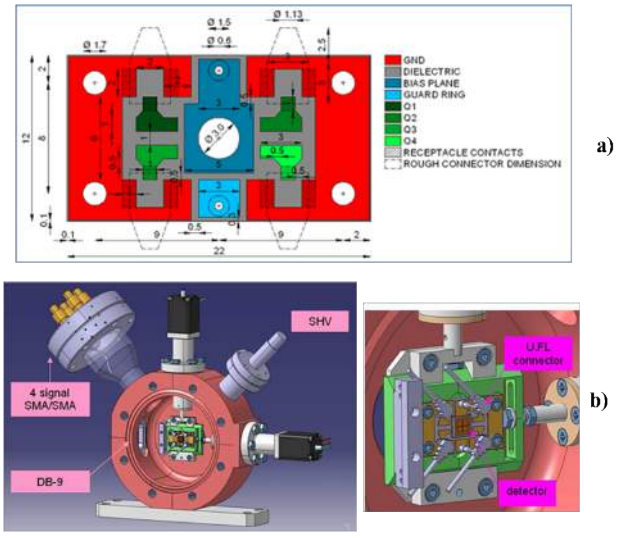

FIGURE 4.15: a) the board; b) Chamber for UHV with coaxial receptacles

Chapter 5

Device fabrication

The first section of this chapter describes the growth of the QW devices, in particular, the growth of the metamorphic InGaAs/InAlAs quantum well and the $In_xAl_{1-x}As$ graded buffers optimized to accommodate our $In_{0.75}Ga_{0.25}As$ QWs on GaAs substrates. We have developed four different configurations for the device, which are described in the present chapter. Pixelation was applied either on the QW side, on the back side or on both sides. Finally, we have developed a free-standing device in which the whole GaAs substrate was removed.

5.1 Sample growth and transport experiments

The growth of good quality $In_{0.75}Ga_{0.25}As$ QW is made very difficult by the absence of suitable substrates. In order to grow high electron mobility 2DEGs in virtually unstrained, defect-free $In_{0.75}Ga_{0.25}As$, a virtual substrate can be adopted, which matches the $In_{0.75}Ga_{0.25}As$, lattice parameter to that of commercially available substrates. In this section, lattice-mismatched growth of virtual substrates based on $In_xAl_{1-x}As$ graded buffers is described.

5.1.1 Lattice-mismatched growth

Apart from a few lucky exceptions, crystals of different semiconductors have different lattice parameters or even different crystal structures. This makes it very difficult to grow heterostructures without the formation of crystal defects. The most notable exception is that of GaAs/AlAs

and their alloys. In fact not only GaAs and AlAs crystals have both a zincblende structure, but their lattice parameters differ so little that virtually any thickness of any alloy of these binaries can be grown without having to worry about strain buildup (Fig. 5.1). Moreover, the band gaps of GaAs and AlAs are very different, so that conduction band engineering can be easily done in AlGaAs/GaAs systems. GaAs/AlGaAs multilayers have been used to fabricate (by a number of growth techniques) a variety of high quality electronic and photonic devices. As can be seen in Figure 5.1, the situation for InAs (and thus $In_xGa_{1-x}As$ alloys) is not as good: the lattice mismatch between InAs and the most common III-V commercial substrate, GaAs, is huge (almost 7%), and with InP (the other commercially available substrate) it is more than 3%.

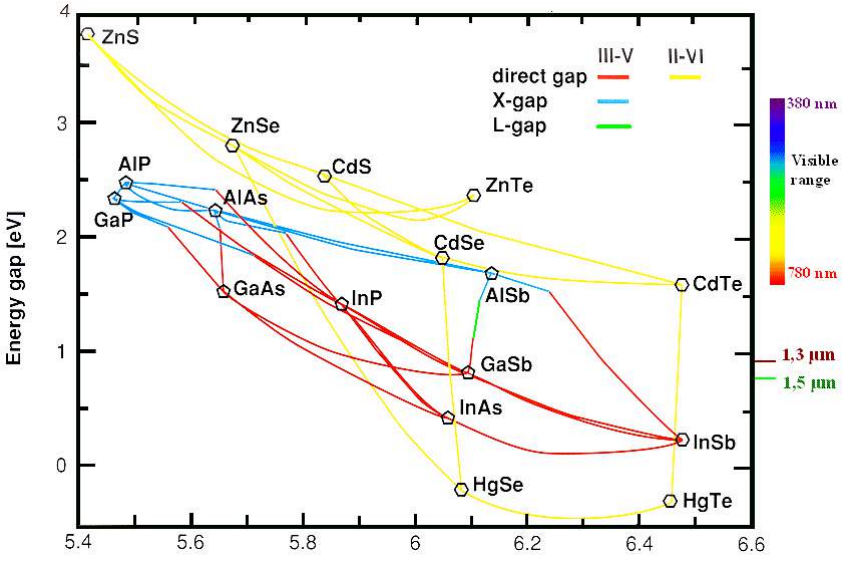

FIGURE 5.1: Band gaps and lattice parameters of most binary semiconductors. GaAs, AlAs, InAs and their ternary alloys are brightly colored (re-elaborated from [57]).

The only possible lattice-matched growth of an $In_xGa_{1-x}As$ alloy is with x = 0.53 on InP. This was not a suitable choice in our case for two reasons: first, our target was $x \gtrsim 0.75$, so strain build up would have been a problem anyhow; second, phosphorus is a contaminant for high mobility 2DEGs in GaAs/AlGaAs, so InP can not be used as substrate in our MBE chamber.

Thus the only choice has been using GaAs as a substrate, and find a way to relax the strain to grow $In_{0.75}Ga_{0.25}As$ layer with a low defect density in the active region of the structure.

Strained Heteroepitaxy

Whenever growing an epilayer with a different lattice parameter than the substrate, strain will build up in the epilayer. This strain can be either *compressive*, when the epilayer has a larger lattice parameter than the substrate (as is the case for $In_xGa_{1-x}As$ grown on GaAs), or *tensile*, in the opposite case. In both cases the first atomic layers of the growing film tend to have the in-plane lattice parameter matched to that of the substrate, and to expand or compress the out of plane lattice parameter to accommodate the misfit (the so called *pseudomorphic* growth). This, however, has an energy cost payed in elastic energy accumulation within the crystal. When this elastic energy exceeds the energy cost of a crystal defect, the defect becomes energetically favorable and tends to form throughout the interface between the epilayer and the substrate.

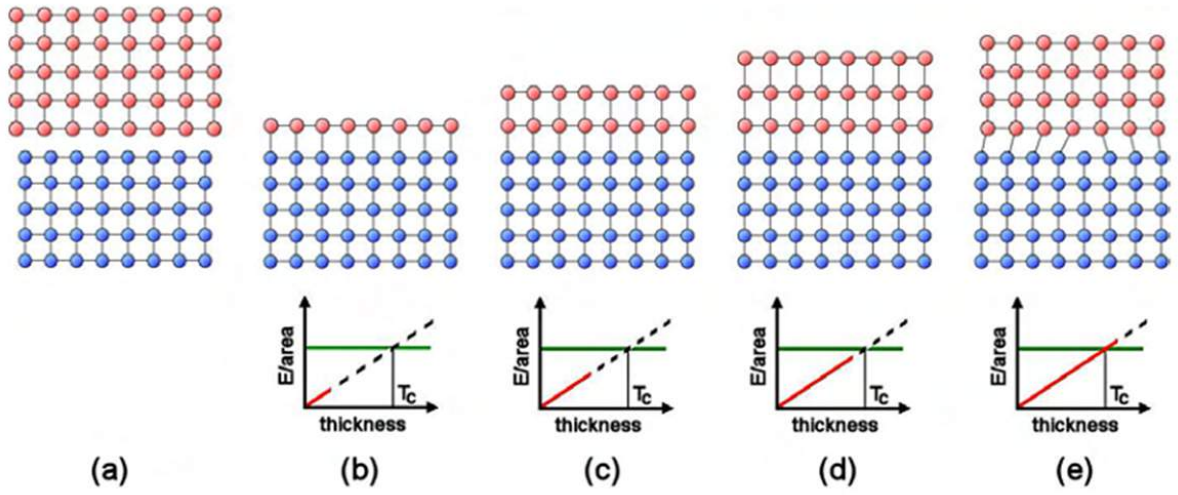

FIGURE 5.2: Growth of a mismatched layer (red) on a substrate (blue) beyond the critical thickness T_c. In (a) a representation of the "bulk" fully relaxed materials; (b)-(e) are the various phases of growth. Below the cartoons are shown the graphs of elastic energy per unit area versus epilayer thickness. The horizontal green line represents the critical energy for dislocation formation

This process is depicted in Figure 5.2. The thickness at which defects start forming is called *critical thickness*. The growth of an epilayer beyond the critical thickness, with the formation of crystal defects (in the form of dislocations) that possibly lead to the full relaxation of the epilayer, is referred to as *metamorphic*.

For a given thickness of the strained film the formation of dislocations is a function of the lattice mismatch; in practice the slope of the line of the graphs of Fig. 5.2 gets steeper as

the lattice mismatch increases, thus reducing the critical thickness. This means that in order to grow dislocation-free lattice mismatched layers there are only two strategies:

- for small lattice mismatch: to grow pseudomorphic strained layers below the critical thickness;
- for large lattice mismatch: to grow first a buffer layer where strain relaxation through misfit dislocations formation takes place, i.e. to obtain a virtual substrate lattice-matched to $In_xGa_{1-x}As$.

$In_{0.75}Ga_{0.25}As$ QW growth

In order to obtain defect free active regions of $In_{0.75}Ga_{0.25}As$, step graded $In_xAl_{1-x}As$ buffer layers (BL) with increasing indium concentration x was grown on GaAs (001) wafers. The growth procedure, schematically represented in Fig. 5.3, can be divided in three phases characterized by different growth temperatures:

- *Substrate preparation*. The growth starts with an epiready GaAs (001) wafer degassed at 580^{o}C to remove the surface oxide. Then a 200 nm thick undoped GaAs layer followed by a 20 period GaAs/ $Al_{0.33}Ga_{0.67}As$ (8 nm/2 nm) superlattice and a second 200 nm undoped GaAs layer are grown at 600^{o}C. These three layers have several purposes: to reduce the wafer roughness, the diffusion of interface impurities in the grown layer, and to reduce the risk of threading dislocation formation during the subsequent phase, as pointed out in Ref. [58]. They are grown at this temperature since it is the optimal growth temperature to obtain high quality GaAs.
- *Buffer growth*. The substrate temperature is decreased to 330^{o}C and the $In_xAl_{1-x}As$ buffer is grown in 50 nm steps with increasing indium concentration, starting from $In_{0.15}Al_{0.85}As$ up to $In_{0.75}Al_{0.25}As$. The In concentration is varied by increasing the In cell temperature while maintaining the Al flux constant; there is no growth interruption between the steps, so that the interface is not abrupt, since the increase of the In cell temperature takes several seconds. Since only a finite amount of elastic energy can be sustained inside the buffer structure before the onset of plastic relaxation, a wide number of misfit dislocations are present in the region of the buffer closer to the GaAs substrate,

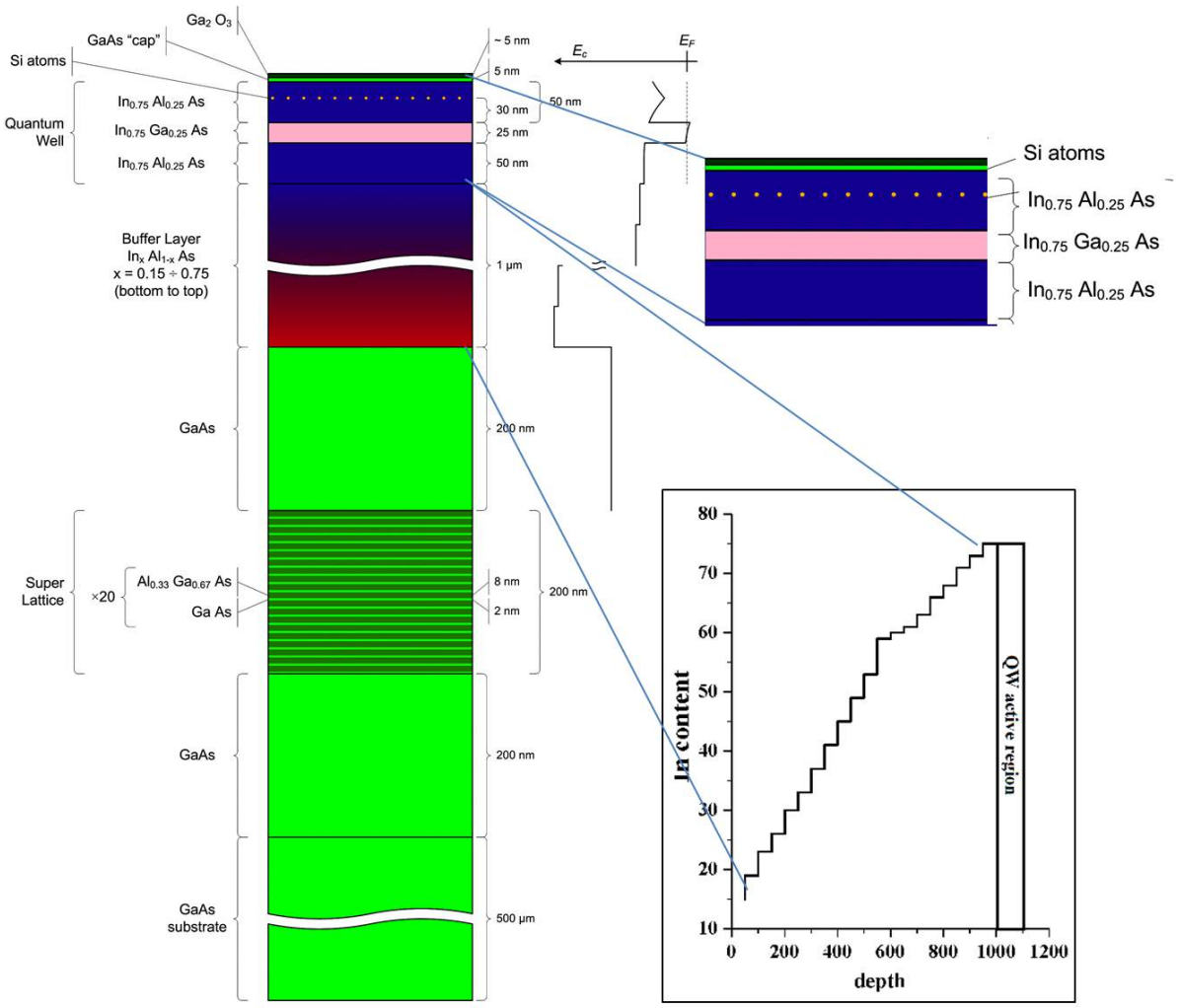

FIGURE 5.3: The growth sequence of the $In_xGa_{1-x}As/In_xAl_{1-x}As$ samples. In the first, a schematic view of the layers with the zoom of the QW. On the right down is the buffer layer composition: the vertical axis represents the distance from the top of the interfacial layer, and the horizontal axis is the indium concentration x.

as can be seen in the transmission electron microscopy (TEM) image of Fig. 5.4a) [32]. The upper layers of the BL are however virtually dislocation-free, and allow growth of an almost unstrained $In_{0.75}Ga_{0.25}As$ quantum well can be grown after the BL with same In concentration.

- *Active layer.* The substrate temperature is increased to 470^{o}C. This layer consists of a lower 50 nm thick $In_{0.75}Al_{0.25}As$ barrier, a 25 nm thick $In_{0.75}Ga_{0.25}As$ quantum well, an upper 50 nm thick $In_{0.75}Al_{0.25}As$ barrier covered by a 5nm thick GaAs cap layer (see Fig. 5.4a). The upper barrier is delta-doped by Si delta 30 nm apart from the QW with

different concentration. As can be seen in the atomic force microscopy image of Fig. 5.4b, the top surface exhibits a typical cross-hatched pattern and root mean square (RMS) values from few nm to hundreds of nm, as a memory of the underlying dislocation pattern [40].

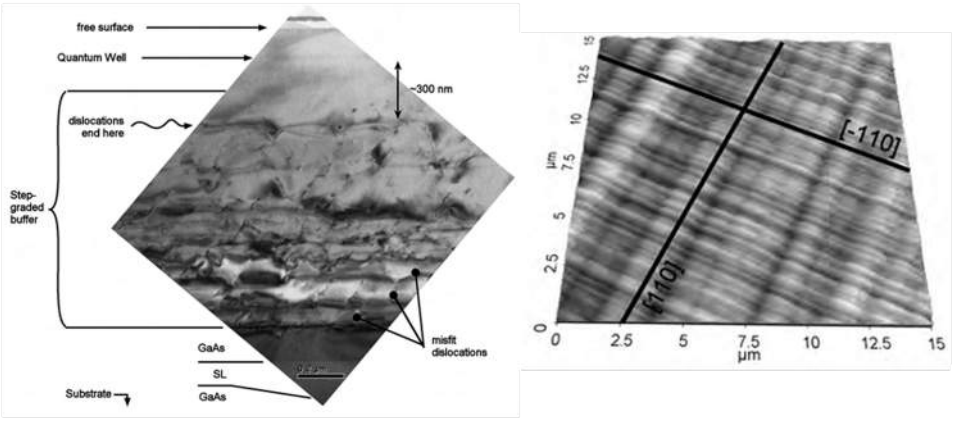

a) **b)**

FIGURE 5.4: a) TEM cross section of metamorphic step graded layer on $In_xAl_{1-x}As$ [32]; b)A representative AFM topography of one of the $In_{0.75}Ga_{0.25}As/In_{0.75}Al_{0.25}As$, showing the characteristic cross-hatch pattern of surface roughness [40]

5.1.1.1 Transport measurements

Hall measurements were performed both at low temperature (1.5K) and at room temperature (RT) to characterize the charge density n and the carrier mobility μ in the QW. A series of samples with different Si doping concentrations was grown, allowing us to control the carrier density inside the 2DEG. Figure 5.5a shows that the charge density is always higher at RT, due to the higher electron kinetic energy. In particular, it can be tuned in the range 5×10^{11} - 1×10^{12} cm^{-2} by increasing the Si doping. Note that a residual charge is present in the QW even in the absence of intentional doping, due to the existence of defects in the AlGaAs barrier that populate the QW [33]. The mobility decreases by more than an order of magnitude (10^5 to 10^4 cm^2 V^{-1}s^{-1} ranges) in going from 1.5K to RT, due to phonon scattering [59]. At both temperatures it decreases with increasing Si doping [32], evidencing that scattering with remote impurities is playing a role even at RT. The resistivity $\rho = 1/(n\mu e)$ of the 2D channel is rather insensible to the Si doping, and is in the range of 10^2 Ohms at LT and 10^3 Ohms at RT (Fig. 5.5c).

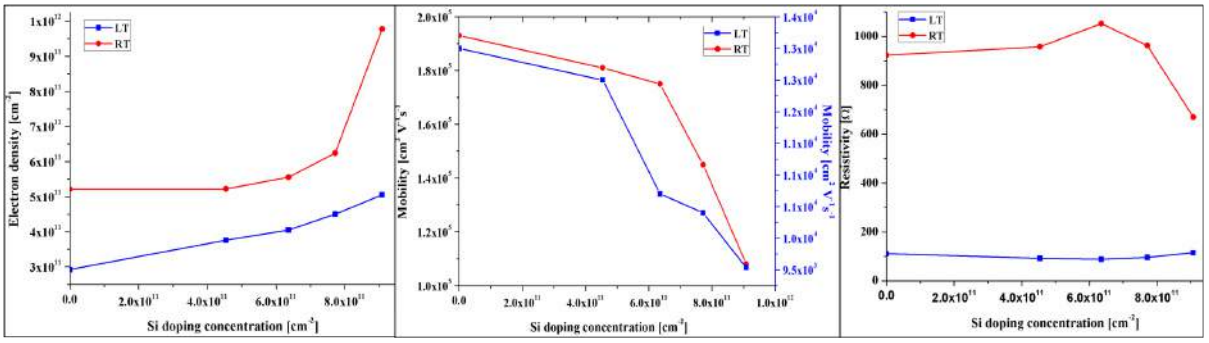

FIGURE 5.5: a) Electron density and b) Electron mobility inside the 2DEG c) Resistivity as a function of Si concetration in the delta-doping layer.

Top-to-bottom resistance across the 500μm GaAs wafer and the epilayers was found to be of the order of 100 MΩ, mostly determined by the substrate resistivity, which is order of $\times 10^7 \Omega$cm taken from the semi-insulating GaAs wafer sheet, as specified in the wafer specs sheets

5.2 Fabrication of pixelated devices

A number of QW devices have been fabricated at the CNR-IOM TASC Laboratory. We have fabricated several pixelation configurations in this work. Depending on the configuration, different metals for the readout electrode and bias electrode were developed, which will be given in the Appendix (8).

5.2.1 QW-side-pixelated device

In the first device configuration we chose to pixelate the active region containing the InGaAs QW, as the most direct method to isolate electrically photo-currents originating from different quadrants. Pixelated structures were fabricated by optical lithography and wet chemical etching into the active surface. This allows us to electrically isolate four quadrants (pixels) containing the QW under them in a square (2×2) geometry.

We have designed a pixelation mask (Fig. 5.6) with different clearances separating the quadrants, with widths ranging from 100 μm to 400 μm. Depending on the beam size used

in the measurements we selected the clearance with the most appropriate width and relation between a beam size and pixel clearance will be detailed in Section (6.2). Both positive end

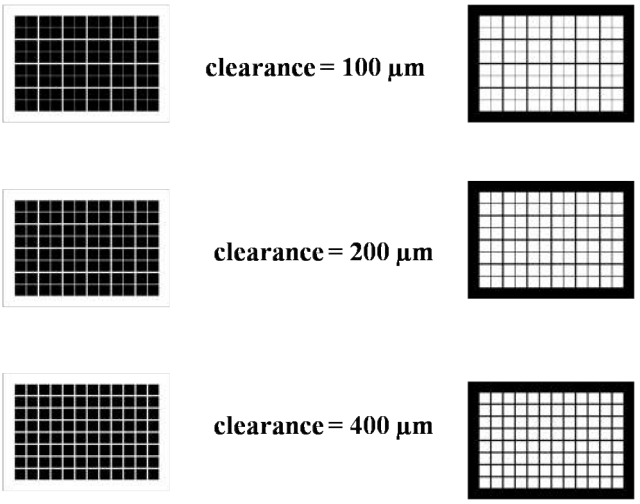

FIGURE 5.6: Positive and negative masks with different clearance width between the pixels

negative masks contain 4x6 samples in same time arrays, each samples being divided in turn in (2×2) pixels), which allows us to produce several samples with same structure at once and test with different sources without transferring the samples. The size of a single mask is 5x5 mm^2 and the clearances between masks are 400 μm wide, sharp enough to precisely cut a single samples. Before fabrication of the pixelated structure, the the wafer was cleaned by acetone with ultrasonicator and rinsed by isoproponal. S1818 positive photo-resist was span on the top of the wafer with 5000 rpm for 1min. In order to harden the resist, it was baked at 115^{o}C for 1 min, giving a thickness of about 1.5-1.8 μm.

The positive mask with 100 μm clearance between the pixels was chosen to fabricated the first configuration of pixelation on the QW side. After 20 sec of UV exposure, the resist was developed for 30-45 sec in an MF319 developer solution. The exposed area is thus removed by the developer and remaining resist protects the surface from etching. Etching is done in the wet form in a H_3PO_4:H_2O_2:H_2O solution with ratio 3:1:50. Etching rates for the different materials is given in the Table (5.1).

In this device, a 100-μm-wide and $\backsim$1.5μm deep cross-shaped clearance on the QW side of the dice was etched, deep enough to reach the substrate (Fig.5.7). The size of the clearance was measured by surface a profilemeter (Fig. 5.8), and resulted to be 100 μm - 120 μm wide and 1.5 μm to 1.8 μm deep. This allowed us to electrically isolate four quadrants

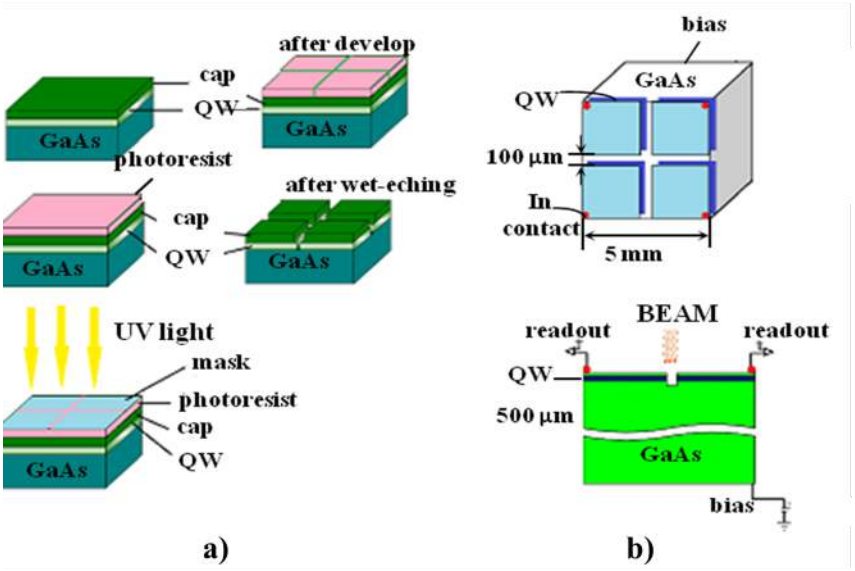

FIGURE 5.7: a) Photo-lithographic development on the sample; b) schematic view of the segmented QW device;

TABLE 5.1: Etching rate in H_3PO_4:H_2O_2:H_2O solution

Material	Etching rate [nm/min]
GaAs	100
$Al_xGa_{1-x}As$ x < 0.35	100
$In_xGa_{1-x}As$ x = 0.75	120
$In_xAl_{1-x}As$ x = 0.75	120

(pixels) containing the QW under them. In this first configuration, ohmic contacts to the readout were done by simply depositing indium drop contacts on the corner of each quadrant.

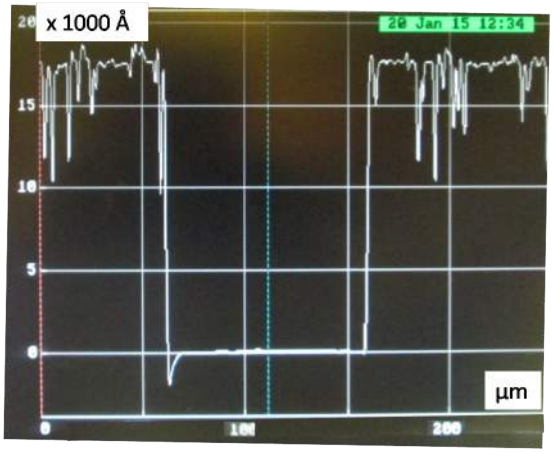

FIGURE 5.8: Surface profile of the clearance

5.2.2 Back-side-pixelated device

In order to fit our devices to commercially available readout chips, especially in future implementations of (n $\times$ m) devices with n, m $>$ 2, we have designed a second configuration where the pixelation was realized on the back side of the device instead of on the top QW. In fact, while our segmentation into 4 quadrants allows contacting the pixels to the readout chips via simple wiring, this is not technically possible if the pixels are more than 4. In this case the readout electrodes have to be bonded to the readout chips (Fig. 5.9). Therefore, it is not possible that beam hits the device from the readout side.

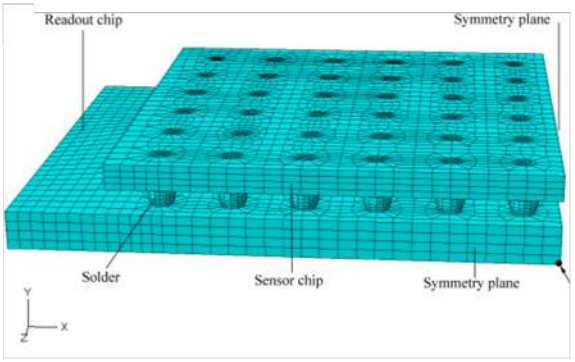

FIGURE 5.9: Schematic presentation of the readout chip

4 readout quadrants made of Au/Ge/Ni (130 nm/60 nm/30 nm) were deposited by means of metal evaporation on the back side of the dice with a 100-μm clearance, while the QW was left unsegmented. Instead of In drop contact for the readout, an uniform metallic layer was developed in order to reduce the electronic noise.

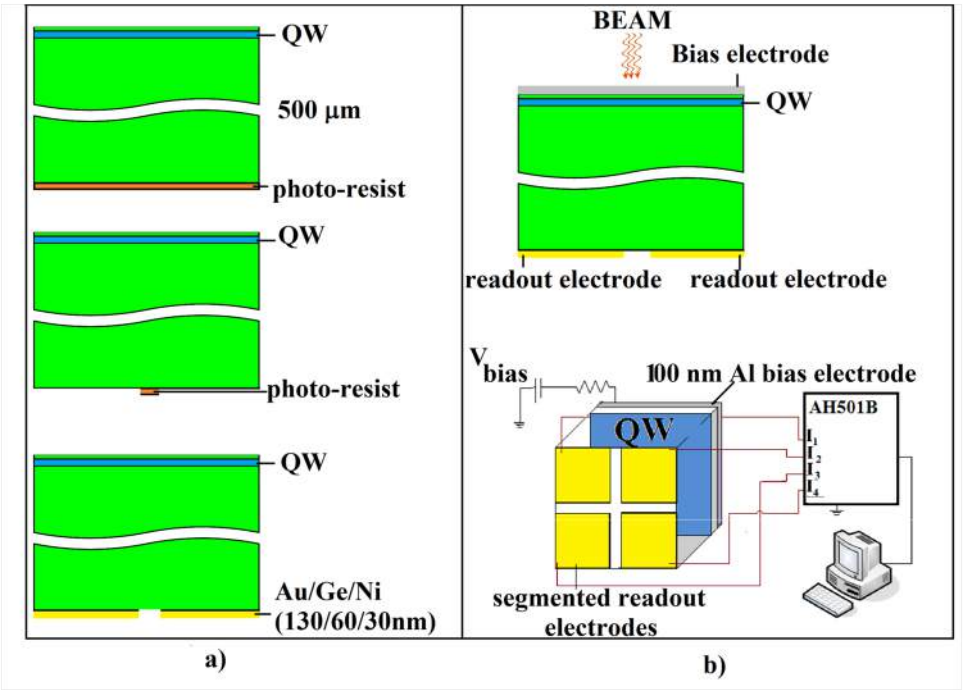

FIGURE 5.10: a) Photo-lithographic development on the sample; b)schematic view of the fabricated back-side-pixelated device;

The roughness of the back surface is an important issue to address in order to develop the pixelation geometry, when lithography involves the back side. In fact, the back surface (RMS$\sim$0.5μm) of the wafer is much rougher than the epitaxially grown surface (RMS$\sim$3 nm [32]). Therefore, the back surface of the device had to be mechanically polished in order to reduce the roughness down to 50 nm, which is acceptable for our fabrication procedures (Fig. 5.11).

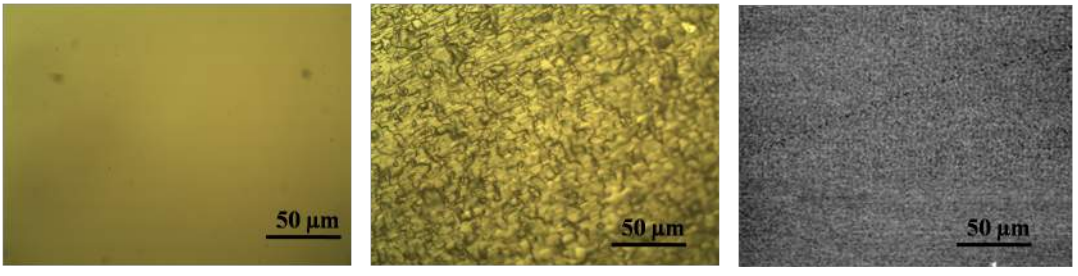

FIGURE 5.11: Surface topography of the surfaces a) epitaxial grown surface (RMS$\sim$3 nm), b) back surface of the wafer (RMS$\sim$0.5μm), c) the same after mechanical polishing (RMS$\sim$50nm)

After polishing the surface, the positive resist was deposited onto the back side of the sample. A cross-shaped resist strip 100 μm wide with thickness of 1.8 μm remains after the exposure and development of the positive resist. Metal layers were then evaporated on the surface. This was followed by immersion in warm acetone, which removes the resist strip and the metal layer above it (lift-off). After the lift-off process, 4 Au/Ge/Ni pixels with 100 μm clearance between each other are obtained on the back surface. In this configuration, chemical etching is not applied since the unsegmented active region with the QW is in the other side of the device. A single 100-nm Al electrode was deposited on the QW side of the die for biasing.

5.2.3 Double-side-pixelated device

The third configuration was developed as a combination of the first 2 segmented strategies, to obtain a double-side pixelated device (see Fig. 5.12). In order to see effect of the higher field value (-0.04$V/\mu m$) with respect to previous two devices (-0.03$V/\mu m$), the thickness of the substrate was chosen to be 350 μm in this device. The QW was segmented with the same geometry of the first configuration, and subsequently covered by a single Al bias electrode. Two lithography steps were necessary to pixelate the QW side and deposit single metal electrode above it. The active region was etched trough the mask of positive resist for the pixelation. The etched clearance is the same as the first configuration (100 μm wide, 1.5 μm deep) after the wet-etching. In the second lithography step, the clearance between the QW pixels was filled with the positive resist to isolate the 2DEG regions from each other. 100 nm of Al was deposited on the surface providing a single electrode for biasing. Four segmented readout electrodes made

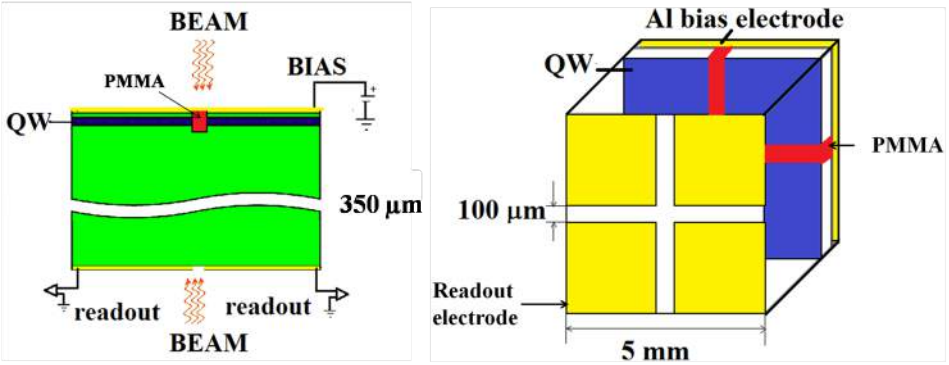

FIGURE 5.12: Double-side-pixelated device

of 100 nm Al were then deposited on the back side by metal deposition and lift-off, like in the second configuration. Aluminium was chosen for both sides due the lower absorption of

photons, with respect to the other metals (see Appendix). We have tested the performance of these double-side segmented devices with the beam hitting from either side (see Fig. 5.12, left). Having the QW side pixelated, precision for the beam monitoring is expected to be with better respect to back segmented devices due to the minimized cross talk between the pixels.

5.2.4 Back-tinned device

An offset drift of the dark current is one of the major issues encountered while testing these devices (see later in Section 6.2). Our measurements showed that this effect is mainly caused by the thick GaAs substrate. In order to reduce this effect, we developed a procedure to thin the substrate by mechanical polishing down to 40 μm. A 100-nm-thick Al layers was deposited for bias electrode.

After developing the pixelation structure on the QW side with a 200-μm-wide and 400-nm-deep clearance, the sample is mounted on the board with the QW side facing it and In ball-bonded to the readout receptacles. Au/Ge/Ni metallic layers were chosen for the readout electrode metals since the ohmic contact is realized on the QW side (see discussion in the Appendix abut the metal choice).

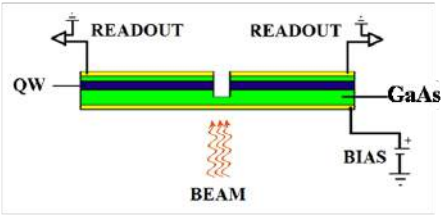

FIGURE 5.13: Schematic view of back-tinned sample

Chapter 6

Results

This section describes the main results obtained in this thesis. First of all, the working condition of the QW detector was optimized in terms of bias voltage. A low dark current with small noise was measured at -15 V bias. Section 6.1 shows the time response of the QW device to an ultra-fast laser pulse, which is a fundamental figure of merit for use as a detector in SR and FEL. We obtained time responses as small as 100 ps. Results of the tests of the QW devices in terms of position sensitivity are given by the following section 6.2. The finest precision obtained for position estimation of the photon beam was 800 nm with a 70 μm wide synchrotron beam. Finally, the last section 6.3 of this chapter will describe estimated enhanced Charge Collection Efficiency (CCE) for our QW devices, which compares very favourably to existing detectors.

Optimization of bias voltage

As a preliminary characterization, we have optimized the operating bias voltage between the top and bottom faces of the device in the dark, to find the conditions where both dark current and noise are minimized. The dark current summing from for all the 4 quadrants of the back-side-segmented device (5.2.2) was measured under a bias voltage ranging from -30 V to 30 V range in 5 V intervals at room temperature (Fig. 6.1 dots). A smaller dark current was recorded for negative biases, with respect to positive ones, saturating from about -15 V. Additionally, an increase of the current noise was observed with positive bias (Fig. 6.1, squares). The maximum and minimum values of rms noise were recorded as 2.7 nA and 0.02 nA at 30V and - 30 V bias voltages, respectively. Therefore, a bias voltage of -15 V was chosen for the measurements as

the optimal bias voltage in terms of dark currents and noise. This is a significant advantage of these devices with respect to other solid-state position-sensitive detectors which require higher voltages [41]. For example a typical bias voltage for a single crystal diamond is about -500 V and it is much higher for ion chambers [8].

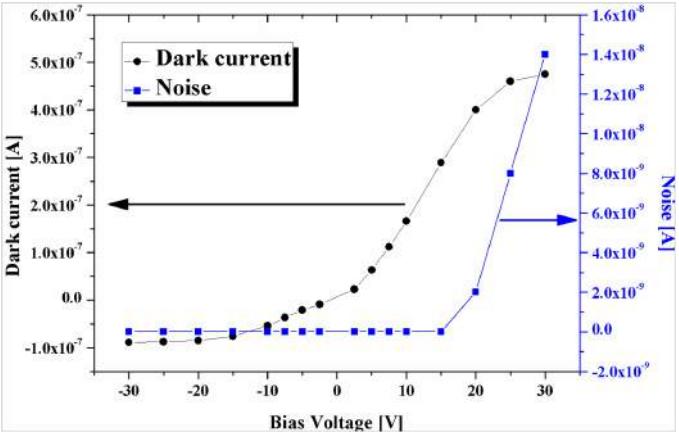

FIGURE 6.1: Dark current (dots) and current noise (squares) of the QW device in terms of bias voltage

6.1 Time response of the device to near UV laser light

Diagnostics at third generation synchrotron radiation sources needs devices with response times from the sub-ns to the ps range. Future FEL sources will require faster detectors with a response time in the fs domain. The accessibility of room temperature infrared devices based on HgCdTe alloy semiconductors already now allows obtaining sub-ns response times [60]. Recently, high frequency UV tests have evidenced that a single crystal diamond detector responds to very short laser pulses with rise times about 600 ps [21].

The high carrier mobility of the QW device at RT (around $10^4 cm^2 V^{-1} s^{-1}$) makes it possible to detect ultra-fast light pulses operating in either air or vacuum without using a cooling equipment. Therefore, these novel detectors are good candidates to sense the position and the intensity of a beam meeting the demanding time-resolution requirements posed by recent SR and FEL sources.

In our work, the performances of these detectors have been assessed by measuring their response to ultra-fast laser pulses. Experiments have been carried out through a table-top Ti-sapphire laser delivering 100-fs-wide pulses with a 400 nm wavelength (Section 4.4.1).

Experimental procedure and Device setup

Ultra-fast near UV pulsed laser sources are an efficient tool to characterize the presented QW detectors in terms of time response. We have tested two configurations (Fig. 6.2a) and (Fig. 6.2b) of the QW devices.

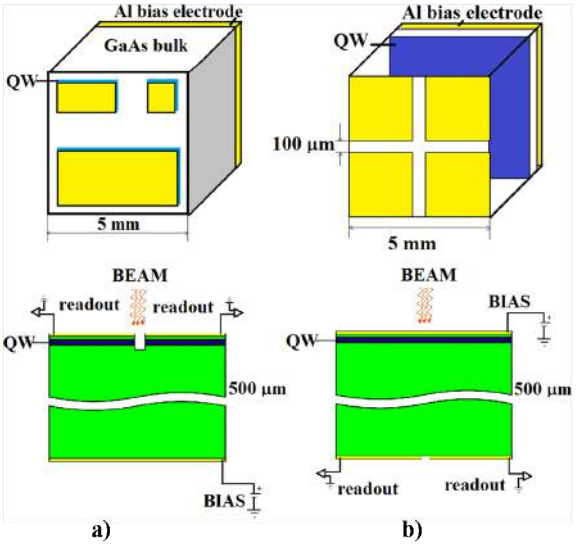

FIGURE 6.2: Tested configurations; a) segmented QW, b) Segmented readout electrodes in the back side of the device, unsegmented QW

A 100-μm-spot laser beam was focused on the surface. The power of the pulsed laser was 1140μW, while the detector was biased with –15 V. The signals from the readout pads were acquired through a 40 GS/s oscilloscope. The power of the impinging photon pulse was varied during the tests to check the dependence of photo-generated charges. The QW devices were mounted on a compact vacuum chamber (Fig. 6.3) with small coaxial cables are connected to the readout pads of the carrier board, immediately next to the sensor, in order to transmit the broad-band signals generated by the QWs on a shielded, 50 Ω impedance-matched path.

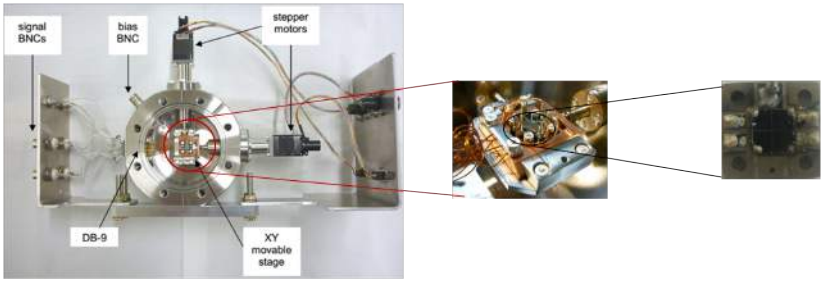

FIGURE 6.3: Compact chamber (Version No.1)

6.1.1 Results and Discussion

In order to explore the pulse response of the detector, the acquired signal originated from the UV pulsed laser was displayed through the high-frequency setup while keeping the laser light spot on the detector. Important results have been achieved in terms of sub-nano second pulse detection: the response to 100-fs-wide laser pulses has shown very short rise times of about 100 ps in both devices. These results show that the QW devices respond faster than similar beam positioning photon detectors such as diamond, where the response times were at best of the order of 600 ps [41]. As shown in Figure 6.4a, the rise time and fall time of the peak are similarly sharp for the segmented QW case. However, the peak of the back-side pixelated device has some tale structure (Fig. 6.4b), which could be caused by deep levels due to dislocations in the buffer layer or impurities from the substrate. In fact, when the laser beam is hitting from the QW side, most of the photons are absorbed in the QW region, since the penetration depth is around a few nm for 400 nm photons (see Fig. 3.6). On the other hand, in the device where the beam hits from the opposite side of the readout, electrons have to cross the whole sample thickness and scattering events through the substrate could deteriorate the tail shape.

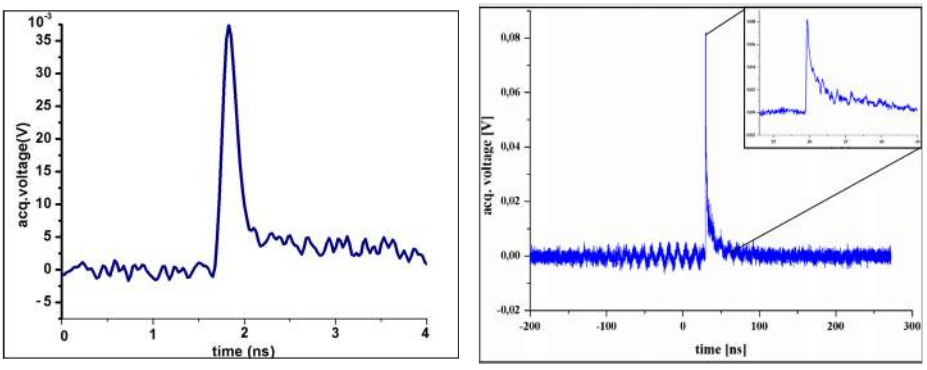

a) b)

FIGURE 6.4: Response of device to the laser pulses: a) with segmented QW structure on the surface; b) Back-side-pixelated device

6.1.2 Summary

The capabilities of the proposed QW devices were tested in terms of fastness of signal detection in response to short-pulsed near UV laser light. Thanks to the high carrier mobility of the electrons inside the QW, our detectors are capable to respond with 100 ps rise times to ultra-short near UV pulses. The fastness of our device is recorded as the fastest with respect to

other solid state photon detectors [41]. These promising performances might pave the way for applications in time-resolved experiments and diagnostics with SR and novel light sources.

6.2 Position sensitivity

We have tested the QW devices as photon beam position monitor (pBPM) at different energies (2.14 keV - 22 keV) while beam size is ranging from 70×70 m^2 to 522 m^2. In this section we will analyse the spatial sensitivity to the beam position for the first three configurations introduced in Chapter 5. Position sensitivities of QW and bulk GaAs devices were compared on the conventional crystallographic X-ray tube providing a white beam with photon energies at 22 keV with 500 μm beam size. The comparison of detectors fabricated on QW epitaxial samples and on bulk GaAs is useful to assess the role of the QW in the position monitoring capabilities of our devices. From a mesh scan of both the QW and GaAs devices with 500 μm X-ray beam, the QW detector shows enhanced photon beam position sensitivity with respect to bulk GaAs (Fig. 6.5). Responses of the all channels are more uniform and the difference between the photo-current and the dark current of the QW is much higher than in the bulk GaAs. The 4 pixels on the surface can be clearly distinguished due to the negligible cross talk between the pixels in the QW detector (Fig. 6.5a). This means that segmentation of the QW allows us to electrically isolate the pixels much better than the GaAs detector, even if the geometry of the two detectors were the same. Moreover, the total photo-current was higher in the QW detector then in GaAs, for lower electric fields (1.13 nA at a field of -0.03 V/μm, with respect to 1.06nA at -0.04 V/μm). The higher photo-current in the QW detector could be due to the fact that photo-generated electrons drifting through the sample give their kinetic energy to the carriers in the 2DEG forming inside the QW and allow them to escape from the potential to contribute to the photo-current. This mechanism could be considered as a charge amplification effect due to the high charge density in the 2DEG [61].

An offset drift of the photo currents is one of the major issues encountered while testing these devices. Figure 6.6 shows the drift value on the photo during a scan for both the QW and bulk GaAs detector. The drift value is measured 25 times higher in the bulk detector, which shows the bulk substrate could be a main reason of the drift.

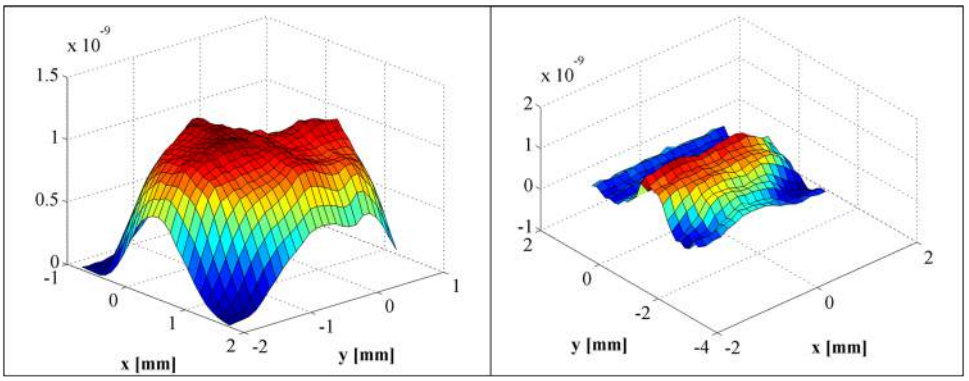

a) b)

FIGURE 6.5: Mesh scan with a conventional X-ray tube performed on: a) the QW detector b) the GaAs detector

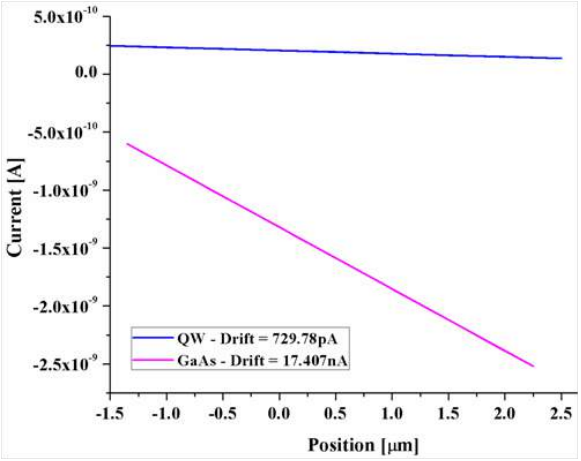

FIGURE 6.6: Drift value on the photo-current during a mesh scan: a) the QW detector b) the GaAs detector

6.2.1 Estimation of position

Beam exposure generates photo carriers inside the device, which can be collected at the read-out electrodes by applying a bias voltage, giving rise to measurable currents. The individual currents obtained from each electrode allow to monitor the position of the beam (Fig. 6.7).

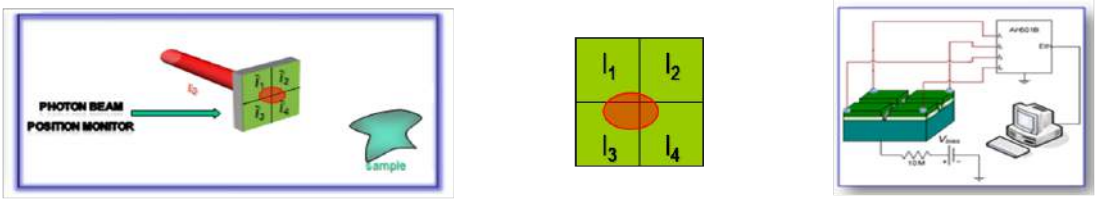

FIGURE 6.7: Position estimation principle

Position encoding can be extracted from the photo-currents from each pixels. The *difference-over-sum* (DOS) technique [8] is the preferred means for deriving the position of the center of gravity from the current signals of the individual electrodes. If I_i is the current from a single channel (Fig. 6.7) then the coordinates of the beam can be calculated as:

$$x = \triangle x \frac{(I_1 + I_3) - (I_2 + I_4)}{\sum_{i=1}^{4} I_i} \qquad y = \triangle y \frac{(I_1 + I_2) - (I_3 + I_4)}{\sum_{i=1}^{4} I_i} \tag{6.1}$$

here $\triangle x$ and $\triangle y$ are normalization factors, which can be extracted from a fitting of DOS in linear region ($x = a \cdot x + b$ and $y = c \cdot y + d$). In case of a line scan where only two channel will be involved, the currents can be defined as I_R and I_L. Then Eq. 6.1 will reduce to

$$x = \triangle x \frac{I_R - I_L}{I_R + I_L} \tag{6.2}$$

Final precisions for the position estimation can be calculated from the measured current I with SNR (signal to noise ratio):

$$\delta_x = \frac{\triangle x}{2\sqrt{2}} \frac{\sigma_I}{I}; \qquad \delta_y = \frac{\triangle y}{2\sqrt{2}} \frac{\sigma_I}{I}; \quad \text{here} \qquad \triangle x = \frac{1}{a}; \triangle y = \frac{1}{c} \quad \sigma_I = \frac{1}{SNR}; \tag{6.3}$$

The relative change between the individual signals produces a profile forming the cumulative curve. Evaluation of the precision in the coding of the position is calculated by the estimation error with two methods: in one case, we calculated the standard deviation of x or y in the central position by propagating the standard deviation of the current acquired at that point; in the other, we estimated directly the the deviation between the fitting profile that calculated by (Eq. 6.1) or (Eq. 6.2) from the experimental data. We defined the precision of estimation (PE) by choosing the larger of the two errors. These values can be considered valid in the region where the currents change linearly across the aperture comparable to the FWHM of the spot.

6.2.2 Position sensitivity of QW-side-segmented device

A conventional and synchrotron X-ray sources have been successfully used to test the QW detectors with a wide range of high energy photons, by taking advantage of the motorised stage to perform either linear or mesh scans of the sensors. The QW-side-pixelated device (5.2.1) is

tested with the XRF beamline and a conventional X-ray tube, in order to check the response of the device in terms of position sensitivity and homogeneity.

In the first experiment was performed on the XRF beamline, whose beam spectral distribution is bell-shaped as a function of the logarithm of the photon energy and the maximum spectral flux density is found at a photon energy of 7 keV with 4×10^7 ph/s; in addition, a double-slit collimator has been used to obtain a needle-beam with a 70-μm FWHM.

The second experiment, a conventional crystallographic X-ray tube provides a white beam with photon energies ranging from 6 keV to 50 keV with an intensity peak at 22 keV. The spot size has been reduced by a pinhole and a double-slit collimator down to 140 μm (FWHM) at the interaction point. Linear scans of a sensor with 100-μm clearances in front of a stationary X-ray beam generated by the X-ray tube were performed sweeping over adjacent pixels. The QW detectors have been mounted on an XY movable stage which is housed in a compact vacuum chamber comprising stepper motors, such that mesh scans of the sensors can be performed (4.4.4).

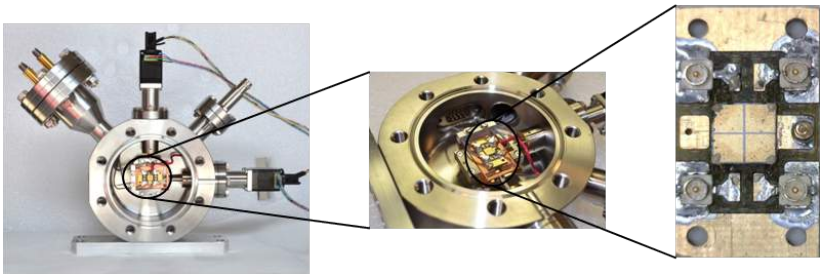

FIGURE 6.8: UHV chamber with movable stage (Version no.2). The movable stage was improved with respect to previous chamber (6.3) in terms of movement precision and the board for the sample has a drilled hole in order to provide the beam hitting from both side

In the first measurement, the position of the needle-beam with 70 μm FWHM was estimated by the first device (segmented QW 5.2.1) with energy peaked at 7 keV. Figure 6.9 shows the currents from the four individual quadrants during the line scan when the beam crosses the clearance between quadrants 2 and 4.

When the beam hits only quadrant 2, only the current from channel 2 is present (I2), with no contributions from the other three channels. Then, while the beam is shifting from one pixel to the next one, a sharp switch in current takes place from channel 2 to channel 4. Channel 3, which like channel 1 was not hit by the beam during the scan, was noisier than the other channels; this is probably an electric noise caused by a bad contact or connection.

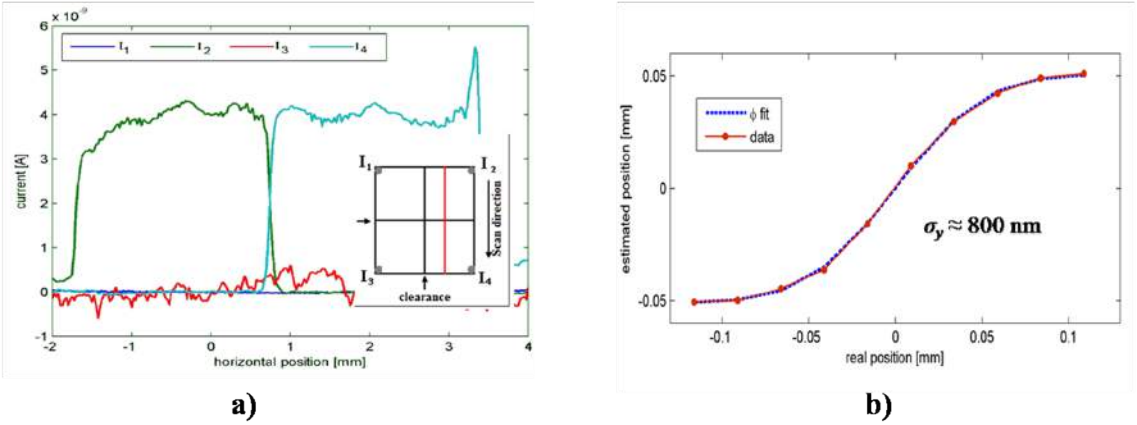

FIGURE 6.9: a) Separate currents measured from each electrode (inset shows the scan direction on the device surface), b) position estimation along y-direction in terms of real position, with precision 800 nm for the needle beam

The beam was estimated in terms of real position by using the DOS technique [8] and fitting a cumulative curve (Fig. 6.9b). The deviations from the fitted curve indicate that these devices can extract the beam position with a spatial precision of 800 nm for a photon beam with the described parameters.

Then the QW samples have been scanned with the beam emitted by the X-ray tube (photon energy is 22 keV with a photon flux order of 10^4). The results of horizontal and vertical position estimations in terms of real displacements are plotted in Figure 6.10a and 6.10b respectively; the deviations from the theoretical surfaces indicate that these devices can extract the beam position with a spatial precision of 1.5 μm. This lower resolution is strongly effected by the lower photon flux with respect to the previous measurement with SR source. The level of the photo-current is proportional to the photon flux, therefore lower current is one the reason of lower precision (6.3).

6.2.3 Position sensitivity of back-side-segmented device

Results for three experiments performed with the back-side-segmented detectors (5.2.2) at the XRF beamline, Elettra, Italy, are reported in this section. The precision of the beam-position estimation was evaluated at three different photon energies in three experiments performed with monochromatic beams at photon energies of 2.14 keV, 5 keV and 10keV. A photon flux of 10^8ph/s was roughly estimated by an ion chamber for the two higher energies with a spot size of 200 μm. Since photon absorption of air increases below 4 keV, the spot size of the beam

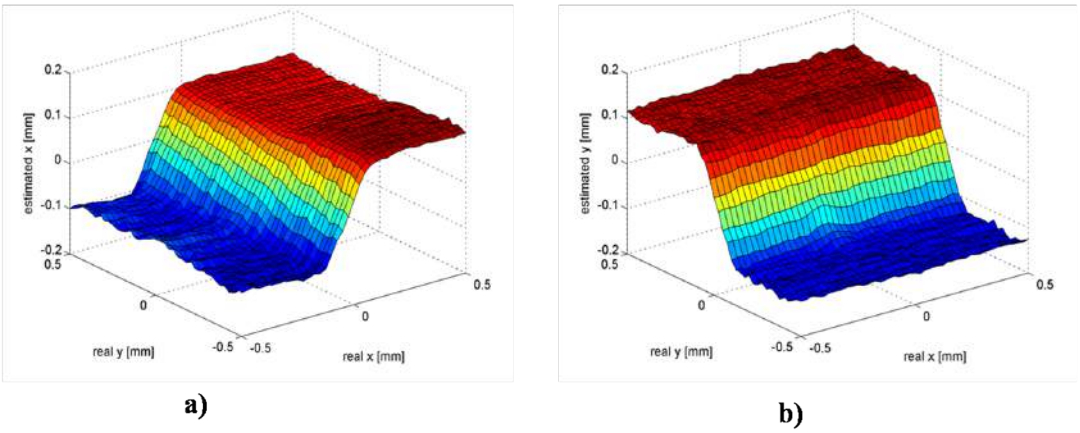

FIGURE 6.10: 2D maps of the position estimation along a) horizontal direction and b) vertical direction

at 2.14 keV was set to 500 μm, in order to reach a comparable value of the impinging flux (3×10^8ph/s). Additionally, the position monitoring was also tested with UV laser light; single ultra-short laser pulses with a spot of 100 μm were used to perform linear scans. The setup for the line scans with ultra fast laser beams is the same as section 6.1.

In order to determine the response of all channels as the X-ray beam moves across the device, scans of photo-current acquired along a square-shaped path (shown in the inset of Fig. 6.11c) were recorded. As shown in Figure 6.11, all channels were homogeneously responding to the beam exposure during the scan, at all utilized energies.

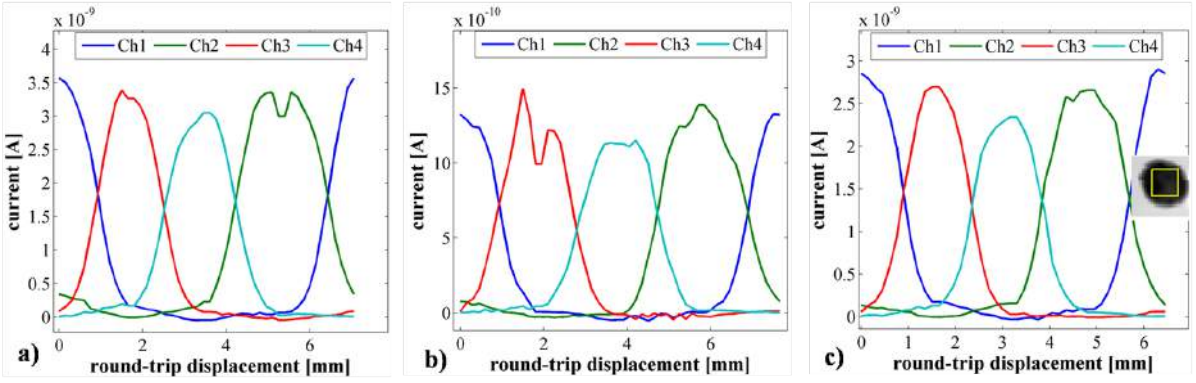

FIGURE 6.11: Current line scans along a square-shaped path around the surface of the QW device; a) at 2.14 keV, b) at 5 keV and c) at 10 keV.

While the beam is shifting from one quadrant to the next one, a sharp switch in currents between two neighbour quadrants is shown in the reported result. The individual currents obtained from each readout electrode prove that the QW detector allows to effectively monitor

the beam position even the QW is not segmented. The beam position was estimated by using the DOS technique for all energies and then plotted in terms of the real position, as determined by the XY stepper (Fig. 6.12), top panels. The estimate is represented in the 2D plot of Figure 6.12, lower panals, by the dots, relative to each of the scan lines. The deviation of this curve from the fitting cumulative function (continuous line) suggests a precision of 10 μm for the position monitoring of a 500-μm-wide monochromatic beam at 2.14 keV. The precisions of the position estimation degraded to 12 μm at 5 keV and 19 μm at 10 keV. The much poorer spatial resolution with respect to segmented QW devices (see previous section 6.2.2) could be ascribed to a cross talk between the pixels in the unsegmented case or to lateral carrier diffusion through the substrate thickness. Furthermore, we observe a loss of resolution as the photon energy increases. Since the penetration depth increases from 0.48 μm to 36 μm with the photon energy of 2 keV and 10 keV (see Section 3.2), with the beam eventually reaching the deeper layers of the BL where dislocations are present, we speculate that such dislocations play the role of traps for the photo-generated carriers which reduce the signal level and thus the resolution.

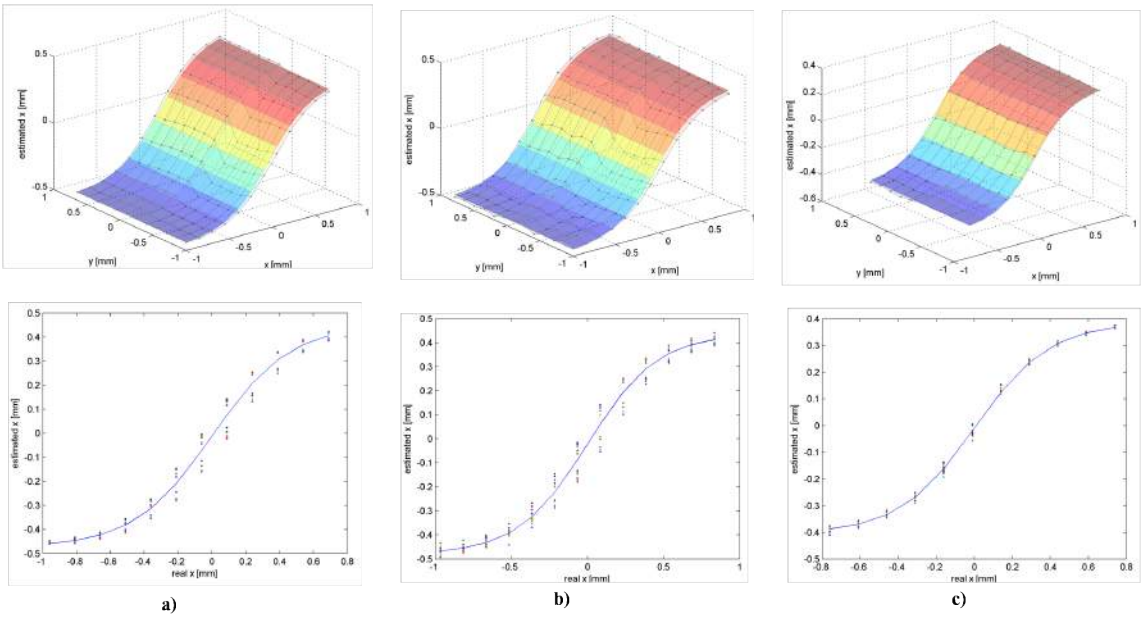

FIGURE 6.12: Estimated position from the total currents from Fig. 6.11 in terms of real beam position: 2D vertical position estimation (top) and 1D vertical position estimation (bottom) a) at 2.14 keV, b) at 5 keV and c) at 10 keV.

Finally, with the back-side-pixelated device the position monitoring of each ultrashort laser pulse was tested by linear scans across the 100 μm clearance between the quadrants. As shown in Figure 6.13a, when the beam hits one quadrant only, no current contribution from other channels is present. It is evident also in this case how the two currents from each channel

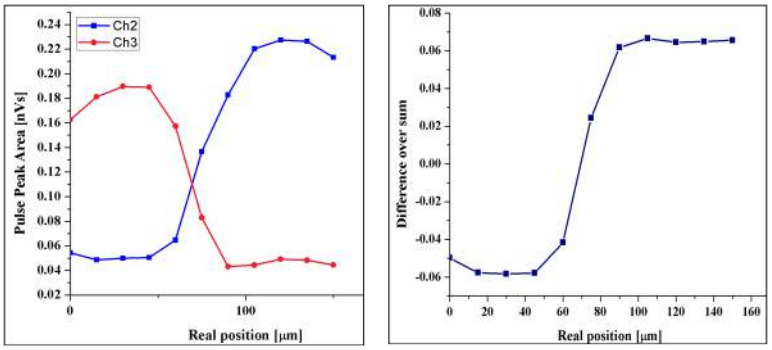

FIGURE 6.13: a) Current switch from two channels during linear scan and b) difference over sum

switch while the beam crosses the clearance. Furthermore, DOS of the beam position results in a cumulative curve with a central linear range of about 30 μm (Fig.6.13b). This proves the capability of the detector for beam position monitoring even with an ultra fast pulsed near UV laser beam. However, the number of steps in the transition region was not sufficient for a detailed estimation of the precision of the beam-position encoding.

6.2.4 Position sensitivity of double-side-segmented device

The double-side-segmented devices (5.2.3) were tested with 10 keV, 11 keV, 14 keV and 20 keV photon energies at the SYRMEP beamline. The beam size was fixed at $90\times90\mu m^2$ for all utilized energies. Two types of experiments were performed to choose suitable side where the photon beam hits. In the first measurement at photon energies of 10 keV, 14 keV and 20 keV, the beam hitting side was chosen as the QW side through a hole of the board. Lines scans between two pixels either in the horizontal or the vertical direction performed here. In the second, the device was flipped, therefore the photon beam was shooting from the readout electrode side (back side) at 11 keV and 20 keV.

The recorded current switch in the clearance is shown in Figure 6.14a. A charging up of the insulating positive resist which is used to fill up the clearances (see 5.2.3) is strongly affecting in the currents and is manifesting itself as a hump near the edge of the clearance. The best precision (12μm) was recorded at 20 keV when the beam is hitting from the QW side (6.14b). Thus, the estimation precision is in the same range as the back-side-segmented

device (see section 6.2.3), meaning that our procedure of segmenting the QW did not bring the expected improvements.

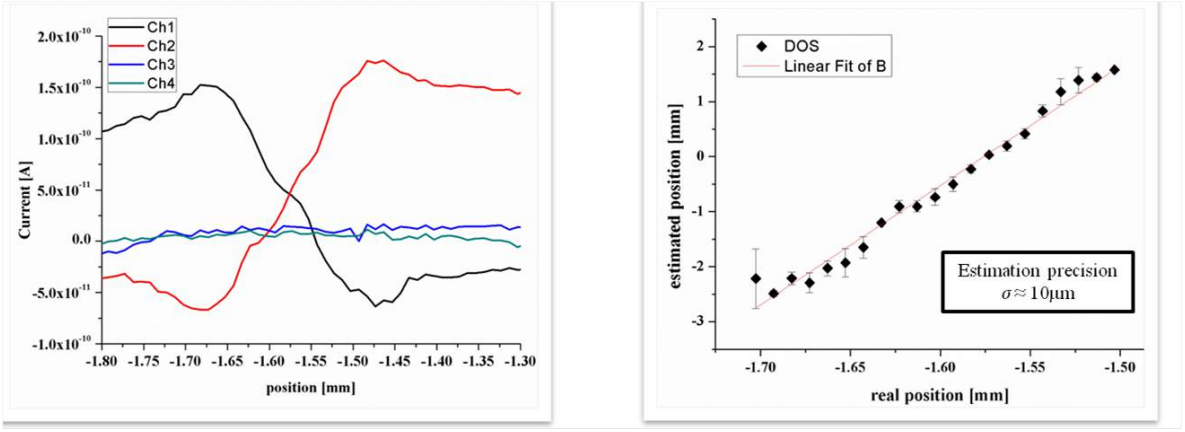

FIGURE 6.14: A linear scan on double-side pixelted device; a) Current switch from two channels during linear scan and b) DOS with linear region fitting

The reason of the poor spatial resolution of this device could be ascribed to the presence of the insulating positive resist layer in the clearance between the pixels, which could be considerably charged up due to photon absorption and increase the noise in the current at the edge of the clearance.

6.2.5 Position sensitivity of back-thinned device

Preliminary tests on the back-thinned devices (5.2.4) were performed at the MCX beamline, Elettra. In order to assess the spatial resolution of the device the beam was set as a blade beam ($100\times600\mu$m) at photon energy of 10 keV. The estimated photon flux is of the order of 10^9 ph/s. The dark current of the device versus the bias voltage is shown in Figure 6.15a. Since the thickness is much smaller than the previous devices (40 μm vs 350 - 500 μm), the bias voltage was chosen as only -4 V. A major result is that the drift on photo current was eliminated on this measurements. Equally important, the beam position could be estimated with a precision of 1μm, even though the beam was hitting from the back side. This means that with this method we were able to reach a precision comparable to our best result (obtained on the QW-side pixelated device), but in a configuration that is compatible to be fit to commercially available readout chips in multi-pixel arrays.

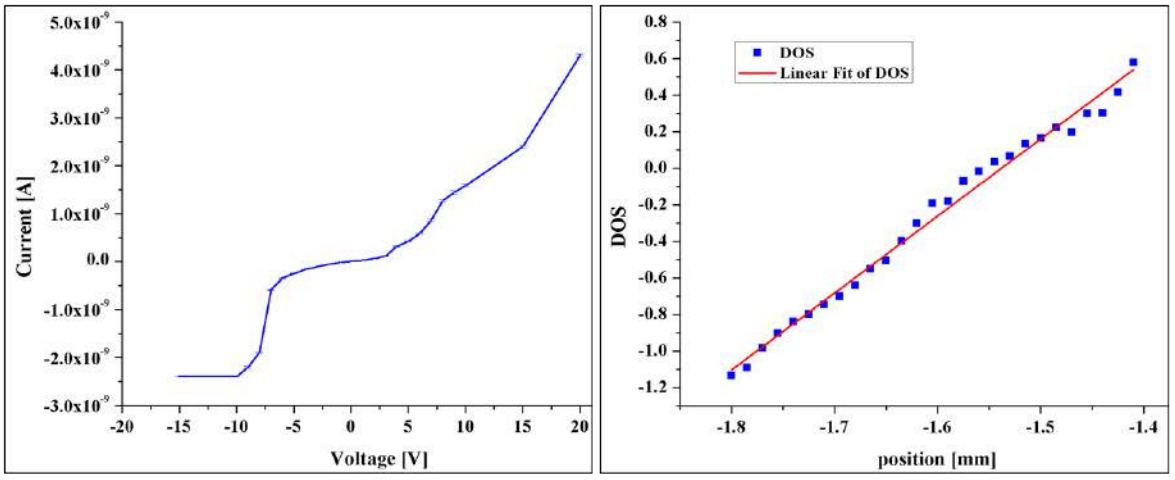

FIGURE 6.15: a) I-V curve of the back-thinned device on the dark current; b) Linear fitting by the DOS

6.2.6 Cross talk between the pixels

In this section we analyse some important phenomena taking place in our estimation of position, namely the charge spread in the material and related crosstalk between pixels, as well as their sensitivity. The cross talk between pixels is important for pixelated devices as it affects the resolution of the scans. The main measured and simulated results are reported below. Linear scans of a sensor possessing 100-μm clearances in front of a need beam with size of 90×90 μm^2 by SR were performed sweeping over adjacent pixels. For this measurement the photo-currents generated by the involved couple of pixels have been acquired step by step; the recorded values are shown in the graph of Figure 6.16a together with the total current. We defined a charge collection function (CCF) per pixel, which can show the crosstalk between pixels. Furthermore, we have simulated the profile of the DOS depending on the spot size with a given clearance between the readout pads. Three parameters have been taken into account for this simulation. The first one is the profile of the CCF, which can be extracted from the currents from individual pads (Fig. 6.16a), and fitted as an arctan function of the position in Figure 6.16b. The second one is the photon beam profile (PBP), which is chosen as a Gaussian distribution [62] for the simulation. When beam is absorbed inside the detector, it generates a cloud of charges. The third parameter is distribution of the charge cloud, which depends on the intrinsic properties of the device and will called point spread function (PSF); we assume also for this a Gaussian profile [63]. The size of the simulated beam in the PBP was varied according to the real spot

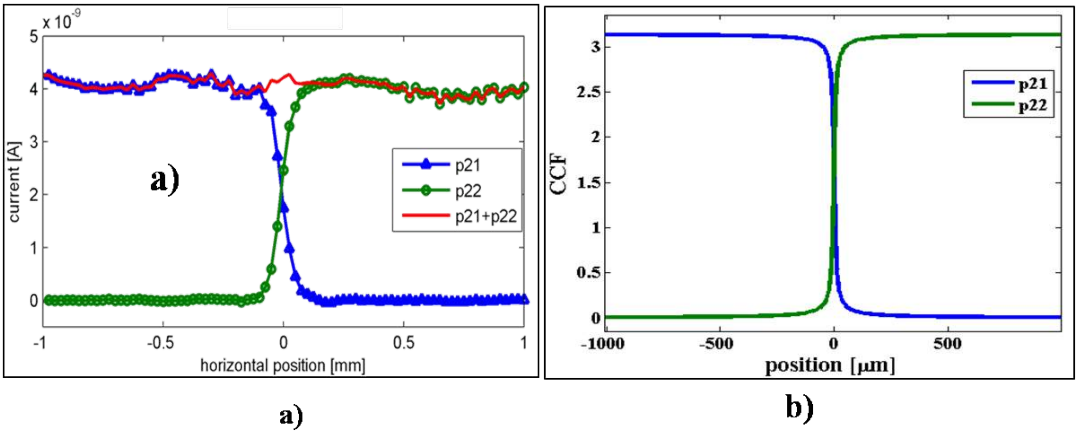

FIGURE 6.16: a) linear current scans of QW sensors with through a 100 μm clearance on the QW side with a 90×90 μm^2 X-ray beam, b) extracted arctan function from the total current

sizes used in the experiments (70 μm, 140 μm, 200 μm and 500 μm), thus the shape of the PBP was kept constant in each fit according to it. The PSF is an intrinsic parameter of our material, thus was the fixed to the same shape in all the fits. In this way, our fits are able to separate the effect of the CCF (and thus of the cross talk between pixels) from the spot and materials parameters. The simulated function resulting from the convolution of CCF, PBP and PSF was fitted to the respective measured data by comparing the simulated and the measured DOS.

Figure 6.17) shows the results of the fit for four different data sets. Panel a) is relative to a QW-segmented device measured on the X-ray tube with a 140μm beam size; panel b) to the same device at the XRF beamline with a 70μm beam size; panel c) to the back-segmented device at the XRF beamline with a 500μm spot size; finally panel d) to the same device at the XRF beamline with e 200μm spot size.

This has allowed the slope parameter of the CCF to be extracted for all the tested configurations, as shown in Figure 6.18. The slope of the CCF function is much higher (30 times) when the readout electrode is developed in the QW side than in the back side. The cross talk between pixels on the QW-segmented device is therefore much smaller than the back-side-segmented device, where the readout is realized on the bulk GaAs. These simulations show that the cross talk between pixels is actually responsible for the different resolutions obtained, independently of the experimental conditions, pointing out the importance of the geometry of the fabricated devices.

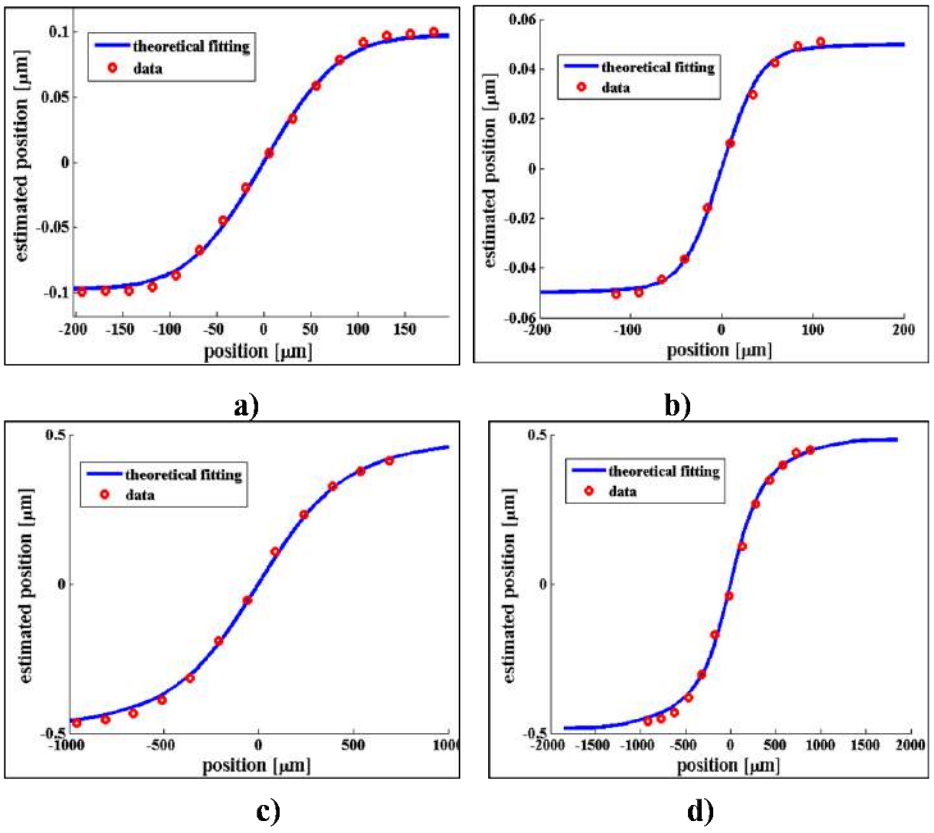

FIGURE 6.17: DOS fitting for the data a) the QW-segmented device at X-ray tube (beam size-140μm), b) the QW-segmented device at XRF (beam size-70μm), c) the back-side-segmented device at XRF (beam size-500μm), d) the back-side-segmented device at XRF (beam size-200μm)

6.2.7 Summary

The mesh-scans of the QW-side-segmented devices with X-ray SR demonstrate that a precision of 800 nm in the position estimation can be achieved. Furthermore, mesh-scans of these devices with a conventional X-ray tube gave a precision of 1.5 μm in the position estimation, with due to the lower photon flux.

On the device where the segmentation was applied to the back surface of the sample, the finest estimation precision recorded was 10 μm for a spot size of 500 μm with 2.14 keV photon energy. The precision in position estimation was about 12 μm in the case of a 200 μm-wide beam at an energy of 5 keV. The position of the 10 keV beam with 200 μm spot size was estimated with a much lower precision of 19 μm, probably because the incident photon penetrates deeper into the dislocated InAlAs buffer layers.

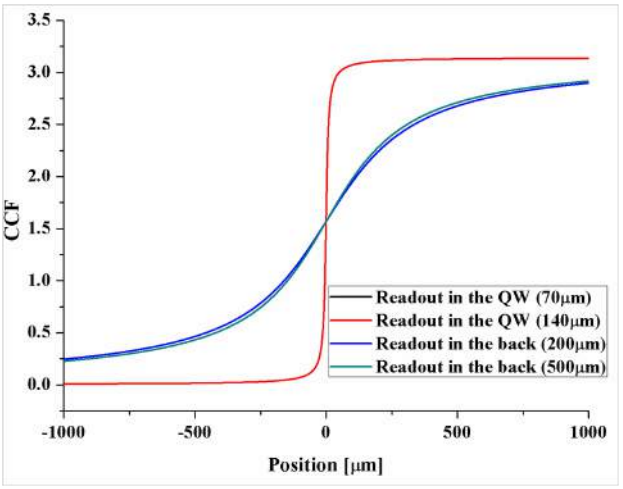

FIGURE 6.18: CCF function in terms of different beam size on both the QW and the back-segmented devices (the clearance is 100 μm)

The double-side-segmented device was tested with the needle beam at the SYRMEP beamline with several energies. The estimation precision was in same range of back-side pixelated devices, probably caused by the presence of charging PMMA between the pixels.

A precision similar to the QW-side pixelated device (1um), but with the beam hitting from the back, can be reached by thinning down the sample to about 40 μm. This is a fundamental achievement since it allowed us to obtain our record precision on a device that can be fitted on commercially readout chips in possible future multi-pixel arrays configurations. By summarizing this section, the QW photon detectors having 4 pixels on the surface where the QW is segmented has enough precision to monitor the position even for a needle beam. The back-thinned device shows a significant improvement on spatial resolution, when beam was hitting from the back side. The cross talk between the pixels is minimized when the QW is segmented.

TABLE 6.1: CCE for three energies with energies with bias voltage as -15 V

Device configuration	Photon energy $[keV]$	Photon flux $[ph/s]$	Beam diameter $[\mu m]$	Readout side	Beam hitting side	Estimation Precision $[\mu m]$
QW-side segmented	22	$\sim 10^4$	140	QW	QW	1.5
	7	$\sim 10^8$	70	QW	QW	0.8
Back-side segmented	2.14	$\sim 10^8$	500	Back	QW	10
	5.0	$\sim 10^8$	200	Back	QW	12
	10.0	$\sim 10^8$	200	Back	QW	19
Double-side segmented	10.0	$\sim 10^8$	90	Back	QW	18
	14.0	$\sim 10^8$	90	Back	QW	19
	20.0	$\sim 10^8$	90	Back	QW	12
	11.0	$\sim 10^8$	90	Back	Back	130
	20.0	$\sim 10^8$	90	Back	Back	35
Back-thinned	10.0	$\sim 10^9$	100	QW	Back	1.0

6.3 Charge collection efficiency

The high density and mobility of carriers in the 2DEG forming inside the QW allow the development of efficient photon detectors. CCE for photo-generated carriers was estimated by comparing the acquired photo-currents with the ones expected from the incident photon flux (considering pair-generation energy (ϵ) of 4.2 eV [37]). The QW devices were tested in the two SR light sources XRF beamline (6.3.1) and SYRMEP beamline (6.3.2) with different energies while changing bias voltages.

6.3.1 X-ray Fluorescence beamline

Characterization of the first back-side-segmented-device (Fig. 6.19) in terms of CCE was performed at XRF with same conditions as in section 6.2.3. The CCE was estimated with three different photon energies at the XRF beamline and the same bias voltage of -15 V as shown in Figure 6.20.

The CCE was 27% at 2.14 keV, 20% at 5 keV, and dropped to only 10% at 10 keV. This could be due to the closeness of the highest excitation energy to the Ga K absorption edge (around 10.3 keV [64]), causing a decrease of the number of photo-generated carriers.

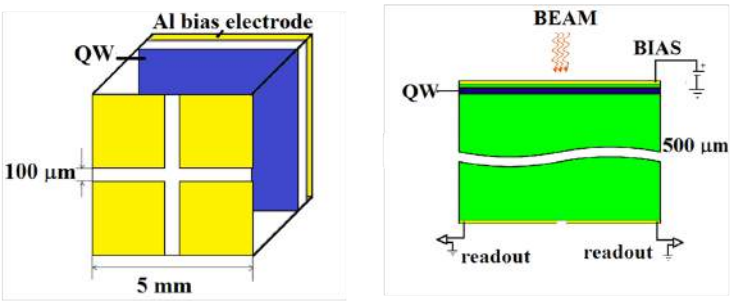

FIGURE 6.19: Tested device configuration in XRF beamline

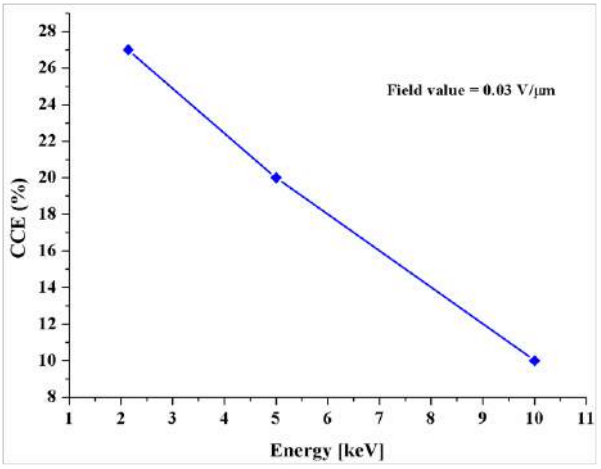

FIGURE 6.20: CCE in terms of the energies of the photon under bias voltage of -15 V

6.3.2 SYRMEP beamline

The same device (5.2.2), formed on a substrate with 500 μm thickness was tested at the SYRMEP beamline with 2 different energies of 17 keV and 22 keV to estimate CCE in terms of bias voltages (Fig. 6.21a). Additionally, measurements of CCE for photo-generated carriers for a double-side-segmented-device (5.2.3) grown on a thinner, 350um-thick wafer, were performed at the same beamline, with the photon energies of 15 keV and 20 keV (Fig. 6.21b).

The monochromatic, laminar-section X-ray beam was shaped to a spot of 522×522 μm^2. The total fluxes were estimated to be 1.55×10^8ph/s for 17 keV and 5.19×10^7 for 22 keV by the ion chamber currently used for beam diagnostic at SYRMEP. In the experiment on the double-side-segmented-device, the total flux was measured as 2.54×10^8ph/s for 15 keV and 1.64×10^8ph/s for 20 keV.

Figure 6.22a shows the CCE of the back-segmented device for the two energies, in terms of the bias voltage, in the range 0 to -60V. The results show that the CCE in our detector

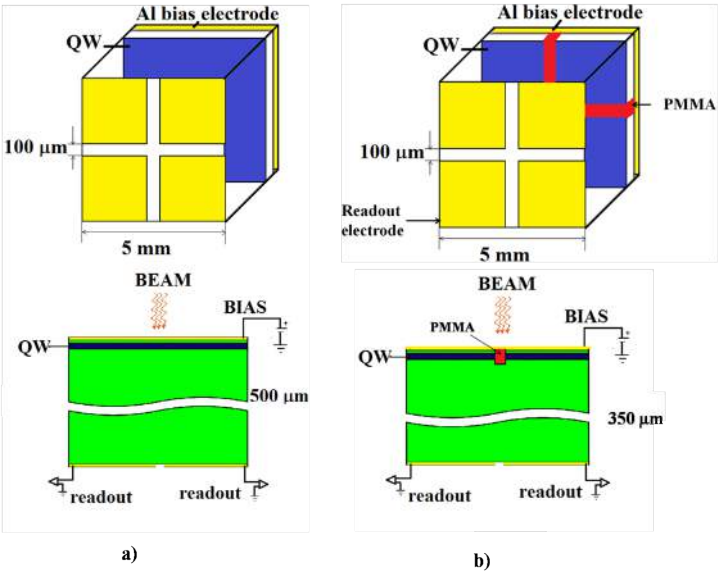

FIGURE 6.21: Setup of the CCE measurements at the SYRMEP beamline. a): back segmented device, b): double-segmented device

reach a value of about 55% at a bias of -40 V. This value is higher than the ones reported in the literature within the considered field range. For example, a 50% of CCE for 200 μm-thick GaAs detector was reported at - 140 V bias voltage [65] tested with an X-ray source. Similar CCE was recorded at 10 times higher field value on GaAs detector with a photon energy of 60 keV [66].

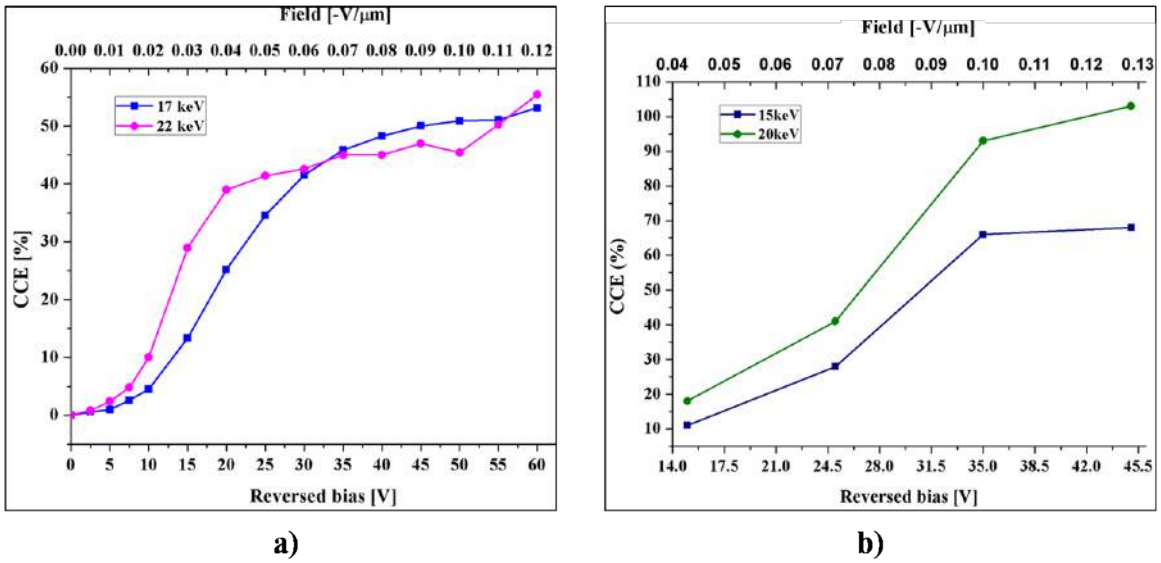

FIGURE 6.22: CCE in terms of field value at photon energies: a) 17 keV and 22 keV, b) 15 keV and 20 keV

Since the second device is thinner than the first one (350μm vs 500 μm), a higher CCE was expected for same bias voltage range. The drifting path for the photo-generated electrons is smaller than previous sample. In fact, an enhanced CCE was measured even at lower fields with respect to the previous measurements (Fig. 6.22b), with values reaching 100%. This result could be caused by the charge-amplification effect (see Section 3.2) taking place inside the QW when the drifting carriers photo-generated close to the QW transfer part of their kinetic energy to the electrons of the 2DEG, allowing them to contribute to the total current, with the mechanism outlined in Section 3.2.

Summarizing, the tests with different SR sources and energies ranging from 2.14 keV to 22 keV show how these devices exhibit high CCEs even with low bias voltage, which can be imputed to the charge-multiplication effect of the 2DEG inside the QW. The CCE is mainly depends on the incident photon energy. Most importantly, our results show that the CCE of our QW devices compare very favourably to those of existing detectors. In fact, they reach values close to 100% at bias voltages lower than 50 V, to be compared with the 140 V needed for bulk GaAs to reach only 50% [65], and single crystal diamond, which shows CCE 70% for 10 times higher electric field values [67].

Chapter 7

Conclusions

The research presented in this thesis was mainly focused on the development of the diagnostic tools for beamline applications involving photon detection. The development of the QW as pBPM has achieved an innovative technology for photon detectors of the third and fourth generation of light sources in terms of performance and compatibility. Our detectors were based on metamorphic $In_{0.75}Ga_{0.25}As/In_{0.75}Al_{0.25}As$ QWs grown on GaAs substrates and containing a high mobility two dimensional electron gas. Compared to existing, state-of-the-art detectors based on single-crystal diamond, our materials. The QW detector costs much less with better availability and repeatability with respect to single-crystal diamond detector.

We have realized photon detectors based on our epitaxial materials containing four readout pixels, defined in different geometries and placed differently with respect to the side containing the QW, the readout electronics and the photon beam. These different geometries were characterized in terms of time response, position sensitivity and charge collection efficiency.

The QW photon detector response to the X-ray beam has shown a better spatial resolution with respect to a bulk GaAs device with the same pixelation geometry. Photo-currents with low noise were recorded for low negative bias voltages, with respect to other beam monitoring photon detectors such as diamond-based pBPMs [19] and ion chambers [7]. As shown by a number of experiments with synchrotron and conventional light sources, detectors based on InGaAs/InAlAs QW in the segmented configurations can be utilized as pBPMs in synchrotron

beamlines. In particular, an 800 nm precision has been obtained for the position monitoring of a needle beam by a device where the QW region was segmented [68].

These detectors have shown time response of 100-ps to ultra-fast laser pulses, which is due to their high carrier mobility even at room temperature. Such time response is even faster than the ones obtained through state-of-the-art technologies like diamond, thereby making the QW detectors attractive in many time-resolved applications [41].

The tests with SR sources with several different energies show how these devices exhibit high charge collection efficiencies, which can be imputed to the charge-multiplication effect of the 2DEG inside the QW. The results obtained in with our QW photon detectors are hardly approachable by other technologies based on bulk GaAs or single-crystal diamond [65, 67].

The test with a QW device where the substrate was ack thinned down to 40 μm showed how the offset drift was completely eliminated and the spatial resolution (1μm) of the beam monitoring reached our record values even when the beam was hitting from the back side of the detector. Therefore, the back-thinned configuration can be a key improvement for the future production of pixeleted QW detectors, as it is compatible with commercially readout chips in possible future multi-pixel arrays configurations. .

Chapter 8

Appendix: Fabrication of ohmic contacts

In the first device (Section 5.2.1), electrical contacts were realized by a simple deposition of an In drop on each quadrant and on the back side. In subsequent fabrication runs, in order to reduce the electronic noise, the fabrication procedure was improved (in particular in terms of uniformity of the metallic layers of the electrodes).

On the other side of the device, a single metallic layer is deposited as the bias electrode. In order to select the metal for the bias electrode, the photon absorption of the metal layer has to minimized when the beam is hitting from the bias side. To estimate this effect, we calculated the photon absorption spectras of three different metals or metal combinations, that we used for our contacts, namely Al (50nm and 100nm), Ni (50nm) and Au/Ge/Ni (130nm/60nm/20nm) (Fig. 8.1).

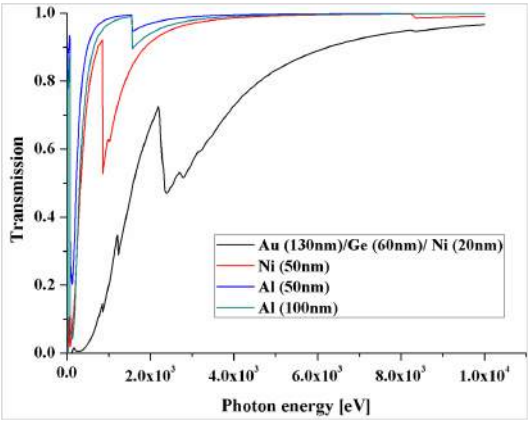

FIGURE 8.1: Transmission spectra of all metal layers was calculated [69]

Due to its low atomic number, Al layer absorbs less the incident photon with respect to the other two metallic layer configurations. Furthermore, it has a less pronounced K_α absorption edge (1.559 keV). Therefore, a metallic layer of Al can be used as bias electrode when the beam is hitting from the bias side since it has minimum absorption of the photons.

To chose the material for the metal pads on the quadrants, the same three kinds configurations of metallic layers were tested for the readout electrodes. Since different pixelation strategies were developed in our devices (5.2.1, 5.2.2 and 5.2.3), we have to choose a metal layer creating good ohmic contact, which can also be useful as a mask for the wet chemical etching for the readout electrode. We developed a test structure to compare the properties of the three metal layers, as is shown in Figure 8.2. Such structure, repeated for all the three metals, consisted of three pads on the surface of the QW side.

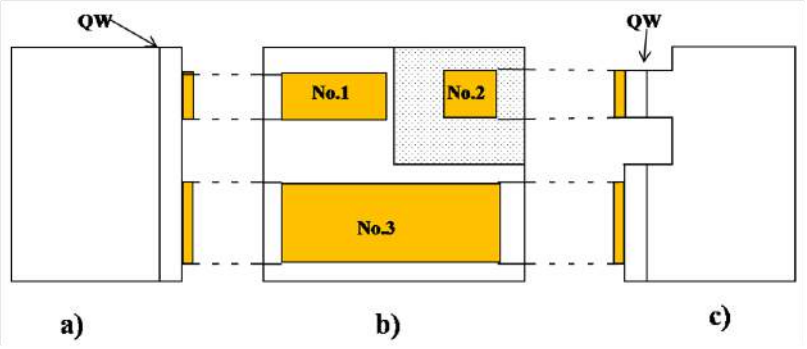

FIGURE 8.2: Developed structure to check ohmic contacts. a) cross section of Pad No.1 and Pad No.3; b) cross section of Pad No.2 and Pad No.3

Pads No.1 and 3 were deposited on the grown surface and electrically connected through the QW. Pad No.2 was still deposited on the grown surface, but the QW around the pad was etched away (1.5 μ deep etch), in order to check electrical conduction through the GaAs substrate. Therefore, the resistance R12 measured between Pad No.1 and 2 is of the order of MΩ (Fig. 8.3a) while the resistance R13 between Pad No.1 and 3 of the order of a few kΩ (Fig. 8.3b).

The Au/Ge/Ni metal combination is proven to provide perfectly ohmic contacts by annealing at 364^{o}C even at cryogenic temperature in InGaAs QW devices [32]. Therefore, Au/Ge/Ni contacts annealed in such a way on our test structure can be considered as the reference of a perfect ohmic contact. Table 8.1 is summarizing R12 and R13 for all the cases with three tested metals. As it is shown in the Figure 8.1, metallic depositions of Al and Ni create contacts right after deposition since their contact resistance is comparable to that of Au/Ge/Ni,

TABLE 8.1: Comparison of metal contacts.

	Au/Ge/Ni		Ni		Al	
Procedure	R12	R13	R12	R13	R12	R13
After deposition	93 MΩ	2.2 kΩ	87 MΩ	1.6 kΩ	113 MΩ	6.9 kΩ
After annealing	89 MΩ	1.3 kΩ	81 MΩ	35 kΩ	80 MΩ	4.0 kΩ
After etching	153 MΩ	142 MΩ	84 MΩ	88 MΩ	327 MΩ	277 MΩ
After annealing then etching	253 MΩ	364 MΩ	303 MΩ	239 MΩ	380 MΩ	201 MΩ

both by contacting the QW (R13) and the underlying substrate (R12), even resistance though Al is a little higher. To better assess the Ohmic behaviour of the various contacts after deposition and after annealing, we have performed I-V scans for R12 in a $\pm$ 0.05V range (Fig. 8.3a) and for R13 in a $\pm$ 1.0V range (Fig. 8.3b). The curves are all linear, showing a perfect ohmic character for all the tested contacts, except for Al. Ohmic behaviour is shown for all metals after annealing all the metal layers. R13 resulted of order of kΩ for all the metals and becoming a bit lower after the annealing, expect for Ni, which increased by an order of magnitude and lost its ohmic behaviour.

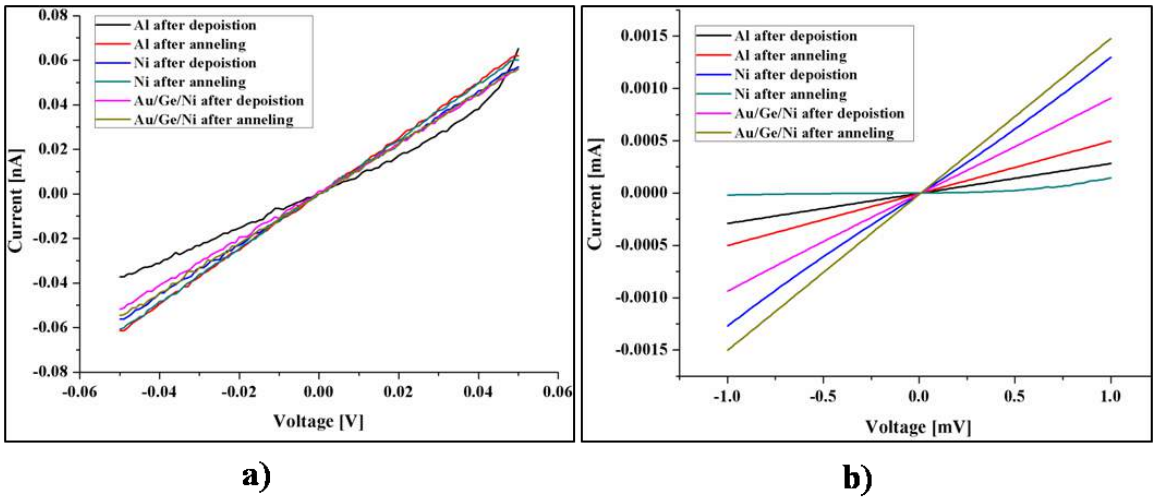

FIGURE 8.3: I-V curve for for the metals after deposition and after annealing; a) R12 b)R13

To realize structures such as the one shown in Figure 5.10, the metal pads have to be exactly aligned to the pixels, avoiding any deposition in the clearances. To avoid a double lithographic exposure and the related aligning difficulties, we have used the metal layers themselves as masks to etch the semiconductor. To test the behaviour of the different metals to etching, we

have used the same structure of Figure 8.2. We performed a blanket etching both through as deposited metal pads and after annealing to 364^0C.

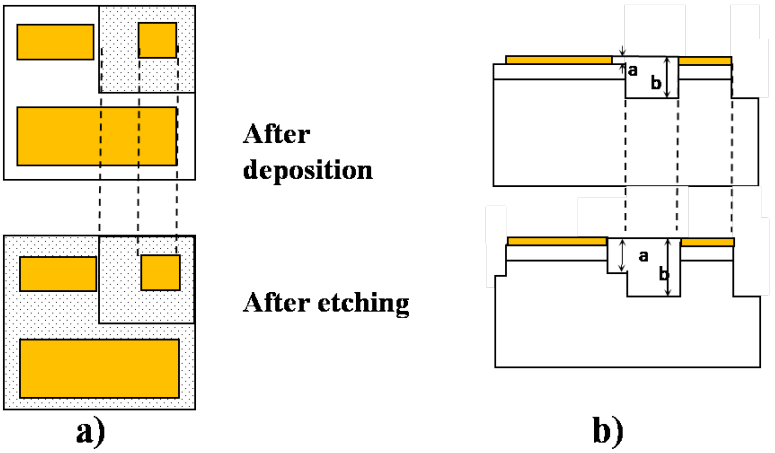

FIGURE 8.4: Schematic view of the surface a) top view b) cross section; dotted area shows the etched surface.

The sample were etched in the phosphoric etching solution for 15 min with ∼100 nm/min etching rate (see table 5.1) after deposition of the metal pads. We then measured the height differences between the metal pads and the region that was etched down from the original surface (marked as a in Fig. 8.4b), and between the metal pads and the region etched down from the previously etched recessed (1.5μm lower, marked as b). If the metal layer is capable to withstand the etching solution and protect the underlying semiconductor, the value of a should be ∼1.5μm, while b should be ∼3.0μm (Table 8.2)

TABLE 8.2: Surface topography of the surface with metal pads before and after etching

	Au/Ge/Ni	Al	Ni
Etching after deposition	a = 2.1μm b = 3.6μm	a = 0.4μm b = 2.0μm	a = 1.9μm b = 3.3μm
Etching after annealing	a = 1.6μm b = 3.3μm	a = 2.0μm b = 3.3μm	a = 0.6μm b = 1.2μm

As shown in Table 8.2, the Au/Ge/Ni triple layer was not attached by the solution even after annealing and etching. However, Ni could resist the chemical etching only when it is not annealed, and Al only after annealing. Annealed Ni and just deposited Al layers were etched and the QW surface as well. The ability of the different metals to sustain etching must be however confirmed by measuring the resistances between the pads (see Figure 8.5). The

resistance R12 between Pad No.1 and 2 of Au/Ge/Ni and Ni before and after etching the as-deposited metals was similar, while it increased considerably for Al, implying that Al was etched away by the solution. The resistances R13 between Pad No.1 and 3 after etching in the phosphoric solution increased to the order of the substrate resistance. However, Au/Ge/Ni and Ni metal layers are still resulting same order of R12 even after annealing and etching.

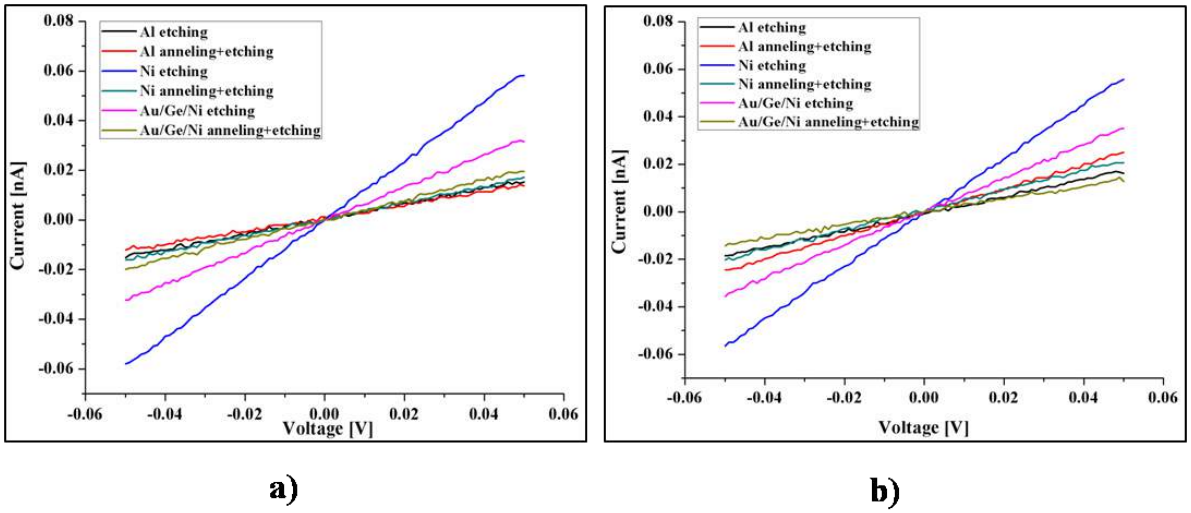

FIGURE 8.5: IV curve of the all metallic layer contact; a)R12 b) R13

As a conclusion, triple layers of Au/Ge/Ni is a suitable metal to create good ohmic contacts for the readout electrode. Moreover, Au/Ge/Ni and Ni metal layers could be used as a protecting mask due to the capability to resist the etching solution. However, the metallic layer should not be annealed before the etching and it can be annealed later. When the beam is hitting from the readout side, Al could be involved as contacting metal with annealing without requiring the etching.

Bibliography

[1] A Galimberti, C.J Bocchetta, C Fava, A Gambitta, G Paolucci, R Presacco, G Paolicelli, and G Stefani. A new detector for photon beam position monitoring designed for synchrotron radiation beamlines. *Nucl. Instrum. Meth A*, 477(1–3):317 – 322, 2002. ISSN 0168-9002. 5th Int. Conf. on Position-Sensitive Detectors.

[2] R. Treusch, T. Lokajczyk, W. Xu, U. Jastrow, U. Hahn, L. Bittner, and J. Feldhaus. Development of photon beam diagnostics for {VUV} radiation from a {SASE} {FEL}. *Nucl. Instrum. Meth:A*, 445(1–3):456 – 462, 2000. ISSN 0168-9002.

[3] TASC-IOM-CNR Laboratory. URL `http://tasc.iom.cnr.it/`.

[4] Elettra-Sincrotrone Trieste. URL `http://www.elettra.trieste.it/`.

[5] University of Trieste. Department of physics. URL `http://www.units.it/`.

[6] W. Schildkamp and C. Pradervand. Position monitor and readout electronics for undulator and focused bending magnet beamlines. *Rev. Sci. Instrum*, 66:1956–1959, 1995.

[7] K. Sato. The position-sensitive ionization chamber for synchrotron radiation experiments. *J. Synchrotron Rad*, 8:378, 2001.

[8] R. H. Menk, D. Giuressi, F. Arfelli, and L. Rigon. A fast high resolution beam position monitor for medium and hard x-rays. *AIP Conf. Proc.*, 879:1109, 2007.

[9] P. Mortazavi, M. Woodle, H. Rarback, and D. Shu. High flux photon beam monitor. *Nucl. Instrum. Meth*, A 246:389, 1986.

[10] T. Warwick, N. Andresen, G. Portmann, and A. Jackson. Performance of photon position monitors and stability of unduiator beams at the advanced light source. *Rev. Scie. Instrum*, 66:1984, 1995.

[11] D. Shu, B. Rodricks, J.Barraza, and T. Sanchez T.M. Kuzay. The aps x-ray undulator photon beam position monitor and tests at chess and nsls. *Nucl. Instrum. Meth*, A 319:56, 1992.

[12] P. Fajardo and S. Ferrer. Ultrahigh-vacuum-csmpatible position and shape monitor for high brilliance synchrotron radiation beams. *Rev. Scie. Instrum*, 66:1882, 1995.

[13] R. W. Alkire, G. Rosenbaum, and G. Evans. Design of a vacuum-compatible high-precision monochromatic beam-position monitor for use with synchrotron radiation from 5 to 25 kev. *J. Synchrotron Rad.*, 7:61, 2000.

[14] N. R. Kyele, K. Decanniereb, and R. G. van Silfhouta. A transparent two-dimensional in situ beamposition and profile monitor for synchrotron x-ray beamlines. *J. Synchrotron Rad.*, 12:800, 2005.

[15] P. Bergonzo, D. Tromson, and C. Mer. Cvd diamond-based semi-transparent beam-position monitors for synchrotron beamlines: preliminary studies and device developments at cea/saclay. *J. Synchrotron Rad.*, 13:151, 2006.

[16] M.R. Fuchs, K. Holldack, M. Bullough, S. Walsh, C. Wilburn, A. Erko, F. Schäfers, and U. Mueller. Transmissive x-ray beam position monitors with submicron position- and submillisecond time resolution. *Rev. Scie. Instrum*, 79(6):063103, 2008.

[17] R.G. van Silfhout. A beam tracking optical table for synchrotron x-ray beamlines. *Nucl. Instrum. Meth:A*, 403(1):153 – 160, 1998. ISSN 0168-9002.

[18] T. R. Oldham. Ionizing radiation effects in mos oxides. *World Scientific*, 1999.

[19] M. Antonelli. *Photon beam-position monitor basati su diamante e quantum well per sorgenti di luce di terza e quarta generazione*. PhD thesis, University of Trieste, 2013.

[20] J. Morse, B. Solar, and H. Graafsma. Diamond x-ray beam-position monitoring using signal readout at the synchrotron radiofrequency. *J. Synchrotron Rad.*, 17:456, 2010.

[21] M. Antonelli, M. Di Fraia, S. Carrato, G. Cautero, R.H. Menk, W.H. Jark, T. Ganbold, G. Biasiol, C. Callegari, M. Coreno, A. De Sio, and E. Pace. Fast synchrotron and fel beam monitors based on single-crystal diamond detectors and ingaas/inalas quantum well devices. *Nucl. Instrum. Meth:A*, 730(0):164 – 167, 2013. ISSN 0168-9002.

[22] F. Capotondi, G. Biasiol, I. Vobornik, L. Sorba, F. Giazotto, A. Cavallini, and B. Fraboni. Two-dimensional electron gas formation in undoped in0.75ga0.25as/in0.75al0.25as quantum wells. *J. Vac. Scie. Tech B", year = 2004, volume = 22, number = 2, pages = 702-706*.

[23] F. Giuliani Gabriele and J.J. Quinn. Spin-polarization instability in a tilted magnetic field of a two-dimensional electron gas with filled landau levels. *Phys. Rev. B*, 31:6228–6232, 1985.

[24] G.E. Stillman, C.M. Wolfe, and J.O. Dimmock. Hall coefficient factor for polar mode scattering in n-type gaas. *J. Phys. Chem. Solids*, 31(6):1199 – 1204, 1970. ISSN 0022-3697.

[25] K. Fletcher and P. N. Butcher. An exact solution of the linearized boltzmann equation with applications to the hall mobility and hall factor of n-gaas. *J.Phys. C:*, 5(2):212, 1972.

[26] H. L. Störmer, R. Dingle, A. C. Gossard, W. Wiegmann, and R. A. Logan. *Physics of Semiconductors*, volume 43. Inst. Phys., Bristol, 1979, 1978.

[27] D. McMorrow, A.R.Knudson, J.B. Boos, Doe Park, and J.S. Melinger. Ionization-induced carrier transport in inalas/ingaas high electron mobility transistors. *Nucl. Scie*, 51(5): 2857–2864, Oct 2004.

[28] V. Palankovski. *PSimulation of Heterojunction Bipolar Transistors*. PhD thesis, Technical University of Vienna, 2000. URL `http://www.iue.tuwien.ac.at/phd/palankovski/`.

[29] URL `http://www.ioffe.rssi.ru/SVA/NSM/Semicond/`.

[30] I. Vurgaftman, J.R. Meyer, and L.R. Ram-Mohan. Band parameters for iii–v compound semiconductors and their alloys. *J. Appl. Phys*, 89(11):5815–5875, 2001.

[31] G. Snider. 1d poisson. URL `http://www3.nd.edu/~gsnider/`.

[32] F. Capotondi, G. Biasiol, D. Ercolani, V. Grillo, E. Carlino, F. Romanato, and L. Sorba. Strain induced effects on the transport properties of metamorphic inalas/ingaas quantum wells. *Thin Solid Films*, 484(1–2):400 – 407, 2005. ISSN 0040-6090.

[33] F. Capotondi, G. Biasiol, I. Vobornik, L. Sorba, F. Giazotto, A. Cavallini, and B. Fraboni. Two-dimensional electron gas formation in undoped $in_{0.75}ga_{0.25}as$/ $in_{0.75}al_{0.25}as$ quantum wells. *J. Vac. Scie.Tech B*, 22(2):702–706, 2004.

[34] E.N. Savitskaya, Yu.V. Beletskaya, G.I. Krupnyi, Ya.N. Rastsvetalov, and A.V. Sannikov. Photon detection efficiency of a germanium semiconductor spectrometer. *Instrum. Exp. Tech*, 55(3):407–414, 2012.

[35] Cheng Xu, Han Chen, Mats Persson, Staffan Karlsson, Mats Danielsson, Christer Svensson, and Hans Bornefalk. Energy resolution of a segmented silicon strip detector for photon-counting spectral {CT}. *Nucl. Instrum. Meth:A*, 715(0):11 – 17, 2013. ISSN 0168-9002.

[36] B.E.A. Saleh and M.C. Teich. *Fundamentals of Photonics*, volume 15. John Wiley and Sons, Inc, 1991.

[37] G. Bertuccio and D. Maiocchi. Electron-hole pair generation energy in gallium arsenide by x and γ photons. *J. Appl. Phys*, 92(3):1248–1255, 2002.

[38] B. F. Levine. Quantum-well infrared photodetectors. *J. Appl. Phys.*, 74(8):R1–R81, 1993.

[39] D. Chattopadhyay, S.K. Sutradhar, and B.R. Nag. Electron transport in direct-gap iii-v ternary alloys. *J. Phys. C*, 14(6):891, 1981.

[40] D. Ercolani. *Transport properties of InGaAs based devices*. PhD thesis, Universit'a di Modena e Reggio Emilia, 2007.

[41] M. Di. Fraia, M. Antonelli, A. Tallaire, J. Achard, S. Carrato, R. H. Menk, G. Cautero, D. Giuressi, W. H. Jark, F. D'Acapito, A. De Sio, and E. Pace. X-ray beam position monitor based on a single crystal diamond performing bunch by bunch detection. *Joyrnal of Physics*, 425(212001), 2013.

[42] M. A. Herman and H. Sitter. Molecular beam epitaxy. *Springer-Verlag*, 1996.

[43] C.T. Foxon and B.A. Joyce. Interaction kinetics of as_4 and ga on $\{100\}$ gaas surfaces using a modulated molecular beam technique. *Surf. Scie*, 50(2):434 – 450, 1975. ISSN 0039-6028.

[44] C.T Foxon and B.A Joyce. Interaction kinetics of as_2 and ga on $\{100\}$ gaas surfaces. *Surface Science*, 64(1):293 – 304, 1977. ISSN 0039-6028.

[45] F. Turco, J.C. Guillaume, and J. Massies. Thermodynamic analysis of the molecular beam epitaxy of alinas alloys. *J. Crys. Growth*, 88(2):282 – 290, 1988. ISSN 0022-0248.

[46] U. Kreibig and M. Vollmer. Optical properties of metal clusters. *Springer*, 1995.

[47] R. C. Jaeger. *Introduction To Microelectronic Fabrication*. Auburn, Upper Saddle River - Prentice Hall, 2002.

[48] L. J. van der Pauw. A method of measuring specific resistivity and hall effect of discs of arbitrary shape. *Philips Research Reports*, 1958.

[49] D. Daghero. *Experimental study of non-conventional gap features in novel superconductors*. PhD thesis, University of Torino, 2001.

[50] K.F. Wall and A. Sanchez. Titanium sapphire lasers. *The Lincoln Laboraotory Journal*, 33(3):447–462, 1993.

[51] B. Fultz and J.M. Howe. *Transmission Electron Microscopy and Diffractometry of Materials*. Springer, 2013.

[52] P. Dhez, H. Duval, and J.C. Malaurent. Multilayer x-ray mirror calibration by an energy dispersive method using an x-ray tube and a si(li) detector: Absolute reflectivity, energy band pass, and overlapping order determination. *J. X-ray. Sc. Techn*, 3(3):176–193, 1992.

[53] XRF beamline. . URL `http://www.elettra.trieste.it/lightsources/elettra/elettra-beamlines/microfluorescence/x-ray-fluorescence.html`.

[54] SYRMEP beamline. . URL `http://www.elettra.trieste.it/elettra-beamlines/syrmep.html`.

[55] L. Rebuffi, J.R. Plaisier, M. Abdellatief, A. Lausi, and P. Scardi. Mcx: a synchrotron radiation beamline for x-ray diffraction line profile analysis. *Z. anorg. allg. Chem.*, 640: 3100–3106, 2014.

[56] Elettra Sincrotrone Trieste S.C.p.A. Ah501b picoammeter. URL `http://ilo.elettra.trieste.it/index.php?page=_layout_prodotto&id=141&lang=en`.

[57] S. Sze. Physics of semiconductor devices. *Wiley Interscience Publication*, 1981.

[58] S Mendach, C.M Hu, Ch Heyn, S Schnüll, H.P Oepen, R Anton, and W Hansen. Strain relaxation in high-mobility inas inserted-channel heterostructures with metamorphic buffer.

Physica E: Low-dimensional Systems and Nanostructures, 13(2–4):1204 – 1207, 2002. ISSN 1386-9477.

[59] F. Capotondi, G. Biasiol, D. Ercolani, and L. Sorba. Scattering mechanisms in undoped in0.75ga0.25as/in0.75al0.25as two-dimensional electron gases. *J.Crys. Growth*, 278(1–4):538 – 543, 2005. ISSN 0022-0248. 13th International Conference on Molecular Beam Epitaxy.

[60] J. Piotrowski and A. Rogalski. Uncooled long wavelength infrared photon detectors. *Infra. Phys. Tech*, 46(1–2):115 – 131, 2004. ISSN 1350-4495. Workshop on Advanced Infrared Technology and Application.

[61] T. Ganbold, M. Antonelli, G. Biasiol, R. Cucini, G. Cautero, and R.H. Menk. Fast, multi-wavelength, efficiency-enhanced pixelated devices based on ingaas/inalas quantum- well. *J. Inst*, accepted, 2014.

[62] K. Tono, T. Togashi, Y. Inubushi, T. Sato, T. Katayama, K. Ogawa, H. Ohashi, H. Kimura, S. Takahashi, K. Takeshita, H. Tomizawa, S. Goto, T. Ishikawa, and M. Yabashi. Beamline, experimental stations and photon beam diagnostics for the hard x-ray free electron laser of sacla. *N. J. Phys*, 15(8):083035, 2013.

[63] g. Liu Chun-Hung, C.W. Philip, Yu-Tian Shen, Sheng-Wei Chien, and Kuen-Yu Tsai. Impacts of point spread function accuracy on patterning prediction and proximity effect correction in low-voltage electron-beam. *J. Vac. Scie. Tech. B*, 31(2):021605–021605–18, Mar 2013. ISSN 1071-1023.

[64] J. A. Bearden and A.F.Burr. Reevaluation of x-ray atomic energy levels. *Rev. Mod. Phys*, 39(1):125–142, 1967.

[65] R.L Bates, M Campbell, S D'Auria, C Da Vià, V O'Shea, C Raine, and K.M Smith. Recent results on gaas detectors. *Nucl. Instrum. Meth:A*, 392(1–3):269 – 273, 1997. ISSN 0168-9002. Position-Sensitive Detectors Conference 1996.

[66] R.L. Bates, M. Campbell, C. Da Via, E. Heijne, M. Heuken, H. Jurgensen, J. Ludwig, S. Manolopoulos, D. Marder, K. Mathieson, V. O'Shea, C. Raine, M. Rogalla, and K.M. Smith. Developments in gaas pixel detectors for x-ray imaging. pages 534–540, Nov 1997.

[67] A.D. Dimitrov, B. Richard, J.R. Cary, I. Ben-Zvi, S. John, C. Xiangyun, R. Triveni, K/ Jeffrey, M. Erik, and B. Andrew. Simulations of charge gain and collection efficiency from diamond amplifiers. *Mater. Res. Soc. Symp. Proc.*, (1203), 2010.

[68] T. Ganbold, M. Antonelli, G. Biasiol, G. Cautero, H. Jark, D.M. Eichert, R. Cucini, and R.H. Menk. Position sensitive photon detectors using epitaxial ingaas/inalas quantum wells. *J. Inst*, 9(12):C12043, 2014.

[69] B.L. Henke, E.M. Gullikson, and J.C. Davis. X-ray interactions: photoabsorption, scattering, transmission, and reflection at e=50-30000 ev, z=1-92. *Atomic Data and Nuclear Data Tables*, 54(2):181–342, 1993. URL `http://henke.lbl.gov/optical_constants/filter2.html`.